To the Graduate Council:

I am submitting herewith a dissertation written by Gary Alan Glass entitled "Electron Capture to the Continuum from Atomic Hydrogen." I have examined the final copy of this dissertation for form and content and recommend that it be accepted in partial fulfillment of the requirements for the degree of Doctor of Philosophy, with a major in Physics.

Ivan A. Sellin, Major Professor

We have read this dissertation and recommend its acceptance:

Accepted for the Council:

The Graduate School

4

ELECTRON CAPTURE TO THE CONTINUUM FROM ATOMIC HYDROGEN

A Dissertation

Presented for the

Doctor of Philosophy

Degree

The University of Tennessee, Knoxville

Gary Alan Glass

March 1984

ACKNOWLEDGEMENTS

I would like to express my gratitude to the entire Atomic Physics Group at The University of Tennessee for the many hours contributed to the success of this project and especially to Peter Engar, who spent many long hours providing necessary assistance. The assistance of the staff and the use of the ORNL EN Tandem Van de Graaff facility is also greatly appreciated.

I would like to thank my wife, Judy, for typing the manuscript and my wife and children, Jimmy and Rebecca, for understanding my many absences during the past few years. I would also like to thank Dr. Stuart B. Elston for his advice and helpful suggestions in preparing this dissertation. Finally, I would like to thank my mother, who offered encouragement in many ways.

ABSTRACT

The differential cross section measurement for electron capture to the continuum (ECC) by 12 MeV C^{6+} ion incident on atomic hydrogen has been obtained. A value of $(4.48\pm3.2)\times10^{-19}\ \frac{cm^2}{sr\text{-}atom}$ was found for the differential cross section for an experimental acceptance angle of 2^{o}. The ratio of the ECC differential cross sections for molecular and atomic hydrogen was found to be $\sim$1.25.

The atomic hydrogen target was produced by a high temperature oven which dissociates H_2 molecules into H atoms. At a temperature of 2350K, dissociation fractions of >90% were obtained for pressures >3 mTorr in the oven. The oven is electron impact heated by a beam of electrons produced by an electron gun with a Pierce lens system. Design, construction, and operating characteristics of the oven are presented.

TABLE OF CONTENTS

CHAPTER		PAGE
I.	INTRODUCTION	1
	Historical Remarks	3
	Experimental Considerations	9
II.	THEORY	12
	Formal Theory of Scattering	12
	Coulomb Scattering	18
	First Born Approximation	20
	Macek's Theory	21
	Salin's Theory	23
	Dettmann's Theory	26
	Chan and Eichler Theory	29
	Shakeshaft and Spruch Theory	30
	Jakubassa-Amundsen Theory	31
III.	EXPERIMENTAL METHODS AND APPARATUS FOR ECC MEASUREMENTS	38
	Description of Experiment	38
	Projectile Ion	40
	Experimental Configuration and Vacuum Systems	41
	Oven Vacuum Chamber	45
	ECC Data Acquisition	46
	ECC Background Noise	50
	Gas Handling System	53
	Determining Oven Pressure for Non-Dissociating Gas	57
	Impurities in Gas Cell	60
	Magnetic Field Nulling	62
	Electron Spectrometer	68
IV.	THE ATOMIC HYDROGEN OVEN	78
	Introduction	78
	Construction and Design of the Oven	81
	Electron Gun	93
	Temperature	98
	Background Rates	101
	Determining Oven Pressure for a Dissociating Gas	106
	Temperature Correction for Mirror-Window-Transmission	111
	Experimental Determination of the Dissociation Fraction	111
	Dissociation Fraction Results	121

CHAPTER PAGE

V. DATA ANALYSIS 126

Subtracting Background From ECC Spectrum 131
Calibrating Gas Flow 136
Estimates of Errors Associated With the ECC Cross Section 141
Spectral Shape Analysis 143

VI. RESULTS AND CONCLUSION 146

Calibration of System for Absolute Cross Sections 146
Calculation of Cross Sections 154
Results of ECC Measurements 155
Conclusions 157

LIST OF REFERENCES 159

APPENDICES 164

APPENDIX A. EQUILIBRIUM DISSOCIATION FRACTION 165

APPENDIX B. DOUBLE CAPTURE METHOD FOR MEASURING DISSOCIATION FRACTIONS 173

APPENDIX C. SINGLE LOSS-SINGLE CAPTURE METHOD FOR DETERMINING DISSOCIATION FRACTIONS 177

APPENDIX D. THE ELECTRON GUN 181

APPENDIX E. STATISTICAL ERRORS ASSOCIATED WITH DISSOCIATION FRACTION MEASUREMENTS 192

VITA 194

LIST OF TABLES

TABLE		PAGE
I.	IMPURITIES IN OVEN VACUUM CHAMBER	63
II.	ELECTRON SPECTROMETER CALIBRATION PARAMETERS	77
III.	OVEN CHARACTERISTICS	79
IV.	ELECTRON GUN CHARACTERISTICS	96
V.	CALIBRATION OF PRESSURE IN THE OVEN	138
VI.	ERRORS ASSOCIATED WITH CROSS SECTION	144
VII.	EXPERIMENTAL ECC CROSS SECTIONS FOR 12 MeV C^{6+} INCIDENT ON ATOMIC AND MOLECULAR HYDROGEN	156
VIII.	FULL-WIDTH-AT-HALF-MAXIMA MEASURED FOR ECC CUSPS	157

LIST OF FIGURES

FIGURE		PAGE
1.	Angular Distribution of Electrons Ejected From 300 keV Protons Incident on He	5
2.	Experimental ECC Spectrum of Crooks and Rudd[11] Compared to the Theory of Macek[12]	7
3.	Differential Cross Section at Forward Angles for 300 keV Protons Incident on Atomic Hydrogen	25
4.	Comparison of Three ECC Theories	32
5.	Semi-Classical Impulse Approximation ECC Spectrum	37
6.	Hydrogen Oven Beam Line	42
7.	Block Diagram of Electronics	47
8.	Schematic Diagram of Gas Handling System	55
9.	Impurities Flowing Into Oven From Gas Handling System	62
10.	Electron Analyzing Apparatus	70
11.	Spectrometer Calibration Electron Gun Electrical Schematic	71
12.	Analyzer Transmission of 1000 eV Electrons Produced By Electron Gun	72
13.	Analyzer Energy Resolution Calibration	73
14.	Analyzer Transmission Function Compared to Typical ECC Cusp	74
15.	Analyzer Constant Calibration	75
16.	Close-up View of Atomic Hydrogen Oven	82
17.	Atomic Hydrogen Oven Assembly	85
18.	Placement of Electron Spectrometer	94
19.	Electrical Schematic for Oven Heating Electron Gun	95
20.	Temperature of Oven Versus Electron Gun Power	99

FIGURE PAGE

21. Background Count Rate Versus Electron CEM Box Bias 104

22. Atomic and Molecular Hydrogen Pressures Inside Hot Oven 109

23. Atomic and Molecular Hydrogen Densities Inside Hot Oven 110

24. Correction of Oven Temperature Reading for Transmission Through Mirror-Window System 112

25. Dissociation Fraction Versus Pressure 116

26. Pressure Difference Across Flow Aperture Versus Dissociation Fraction f 118

27. Experimental Dissociation Fraction at 2350K 122

28. ECC Cusp and Background From Mixture of H and H_2 in Hot Oven 133

29. Background Subtracted ECC Cusp From Mixture of H and H_2 134

30. ECC Electrons Versus Gas Flow Into Oven 139

31. Thermal Transpiration Curve for Argon 141

32. ECC Spectrum for 12 MeV C^{6+} Incident on H_2 147

33. ECC Spectrum for 12 MeV C^{6+} Incident on the Hot H, H_2 Mixture 148

34. ECC Spectrum on Atomic Hydrogen 149

35. ECC Singly Differential Cross Section for H^+, C^{6+}, O^{8+}, and Si^{14+} on Argon 153

C.1. Ratio of Single-Loss to Single-Capture Yields Versus Dissociation Fraction 180

D.1. Effect of Anode Aperture on Electron Beam Focal Point . . . 184

D.2. Minimum Electron Beam Radius Compared to Radius at Cathode 188

D.3. Position of Minimum Beam Radius Relative to Anode 190

D.4. Electron Path Through Cathode-Anode Lens System 191

CHAPTER I

INTRODUCTION

When a fast ion beam is incident on gaseous target atoms, a variety of resultant physical phenomena are observed which can be either elastic or inelastic in nature. Elastic collisions can result in changes in the direction of motions of the colliding incident ion and target atom, but the internal structure of each collision participant will remain the same before and after the collision. Most of the collisions between fast ions and stationary target atoms will be elastic collisions. The small fraction of collisions which are inelastic can produce internal structure changes to either the projectile or target, or both. These internal changes can include direct ionization, charge exchange between the projectile ion and the target atom, and excitation of one or more electrons in either the projectile ion or target atom. These processes will, of course, occur in some combination depending on the velocity of the incident ion.

The electron energy spectra resulting from electrons ejected during a high energy ion-atom collision for high energies ($\lesssim$15 MeV/u) have several distinguishing features.[1,2,3] 1) Discrete lines are observed due to autoionization or electrons emitted from excited states of the target atom. Projectile ions can also emit secondary electrons in this manner, but the positions of the lines are Doppler shifted due to the motion of the projectile. 2) There is an underlying distribution of electrons originating from direct ionization of the target atom. This distribution decreases monotonically with increasing electron energy. 3) For the

electrons emitted in the forward direction (0^{o} is defined to be in the direction of motion of the projectile), the distribution has two additional distinctive features: a) For forward angles $\lesssim 20^{o}$ a broad peak appears at the electron energy corresponding to an electron velocity approximately twice that of the incident projectile. This is the energy-momentum-conservation peak arising from the binary encounter between the projectile and the target electron. b) For forward angles $\lesssim 10^{o}$ another peak appears in the spectrum for the electron energies corresponding to velocities approximately equal to the projectile velocity. This peak becomes very prominent for electron ejection angles very near 0^{o} and results from electrons captured to continuum states of the target atom. Electron loss from the projectile to continuum states of the target atom (ELC)[14] can occur only for incompletely ionized projectile ions. Since the projectile used in this study was a bare ion this process will not be considered.

The subject of this study will be one of the inelastic processes, electron capture to projectile-centered continuum states (ECC) using atomic hydrogen as a target. If a bare ion is incident on a target atom and an electron is emitted in the forward direction with a velocity equal to that of the incident ion, that electron is considered to be an ECC electron, provided the electron is not captured into a bound state of the ion. The binary encounter peak, ECC peak, and the underlying direction ionization distribution can be seen in Figure 5 on page 37. Details of these distributions will be given in Chapter II.

Historical Remarks

In 1927, Thomas[4] suggested that a possible mechanism for electron capture by a projectile ion from a target atom, for high projectile velocities, was a double scattering process. A calculation performed by Thomas used a classical treatment describing a bare ion traveling at high velocity incident on a hydrogen atom. As shown in the following diagram, the incident ion of mass M_B, strikes the electron of mass m,

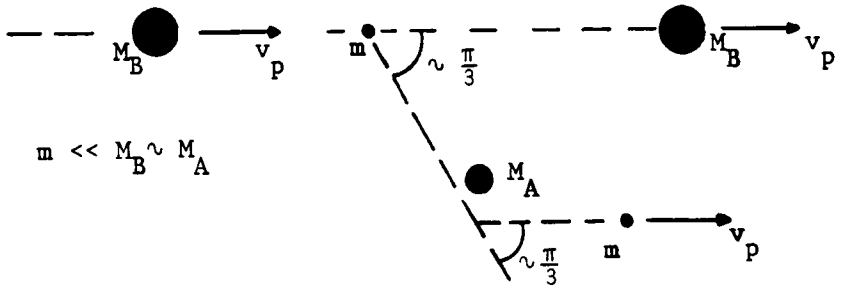

which is bound to a target nucleus of mass M_A. The electron is elastically scattered toward the target nucleus, while the ion continues on with negligible deflection. In order that M_B can capture m, Thomas supposed that m must have a final velocity close to the velocity of M_B. This condition required a second elastic scattering event in which m is scattered by M_A such that the final velocity of m is equal in magnitude and direction to the velocity of M_B. Neglecting terms of order m/M_B, m must scatter twice through two angles of $\sim 60^\circ$. Thomas' results for protons scattered by atomic hydrogen predicted a cross section with a v_p^{-11} dependence on the proton velocity.

Brinkman and Kramers[5] performed the first quantum mechanical calculation of forward capture and predicted a v_p^{-12} dependence of the cross section for high velocity. This calculation was essentially a first Born calculation (see Chapter II) except that the internuclear potential was omitted. This approximation is generally called the

Oppenheimer-Brinkman-Kramers (OBK) approximation since it was also introduced by Oppenheimer at nearly the same time.[6] Neglecting this nuclear potential term is justified since the potential depends on the nuclear separation, which is essentially the same as the separation of the center of masses of the two systems, at least to order m/M_A. The internuclear potential can not, therefore, significantly affect the internal state of either system.

For many years the discrepancy between the classical calculation of Thomas and the quantum calculation of Brinkman and Kramers remained unexplained.[7] This discrepancy was disturbing since the correspondence principle should be applicable for the process being described, i.e., the electron is scattered at large angles with high speed. It was believed that the classical calculation neglected subtle interference effects. However, in 1955, Drisko[8] realized that the classical formulation of Thomas is a two-step scattering process which should correspond to a second Born term (see Chapter II) in the quantum mechanical treatment of the process. Drisko indeed found that a calculation of the second Born term resulted in a v_p^{-11} dependence of the cross section, a fact which seemed to validate the classical approximations of Thomas.

However, this scattering phenomenon was considered for bound state capture only until 1966, when Rudd, et al.[9] obtained experimental differential cross sections for the ejection of electrons by 300 keV protons incident on He. Figure 1 shows the angular distribution of electrons for several different ejection energies. It is seen that as the emission angle approaches 0^o, there is a definite increase in the cross section for energies less than 200 eV. The

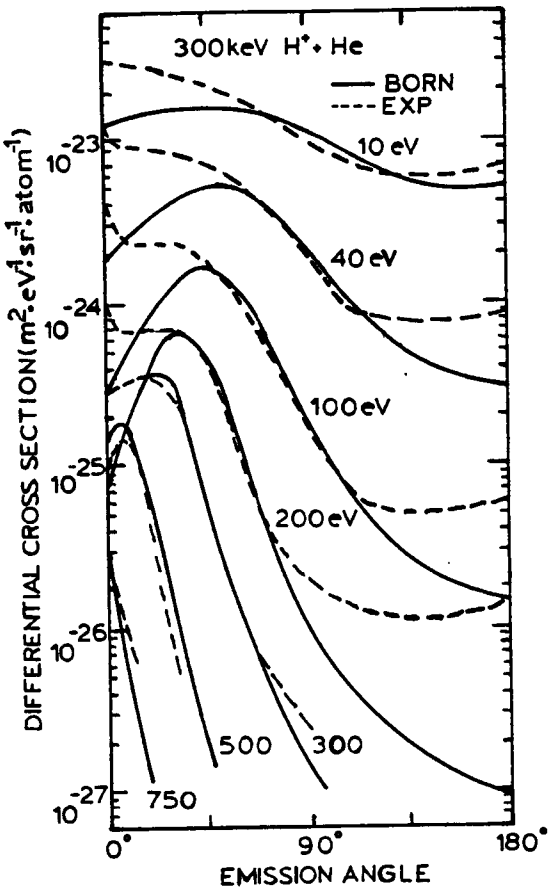

Figure 1. Angular Distribution of Electrons Ejected From 300 keV Protons Incident on He.

Note the increase in experimental cross section (---) for electrons with energy less than 200 eV as the emission angle approaches 0°. The Born theory (——) fails to reproduce this feature. (Reproduced from reference 9.)

electron energy E_e, corresponding to a velocity equal to the incident proton velocity can be easily found by using,

$$E_e = \frac{m_e}{M_p} E_p \qquad (1)$$

where $E_p \equiv$ proton energy, $m_e \equiv$ electron mass, and $M_p \equiv$ proton mass. For a 300 keV proton energy, the electron energy is $\sim$163 eV. It is obvious from Figure 1 that the angular distributions for 100 eV and 200 eV electrons are the most strongly peaked distributions for forward angles of emission, i.e., 0°. Note also the large discrepancies between the experimental data and the theoretical curves obtained from a first Born calculation.

In 1967, Oldham[10] calculated the differential cross section for the ejection of electrons by 200-300 keV protons incident on helium. This first Born calculation was compared with the experimental results of Rudd, et al.[9] Large discrepancies were noted between theory and experiment for forward emission angles when the velocities of the proton and ejected electron were nearly equal. Oldham speculated that this could be due to an interaction between the ejected electron and the scattered proton. The Born approximation for ionization neglected the higher order terms in the interaction between the ejected electron and the scattered proton because the ejected electron was supposed to move in the field of the ionized atom.

In 1969, Crooks and Rudd[11] obtained electron energy distributions for electron ejected at 0° when protons of various energies were incident on a helium gas target. Figure 2 shows a comparison of the experimental electron spectrum with the first Born theory of Macek,[12] which included distortion of the electron final state by the proton. Also shown in the figure is a calculation using the first Born approximation in which the final state of the electron is considered to be a plane-wave, i.e., there is no interaction between the proton and electron. It is obvious that the first Born approximation without inclusion of the electron-proton

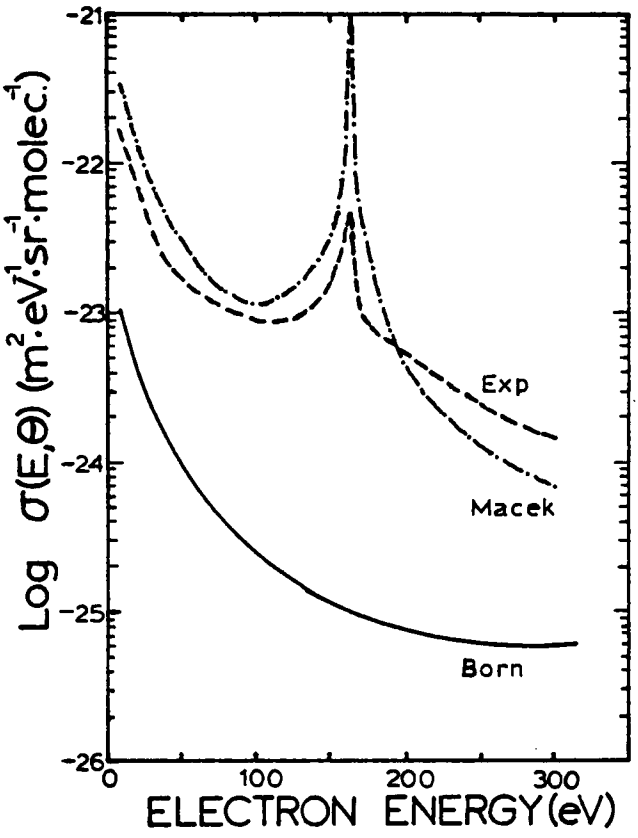

Figure 2. Experimental ECC Spectrum of Crooks and Rudd[11] Compared to the Theory of Macek.[12]

The first Born calculation is shown as the solid line. The Born theory obviously does not indicate the existence of the cusp. (Reproduced from reference 11).

interaction fails entirely to reproduce the experimentally observed peak. A short time later, Salin[13] also performed a first order Born calculation which included distortion of the electron final state by the proton. The theories of Macek[12] and Salin[13] exhibited one major difference in the final result: Macek's theory predicted an essentially symmetric electron velocity distribution centered about the electron velocity equal to the proton velocity while Salin's results give an asymmetric distribution at low proton velocities and tended toward symmetric distributions only at high velocities. The existence of the asymmetry in the electron velocity spectrum has since been supported by experimental data.[14-17]

Dettmann, et al.[18] later obtained an analytical result for the differential cross section for electrons ejected when bare ions are incident on a solid target with a second order Born approximation using a T-matrix formulation. The OBK approximation was also applied. The result produced a symmetric velocity distribution.

From 1974 to the present, a number of theoretical approaches have been introduced which have attempted to resolve the question of the origin and nature of the asymmetry observed in the experimental velocity spectra.[19-25] It had been theoretically established by Drisko[8] that the second Born approximation term will dominate the first Born term for high incident velocity for ground state-to-ground state electron capture in proton-hydrogen collisions. Macek, et al.[26] state that energies of 10 MeV/u were sufficiently high in order that the high velocity condition hold. However, this is in a velocity region where radiative capture dominates over continuum capture and, consequently, experimental data would be difficult to obtain. Chan and Eichler[19] have shown that an asymmetric

velocity distribution can be obtained by retaining certain terms that Dettmann, et al.[18] disregarded in their formulation. Shakeshaft and Spruch used the same approach as Dettmann, et al.,[18] however, the result was an asymmetric velocity distribution. Shakeshaft and Spruch noted that the Dettmann formula was incorrect due to an error in one of the calculations. Theories by Garibotti and Miraglia[23,24] and Jakubassa-Amundsen[21,22] have also established the asymmetry of the ejected electron velocity distribution.

Experimental Considerations

Total cross sections using the Born approximation are still valid since most ejected electrons have small velocities when compared to the incident proton, however, in the velocity region where the ejected electron velocity is close to that incident proton, and for forward emission angles, the differential cross section exhibits a large discrepancy when this electron-projectile interaction is not taken into account. Although all of the theories available to date correctly predict the existence of the cusp shape with a peak in the differential cross section at an electron velocity equal to the incident ion velocity, there is disagreement among the theories concerning salient and interesting features of electron spectra such as the nature of the asymmetry of the cusp, the change in the cusp shape as the incident ion velocity increases and dependence of the differential cross section on such parameters as incident ion energy, target nuclear charge and projectile nuclear charge. All theories, although differing in the quantitative methods used to calculate cross sections, do have one factor in common: The target atom is considered to be hydrogenic, i.e., only one electron is bound to the target. This

is necessitated by the inherent difficulties introduced when multi-electron atoms are considered. Theoretical calculations are also hampered by the non-orthogonality of the initial and final states of the collision system. This makes it difficult to choose accurate wavefunctions. Experimental investigations can therefore be directly compared to theory only if atomic hydrogen is used as a target. Such investigations could be conducted if the technology were available for the production of a satisfactory atomic hydrogen target. However, the high temperature dissociation ovens by which atomic hydrogen targets are presently produced[27-33] are not satisfactory for studying electrons ejected from ion-atomic hydrogen interactions. Heretofore, there have been no attempts to produce a static atomic hydrogen target for use in experiments involving the ECC process. The primary goal of this study was to obtain the first ECC spectrum resulting from the interaction of a bare ion projectile beam with a static atomic hydrogen target. No comprehensive study of the ECC process was undertaken since the objective was to develop the methods and apparatus so that a subsequent, more complete investigation could be accomplished. In order to produce the atomic hydrogen target for this experiment, a new type of atomic hydrogen dissociation oven was required.

The necessity of producing the atomic hydrogen target required that this study consist of two major parts; 1) The design and construction of the atomic hydrogen dissociation oven, and 2) obtaining an ECC spectrum using the atomic hydrogen produced by this dissociation oven. The remaining chapters attempt to separate these two parts as much as possible in order that the physics (ECC experiment) be removed from the engineering (design and use of the dissociation oven). Chapter II gives a description

of the formal theory of scattering, and the applicability of that generalized theory to the ECC process. Several of the more prominent theories mentioned in this chapter are detailed in Chapter II. Chapter III describes the acquisition of the ECC data without a detailed discussion of the dissociation oven. Chapter IV is devoted to detailed discussions of the technical requirements, design, construction, and operational features of the dissociation oven. Chapter V outlines the methods used to analyze the data, while Chapter VI gives the results of the experiment and concluding remarks.

CHAPTER II

THEORY

Formal Theory of Scattering

This section is derived, for the most part, from Reference 34. Let the wavefunction $\Psi(\bar{r})$ satisfy the time independent Schrödinger equation for the motion of a particle of mass M under the influence of a stationary potential $V(\bar{r})$. If the particle has kinetic energy E, at infinity, then the Schrödinger equation is given by

$$(\nabla^2+k^2)\Psi(\bar{r}) = \frac{2M}{\hbar^2}V(\bar{r})\Psi(\bar{r}), \tag{2}$$

where $k^2 = \frac{2ME}{\hbar^2}$. The effect of the potential $V(\bar{r})$ is assumed to be negligible at large distances $|\bar{r}|$, away from the scattering center and to be spherically symmetric. At large distances from the scattering center the wavefunction of the scattered particle $\Psi(\bar{r})$, can be shown to have the asymmptotic form

$$\Psi(\bar{r}) \underset{r \to \infty}{\longrightarrow} e^{j\bar{k}\cdot\bar{r}} + \frac{1}{r}e^{jkr}f(\Theta,\Phi), \tag{3}$$

where $j \equiv \sqrt{-1}$. The first term on the right represents an incoming plane wave while the second term has the form of an outgoing spherical wave $\frac{1}{r}e^{jkr}$ multiplied by an angular factor $f(\Theta,\Phi)$, which is called the scattering amplitude. The form of $\Psi(\bar{r})$ given in (3) will be a solution of (2) for large r only if the potential V(r) satisfies the condition[34]

$$\lim_{r \to \infty} |rV(r)| = 0. \tag{4}$$

Note that this requirement for the asymptotic form of V(r) specifically excludes the Coulomb potential. This will be discussed further in a later section.

The solution to the Schrödinger equation (2) can be written more concisely by using a Green's function formalism. This gives an integral equation called the Lippmann-Schwinger equation[34]

$$|\Psi^+> = |\Psi_o> + G_o^+ V|\Psi^+>, \tag{5}$$

where G_o^+ is the free particle Green's function satisfying

$$(\nabla^2+k^2)\ G_o^+(\bar{r},\bar{r}') = \delta(\bar{r}-\bar{r}'), \tag{6}$$

with solution[34]

$$G_o^+(\bar{r},\bar{r}') = -\frac{1}{4\pi}\frac{e^{jk|\bar{r}-\bar{r}'|}}{|\bar{r}-\bar{r}'|} \xrightarrow[r\to\infty]{} -\frac{1}{4\pi}\frac{e^{jkr}\ e^{-j\bar{k}'\cdot\bar{r}'}}{r}, \tag{7}$$

where $\bar{k}'\equiv k\hat{r}$. The wavefunction $|\Psi_o> = e^{j\bar{k}\cdot\bar{r}}$ satisfies the free particle Schrödinger equation

$$(\bar{\nabla}^2+k^2)\,|\Psi_o> = 0, \tag{8}$$

and the second term on the right of equation (5) represents a shorthand notation for an integral given by

$$G_o^+ V|\Psi^+> \equiv \int G_o^+(\bar{r},\bar{r}')V(\bar{r}')\Psi^+(\bar{r}')\,d\bar{r}'. \tag{9}$$

The superscript +, signifies that functions satisfy the outgoing wave boundary conditions. If the asymptotic form for $G_o^+(\bar{r},\bar{r}')$ in (7) is used along with (9) in (5) the asymptotic form for $\Psi^+(\bar{r})$ becomes

$$\psi^{+}(\bar{r}) \xrightarrow[r \to \infty]{} e^{-j\bar{k}\cdot\bar{r}} - \frac{1}{4\pi}\frac{e^{jkr}}{r}\int e^{-j\bar{k}'\cdot\bar{r}'} V(\bar{r})\psi^{+}(\bar{r}')d\bar{r}'. \tag{10}$$

Comparing (10) with (3) shows that the scattering amplitude is given by

$$f(\theta,\phi) = -\frac{1}{4\pi}\int e^{-j\bar{k}'\cdot\bar{r}'} V(\bar{r}')\psi^{+}(\bar{r}')d\bar{r}'. \tag{11}$$

The Green's function operators are defined as

$$G_o^{+} \equiv \lim_{\varepsilon\to o} \frac{1}{E_o - H_o + j\varepsilon}, \tag{12}$$

and

$$G^{+} \equiv \lim_{\varepsilon\to o} \frac{1}{E - H + j\varepsilon}, \tag{13}$$

where H_o and E_o are the free particle Hamiltonian and energy operators, respectively. The Green's function G^{+}, is defined in terms of the Hamiltonian $H = H_o + V$, where V is a perturbation. The energy E, is then the energy of the particle under the influence of V. The transition operator T, is defined by the equation

$$V|\psi^{+}\rangle = T|\psi_o\rangle, \tag{14}$$

and it can be shown that T satisfies[34]

$$T = V + VG^{+}V. \tag{15}$$

Series expressions for G^{+}, $|\psi^{+}\rangle$, and T can be obtained by using the method of successive approximations.

$$G^{+} = G_o^{+} + G_o^{+}VG_o^{+} + G_o^{+}VG_o^{+}VG_o^{+} + \ldots \tag{16}$$

$$|\Psi^{+}\rangle = |\Psi_o\rangle + G^{+}V|\Psi_o\rangle + G^{+}VG^{+}V|\Psi_o\rangle + \ldots \tag{17}$$

$$T = V + VG_o^{+}V + VG_o^{+}VG_o^{+}V + \ldots \tag{18}$$

The series expressed in equations (16) through (18) are usually called the Born series. The Born series expansions for G^{+}, $|\Psi^{+}\rangle$, and T can be used to calculate these quantities to the desired accuracy dependent upon one stipulation - that the Born series is a convergent series. The requirement of convergence is by no means quaranteed or, in most cases, is this convergence presently able to be shown. Several investigations have given inconclusive results concerning the convergence of the Born series,[35,36] and for the more than two colliding particles, the convergence properties of the Born series are not known in general.[63]

Now suppose a collision between atomic systems is represented by the following diagram. The bare ion projectile and target nuclei have masses

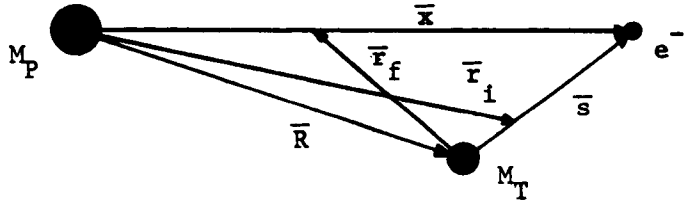

M_P and M_T, respectively, and are separated by a distance $|\bar{R}|$. The nucleus M_T, has charge +Ze, and one electron e^-, of mass m, and charge -e, bound to it. The bare ion projectile nucleus has charge +Z´e. The vector $\bar{r}_i$ represents the position of the center of mass of the M_T-e^- system relative

to M_P while $\bar{r}_f$ gives the position of the center of mass of the M_P-e^- system relative to M_T. Neglecting radiation, the energy and momentum are conserved among these three particles. If it is assumed that the electron is initially bound to the target nucleus M_T, and after the collision it is either moving away from M_T or in an excited state of M_T, then the total Hamiltonian H, for the system can be written as[34]

$$H = H_i + V_i, \tag{19}$$

where H_i is the sum of the kinetic energy operators and V_i includes all interaction perturbations. V_i can be written as

$$V_i = V_{M_T,e^-} + V_{M_P,e^-} + V_{M_P,M_T} \tag{20}$$

where,

$$V_{M_T,e^-} \equiv -\frac{Ze^2}{s}, \tag{21}$$

$$V_{M_P,e^-} \equiv -\frac{Z'e^2}{x}, \tag{22}$$

$$V_{M_P,M_T} \equiv \frac{ZZ'e^2}{R} \tag{23}$$

As mentioned in Chapter I, V_{M_P,M_T} is usually neglected, especially for high impact velocity collisions, since the internuclear potential should have negligible effect on the electron states. This approximation is generally called the Oppenheimer-Brinkman-Kramers (OBK) approximation. Oppenheimer[6] and Brinkman and Kramers[17] independently introduced this approximation at about the same time.

As stated in the discussion immediately following equation (4) on page 12, the Coulomb potential is specifically excluded from the class of potentials for which the Lippmann-Schwinger equation is valid because of its asymptotic behavior. In charge exchange processes, however, the Coulomb potential is the dominant perturbation potential in the interaction between electrons in the target atom and the projectile ion. In most calculations of charge exchange processes, a "screened Coulomb potential" is used in place of the normal Coulomb potential. This screened potential usually takes the form

$$V(r) = \lim_{\lambda \to 0} \frac{e^{-\lambda r}}{r} . \qquad (24)$$

The limit is applied only after all pertinent integrations and manipulations have been performed. This procedure is assumed to account for the infinite range of the Coulomb potential in such a way as to validate the method of approximations used in the preceding section. There is a question, however, concerning the legitimacy of this procedure since such a limiting process could introduce errors if the limit is not taken at precisely the correct point in the calculations.

In addition to the OBK approximation, another approximation is generally assumed when considering high energy ion-atom collisions. This is the assumption of a very small scattering angle for the projectile ion, for high energies, and can be taken into account classically by applying the impact parameter method for solving the scattering problem.[34]

For a projectile ion colliding with a target atom, the total cross section for a transition from an initial state i, to a final state f, is[34]

$$\sigma = \frac{\mu_i \mu_f}{4\pi^2 \hbar^4} \left(\frac{k_f}{k_i}\right) \int |T_{if}|^2 d\Omega \ , \tag{25}$$

where μ_i and μ_f are the reduced masses before and after the collision, $\hbar k_i$ and $\hbar k_f$ are the corresponding momenta, and Ω is the solid angle into which the electrons are emitted. The transition matrix T_{if}, is defined by applying equation (18).

$$T_{if} = \langle \psi_f | V_f (1 + G_i^+ V_i) | \psi_i \rangle \ . \tag{26}$$

Here, $|\psi_i\rangle$ and $|\psi_f\rangle$ are the initial and final state wavefunctions, respectively. The perturbations V_i and V_f, represent the interaction potential energies before and after the collision, respectively, and G_i^+ is the initial state Green's function operator defined by equation (13). When considering ECC, the initial state consists of a bare ion moving towards a target atom containing one bound electron, while the final state is comprised of the projectile ion plus an unbound electron moving away from the ionized target atom. The electron has a velocity nearly equal to the projectile ion velocity and it is moving in the forward direction, i.e., in the direction of motion of the projectile ion.

Coulomb Scattering

If $\psi_{\bar{k}'}(\bar{r})$ represents the wavefunction of an electron of momentum $p = \hbar\bar{k}'$, mass m, charge -e, and energy E, in the presence of a static potential $V(\bar{r})$, then $\psi_{\bar{k}'}(\bar{r})$ satisfies the Schrödinger equation given by[37,38]

$$\left[\nabla^2 - U_c(\bar{r}) + k'^2\right] \psi_{\bar{k}'}(\bar{r}) = 0, \tag{27}$$

where $U_c(\bar{r}) \equiv \pm \frac{2m}{\hbar^2}\frac{Z'e^2}{r}$, $k'^2 \equiv \frac{2mE}{\hbar^2}$, and ∇^2 is the Laplacian operator in spherical coordinates. $\pm Z'e$ is the charge of the particle exerting the Coulomb force on the electron. This equation can be separated into radial and angular equations. The solutions for the radial equation depend on whether the Coulomb potential $U_c(r)$, is attractive (-) or repulsive (+), and whether the energy E is negative or positive. Negative values of E correspond to bound states while unbound states are characterized by positive E. By transforming to parabolic coordinates, analytical solutions for both the bound and unbound states can be obtained in terms of functions known as confluent hypergeometric functions.[37,38] The normalized solutions are written as

$$\psi^{+}_{\bar{k}'}(\bar{r}) = \frac{1}{(2\pi)^{3/2}} e^{\frac{-\pi\alpha}{2}} \Gamma(1+j\alpha) e^{j\bar{k}'\cdot\bar{r}} \; {}_1F_1(-j\alpha;1;jk'r-jk'\cdot\bar{r}), \tag{28}$$

and

$$\psi^{-}_{\bar{k}'}(\bar{r}) = \frac{1}{(2\pi)^{3/2}} e^{\frac{-\pi\alpha}{2}} \Gamma(1-j\alpha) e^{j\bar{k}'\cdot\bar{r}} \; {}_1F_1(j\alpha;1;-jk'r-j\bar{k}'\cdot\bar{r}), \tag{29}$$

where $\psi^{+}_{\bar{k}}(\bar{r})$ and $\psi^{-}_{\bar{k}}(\bar{r})$ are the outgoing and incoming wave solutions, respectively, and $\alpha \equiv \frac{ZZ'e^2m}{\hbar^2k'}$. $\Gamma(1-j\alpha)$ is the gamma function[39] and ${}_1F_1$ is the confluent hypergeometric function.[38,39] Note that the energy dependence appears implicitly in the terms containing α. The bound state solutions can be shown to be directly related to the Laguerre polynomials.[37-39]

First Born Approximation

The Born theory discussed by Massey and Mohr[40] and Bates and Griffing[41] utilizes two approximations:[3] 1) The incident and outgoing waves describing the relative motion of the incident projectile and the target atom are assumed to be undistorted. This assumption is valid provided the electrostatic interaction energy is small compared to the energy of motion, i.e., the kinetic energy of the projectile. 2) The wavefunction of the target atom is undistorted by the incident projectile, either before or after the collision. This assumption is valid under two different physical circumstances: It is applicable if (a) the orbital velocity of the ionized electron is much smaller than the incident projectile velocity, or if (b) the electron-projectile electrostatic interaction energy is small compared to the kinetic energy of the electron in its bound orbit.

The cross section for a capture process is given by equation (25) where the transition matrix T_{if}, is defined by equation (26) and G_i^+ is given by the series in equation (16). The first Born approximation consists of neglecting G_i^+ in equation (26). This yields

$$T_{if} = \langle \Psi_f | V_f | \Psi_i \rangle . \tag{30}$$

This transition matrix is then inserted in equation (25) to give

$$\sigma = \frac{\mu_i \mu_f}{4\pi^2 \hbar^4} \frac{k_f}{k_i} \int |\langle \Psi_f | V_f | \Psi_i \rangle|^2 \, d\Omega \tag{31}$$

The wavefunctions $|\Psi_i\rangle$ and $|\Psi_f\rangle$ can be factored into terms describing internal states of the electron and center of mass motion of the two

nuclei, i.e.,

$$|\Psi_i> = |\Phi_i X_i> \text{ and } |\Psi_f> = |\Phi_f X_f> \ , \qquad (32)$$

where Φ describes the center of mass motion and X gives the internal state of the electron. The center of mass motion can be represented by a normalized plane wave while $X_{i,f}$ are represented as a Coulomb waves [see equation (29)], bound in the initial state and unbound in the final state. The results of a first Born calculation are shown in Figure 1 on page 5 and Figure 2 on page 7. The obvious discrepancy between the first Born calculation and the measured ejected electron distributions is due to the failure of the first Born approximation to account for the projectile-electron interaction after the collision.

Macek's Theory

Macek[12] proposed one of the earliest theories of ECC to describe the forward peaking in ejected electron spectra observed by Crooks and Rudd,[11] in which a pronounced forward peak was observed when the ejected electron velocity $\bar{v}_e$, was very nearly equal to the incident ion velocity $\bar{v}_p$. According to Macek's article, Rudd, extending a suggestion by Oldham,[10] first suggested that these electrons are carried along with the incident ion for some time before moving away from the ion as free electrons. Macek's theory was intended to give a theoretical basis for the continuum electron state in Rudd's proposed explanation and to show in what sense the electron in the continuum state was carried along by the ion. Macek assumed a 300 KeV proton incident on an atomic hydrogen target. In order to produce a qualitative explanation without extensive

calculations, a first order approximation was used. Macek calculated the cross section for ECC using a first order approximation of the Fadeev equation[42] since, in this formulation, all particles are treated on an equal footing.[12] This first order approximation describes an electron moving slowly away from the residual ion while the proton moves rapidly away, and also describes the proton and electron moving slowly away from each other, but both moving rapidly away from the residual ion. The first Born approximation, on the other hand, describes only the former of these two configurations of the final state. The initial state wavefunction is found to be the product of a bound Coulomb wave for the hydrogenic target plus electron system and a plane wave representing the incident proton. The final state wavefunction consists of four terms. The first is the product of three plane waves representing all three outgoing particles as free. The second term has two factors: one is a plane wave representing the incident proton and the other is a Coulomb wave for the hydrogenic target plus electron system. The third term is the same as the second except that the proton of the initial hydrogen target is represented as a plane wave and it is multiplied by a Coulomb continuum wave for the incident proton and the electron system. A fourth term can be combined with the first term by using the fact that the Coulomb plane wave of the incoming proton is essentially a plane wave and use of the OBK approximation, which neglects the incident proton-hydrogen nucleus interaction. Use of these wavefunctions results in a transition matrix element which consists of three terms,

$$T_{fi} = a_{23} + a_{12} - a \qquad (33)$$

where the subscripts 1, 2, 3, denote the incident proton, electron, and hydrogen target nucleus, respectively. The amplitude a_{23}, is the usual first Born amplitude describing ionization of the hydrogen target; a_{12}, is the amplitude describing transfer of the electron into a continuum state centered about the incident proton, and the third term a, is a term arising because the term with all outgoing particles represented as plane waves has been counted twice. After calculating each of the amplitudes, the doubly differential cross section $\frac{d^2\sigma}{dE_e d\Omega_e}$ was obtained by numerical integration. The results are shown in Figure 2 on page 7. The peak in the differential cross section is produced by a factor $|\bar{v}_e - \bar{v}_p|^{-1}$ in the amplitude a_{12}.

There are three significant features of this theory. 1) The physical processes of direct ionization and ECC are considered to be coherent processes, i.e., the amplitudes, not the cross sections, for each process are added. This is explicitly shown in equation (33). Because of this coherence, the processes of direct ionization and ECC cannot, even in principle, be separated from one another. This fact prevents the subtraction of any direct ionization contribution from an experimental ECC spectrum. 2) The electron velocity distribution at 0^o is symmetric about $|\bar{v}_e| = |\bar{v}_p|$ since the term $|\bar{v}_e - \bar{v}_p|^{-1}$ is symmetrical about $\bar{v}_e = \bar{v}_p$. 3) The dependence of the differential cross section on the projectile ion velocity is $<v_p^{-10}$, which is slightly greater than the v_p^{-11} dependence for bound state capture.[8]

Salin's Theory

Another first order theory was proposed by Salin[13] at about the same time as Macek. This theory was based on the first Born approximation for ionization modified to include distortion of the ejected electron

wavefunction by both the target nucleus and the projectile ion. Using an impact parameter approximation, Salin writes the final state wavefunction as a Coulomb wave distorted by the projectile ion. The doubly differential cross section in the laboratory frame can then be written as,

$$\frac{d^2\sigma}{dE_e d\Omega_e} = \left| N(|\bar{v}_e - \bar{v}_p|) \right|^2 \frac{d^2\sigma_{Born}}{dE_e d\Omega_e} , \tag{34}$$

where $\frac{d^2\sigma_{Born}}{dE_e d\Omega_e}$ is the cross section for the first Born calculation for ionization,[13,40,41] and

$$N(|\bar{v}_e - \bar{v}_p|) = \exp\left(\frac{\pi z Z'}{2v'}\right) \Gamma\left(1 + \frac{jz}{v'} Z'\right), \tag{35}$$

is the factor in the final state wavefunction of the ejected electron due to inclusion of the distortion by the projectile. Also, $Z' \equiv$ projectile nuclear charge (for bare ions), $\bar{v}' \equiv \bar{v}_e - \bar{v}_p$, and $z = 1 - v'/v_p$. $\bar{v}_e$ and $\bar{v}_p$ are defined on page 21. For the case $\bar{v}_e \cong \bar{v}_p$ equation (34) simplifies to,

$$\frac{d^2\sigma}{dE_e d\Omega_e} = \frac{\frac{2\pi Z'}{v'}}{1 - \exp\left(\frac{-2\pi Z'}{v'}\right)} \frac{d^2\sigma_{Born}}{dE_e d\Omega_e} \tag{36}$$

The result of calculations with equation (36) for 300 KeV protons incident on atomic hydrogen is shown in Figure 3. At $|\bar{v}_e| \cong |\bar{v}_p|$, the energy of the ejected electrons corresponds to 163 eV as calculated from equation (1) on page 5. The figure shows quite evidently that the doubly differential cross section of (36) exhibits a sharp peak peak at 0^o for ejected electron energies close to this energy. As seen from (36), the resultant peak is symmetric, i.e., $\frac{d^2\sigma}{dE_e d\Omega_e}$

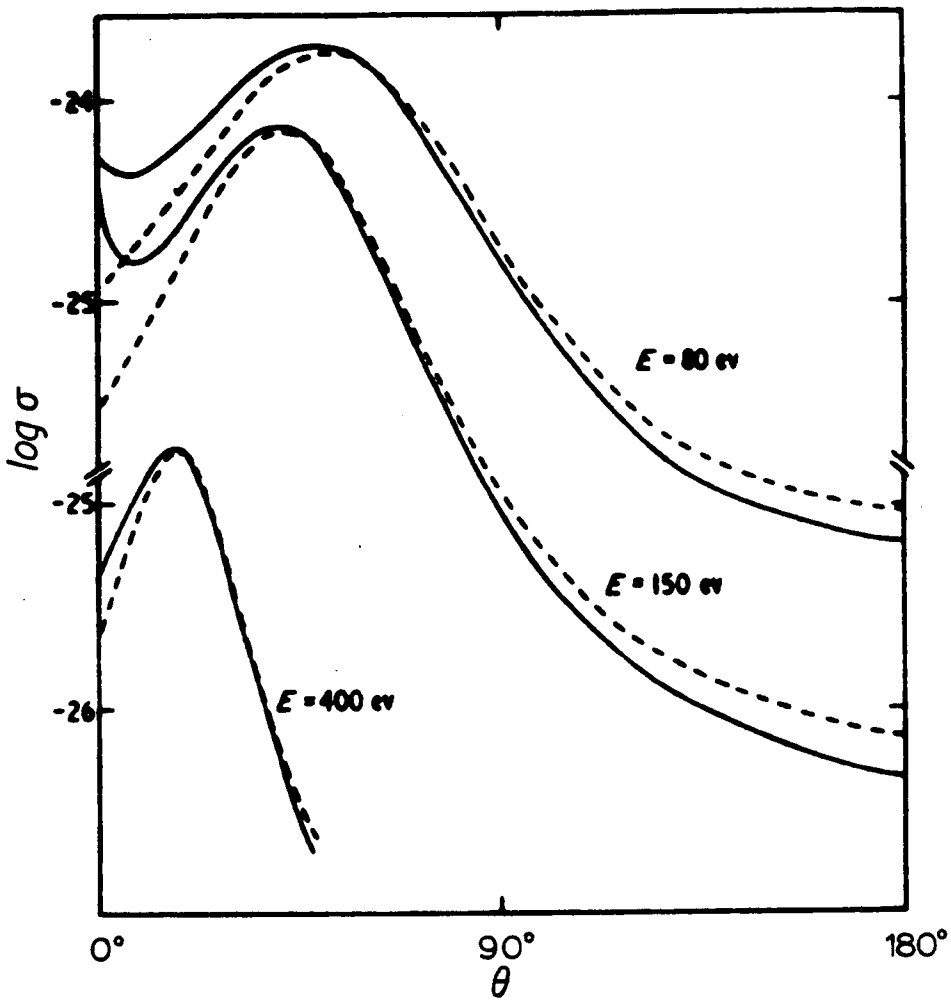

Figure 3. Differential Cross Section at Forward Angles for 300 keV Protons incident on Atomic Hydrogen. (Reproduced from reference 13).

$\frac{d^2\sigma}{dE_e d\Omega_e}$ ——— Salin[13] [calculated from equation (36)].

------- First Born approximation of Bates and Griffing.[41]

depends only on the magnitude of $\bar{v}_e - \bar{v}_p$. Note that the peak is produced by the factor $\frac{1}{|\bar{v}_e - \bar{v}_p|}$, not by $\frac{d^2\sigma_{Born}}{dE_e d\Omega_e}$ which is shown as the dotted line in Figure 3.

Dettmann's Theory

Using a T-matrix formulation, Dettmann, et al.[18] obtained an analytical form from the differential cross section for ECC using a second order Born approximation. A bare projectile ion was considered to be incident on a hydrogenic target atom. The projectile energies considered are high enough so that the projectile undergoes essentially rectilinear motion and the OBK approximation was also employed. In the T-matrix formulation, the doubly differential cross section is obtained from equation (25).

$$\frac{d^2\sigma}{dk d\Omega_e} = \frac{k_f}{K_i} \frac{\mu^2}{4\pi^2\hbar^4} \left| T_{if} \right|^2, \tag{37}$$

where T_{if} is defined by equation (26) and Ω_e is the solid angle into which the electrons are emitted. $\hbar\bar{K}_i$ and $\hbar\bar{k}_f$ are initial and final relative momenta of the colliding systems, respectively, and μ is the reduced mass of the projectile-target system. The incoming projectile has mass M' and nuclear charge Z', while the target atom has mass M, nuclear charge Z, and contains one bound electron of mass m. The incoming state consists of the product of a free plane wave, and the initial bound state wavefunction of the electron, i.e., a bound Coulomb wave. The final state consists of the target nucleus in a free state relative to the projectile-electron system and the electron in an advanced continuum state centered around the projectile. The electron final state can be written as an unbound Coulomb wave as shown on page 19. The dependence on projectile

nuclear charge Z' is contained in this Coulomb wave. If $\hbar\bar{k}'$ is the momentum of the electron relative to the projectile, then for $h\bar{k}'\to 0$ the differential cross section can be written as,

$$\frac{d\sigma}{d\bar{v}_e} = f(\bar{v}_e)F(\bar{v}_p,\hat{k}'), \tag{38}$$

where $\bar{v}_e$ is the electron velocity in the laboratory frame, $\bar{v}_p$ is the projectile velocity, and

$$f(\bar{v}_e) = \frac{\pi\alpha e^{\pi\alpha}}{\sinh\pi\alpha}\ . \tag{39}$$

Also, $\alpha \equiv \frac{Z'}{a_B k'}$ and a_B = Bohr radius. $F(\bar{v}_p,\hat{k}')$ is related to the second Born transition matrix $T_{if}^{(2)}$, by

$$F(\bar{v}_p,\hat{k}') = \frac{m^3}{\hbar^3}\frac{v^2}{4\pi^2\hbar^4}\int|\tilde{T}_{if}^{(2)}|^2 d\Omega', \tag{40}$$

where Ω' is the solid angle in the projectile frame, and

$$\tilde{T}_{if}^{(2)} \equiv \frac{T_{if}e^{-\pi\alpha}}{\Gamma(1-j\alpha)} = \langle\tilde{\Phi}_f^-|V_1G_oV_2|i,\bar{K}_i\rangle. \tag{41}$$

$|i,\bar{K}_i\rangle$ is the incoming state with momentum $\hbar\bar{K}_i$ and $|\tilde{\Phi}_f^-\rangle$ represents the final state. V_1 and V_2 are screened Coulomb potentials for the target nucleus-electron and projectile ion-electron interaction, respectively. G_o is the free particle Green's function operator given in equation (12). $\Gamma(1-j\alpha)$ is a gamma function arising from the normalization of the unbound Coulomb wave of the final state $|\tilde{\Phi}_f^-\rangle$ [see equation (29)]. The factor $f(\bar{v}_e)$, contains the term $\frac{1}{|\bar{v}_e-\bar{v}_p|}$ since it can be shown that (39) can be reduced to

$$f(\bar{v}_e) = \frac{2\pi\alpha}{1 - e^{-2\pi\alpha}} . \qquad (42)$$

For small forward scattering angles $\Theta_o \ll \pi$, and for $Z'v_B > v_p\Theta_o$, for $\bar{v}_e \cong \bar{v}_p$, $f(\bar{v}_e)$ can be finally reduced to

$$f(\bar{v}_e) \simeq \frac{2\pi Z' v_B}{|\bar{v}_e - \bar{v}_p|} , \qquad (43)$$

where $v_B \equiv \frac{\hbar}{a_B m}$ = Bohr velocity. Using (43) in (38) and integrating over a solid angle cone of half angle Θ_o, gives

$$\frac{d\sigma(\Theta_o)}{dv_e} = F(v_p) 4\pi^2 Z' v_B \left\{ \left[(v_e - v_p)^2 + v_p^2 \Theta_o^2 \right]^{-\frac{1}{2}} - |\bar{v}_e - \bar{v}_p| \right\} \qquad (44)$$

where in the high energy limit used here $F(\bar{v}_p, \hat{k}') = F(v_p)$. Using the second Born approximation to obtain $F(v_p)$ from equation (37), with the additional assumptions included in the high energy treatment, $\frac{m}{M} \ll 1$, and $\frac{M'}{M'+m} \simeq M'$, the final result for $F(v_p)$ for projectile ions is

$$F(v_p) = \frac{2^{16}}{10\pi^2} \frac{Z^2 Z'^2}{v_i^3} \left(\frac{v_B}{v_p} \right)^{12} \pi a_B^2 \left[0.3 + \frac{10\pi}{2^{12}} \frac{v_p}{v_i} \right] , \qquad (45)$$

where $E_i = \frac{1}{2} m v_i^2$ is the binding energy of the electron in the target atom. Combining (45) with (44) it is found that a symmetric cusp of full width half maximum $\frac{3}{2} v_p \Theta_o$ results. The cusp shape information is contained only within the expression for $f(\bar{v}_e)$. As seen from equation (41), the second Born expression for the transition matrix element $\tilde{T}_{if}^{(2)}$ describes a two-step scattering process; the first being the scattering of m by M' with interaction potential V_2 and the second, the subsequent collision of m with M and interaction potential V_1. Predictions of this theory are the

following: 1) The cross section in equation (44) yields a symmetric distribution about $\bar{v}_e = \bar{v}_p$ since only $|\bar{v}_e - \bar{v}_p|$ appears in the final result. 2) The full width at half maximum of the cusp-shaped distribution in equation (44) is $3/2\ v_p\Theta_o$ where Θ_o is the finite angular acceptance of the particular experimental apparatus being used to scan the electron spectrum. 3) $\frac{d\sigma}{dv_e}$ varies as v_p^{-12}.

Chan and Eichler Theory

The three theories discussed so far predict a symmetric cusp-shaped differential cross section in the laboratory frame. However, as found by several experiments,[14,15,43] the differential cross section exhibits a decidedly asymmetric cusp shape which is skewed toward lower electron velocities. Although Dettmann, et al.[18] included the second Born term in the differential cross section, the final state Coulomb wavefunction was simplified by using a series expansion for the Coulomb wave, letting $k' \to 0$, and retaining only zero order terms in k'. Chan and Eichler[19] later obtained an asymmetric cusp for the same collision system by using Dettmann's expression for the cross section. However, upon evaluating the final wavefunction, first order terms in k' were retained. The resulting cross section is given by

$$\frac{d\sigma}{dv_e} = 2^7 Z'^3 \int \frac{d\Omega_e}{|\bar{v}_e - \bar{v}_p|} \int_{v_p/2}^{\infty} \frac{1}{1 - \frac{2k' \cdot K}{K^2}} \frac{dK}{K^{11}} \qquad (46)$$

where $\hbar\bar{k}'$ ≡ momentum of electron in the projectile frame, and $\hbar\bar{K}$ ≡ momentum transferred to the projectile.

The Dettmann expression for the cross section in equation (44) can be recovered from equation (46) if the scalar product $\frac{\bar{k}' \cdot \bar{K}}{K^2}$ is disregarded. The asymmetry of the cusp obtained from equation (46) is predicted to approach zero as $\bar{v}_p \to \infty$ (asymptotically high projectile velocities) and $\frac{d\sigma}{dv_e}$ varies as v_p^{-10}.

Shakeshaft and Spruch Theory

Shakeshaft and Spruch,[20] following the same T-matrix formalism as Dettmann, et al.,[18] obtained an asymmetric cusp-shaped peak for the differential cross section for a bare carbon ion incident on atomic hydrogen. The final state wavefunction consisted of an unbound Coulomb wave centered around the projectile ion, but when letting $k' \to 0$, an expression relating the confluent hypergeometric function to the zero order Bessel function J_o, was used rather than the Kummer's series[39] used by Dettmann, et al.[18] Shakeshaft and Spruch[20] also state that Dettmann, et al.[18] have an error in the evaluation of the second Born matrix element $T_{if}^{(2)}$. The combination of these two differences causes the disagreement between Dettmann, et al.[18] and Shakeshaft and Spruch.[20] Also, this theory predicts a v_p^{-11} dependence of the differential cross section.

Shakeshaft and Spruch emphasize that the second Born term is expected to dominate the first Born term for high impact velocities.[7,20] Also, for capture into a true bound state, the first Born amplitude $T^{(1)}$, is proportional to $\frac{1}{v_p \ell'}$ where ℓ' ≡ angular momentum quantum number of the final bound state. The second Born amplitude $T^{(2)}$, however, is independent of ℓ'. The relative probability for capture into a bound state with $\ell' \neq 0$ compared to a bound state where $\ell' = 0$ varies as $\frac{1}{v_p^{2\ell'}}$. Shakeshaft and Spruch argue that this should be true for continuum capture

as well by reason of continuity since this probability should vary smoothly across the bound state-to-continuum boundary. The reason that the second Born term leads to an asymmetric distribution is said to be the following. Since the amplitude $T^{(1)}$, decreases $\frac{1}{v_p}$ only the $\ell' = 0$ component will be important at high velocities. Therefore, $T^{(1)}$ is expected to be isotropic in the vector $\bar{v}_e - \bar{v}_p$. $T^{(2)}$, on the other hand, has contributions from many different angular momentum components of the continuum; because of this, the part of the cross section due to $T^{(2)}$ is expected to depend on both the magnitude and direction of $\bar{v}_e - \bar{v}_p$. This anisotropy is said to be the direct cause of the asymmetry observed in the experimental ECC cusps.

A comparison of the theories of Dettmann, et al.,[18] Chan and Eichler,[19] and Shakeshaft and Spruch[20] is shown in Figure 4 for 2 MeV/u bare carbon ions ($Z'=6$) incident on atomic hydrogen.

As seen from the figure, both the Shakeshaft and Spruch (SS) and the Chan and Eichler (CE) cusps are asymmetric while the Dettmann, et al. (D) cusp is symmetric. Although the (SS) and (D) cusps are predicted to retain the same shape as the projectile velocity increases, the (CE) cusp becomes more symmetric as this velocity increases. Recent experiments[43,44] have shown that, at least to the limit of the projectile velocities studied, no significant symmetrization occurs as the projectile velocity is increased, a fact which does not seem to support the theory of Chan and Eichler.[19]

Jakubassa-Amundsen Theory

Jakubassa-Amundsen[21] has calculated the doubly differential cross section for electrons captured from a hydrogenic target to continuum states of a fast, heavy, bare ion projectile. A semiclassical impact parameter

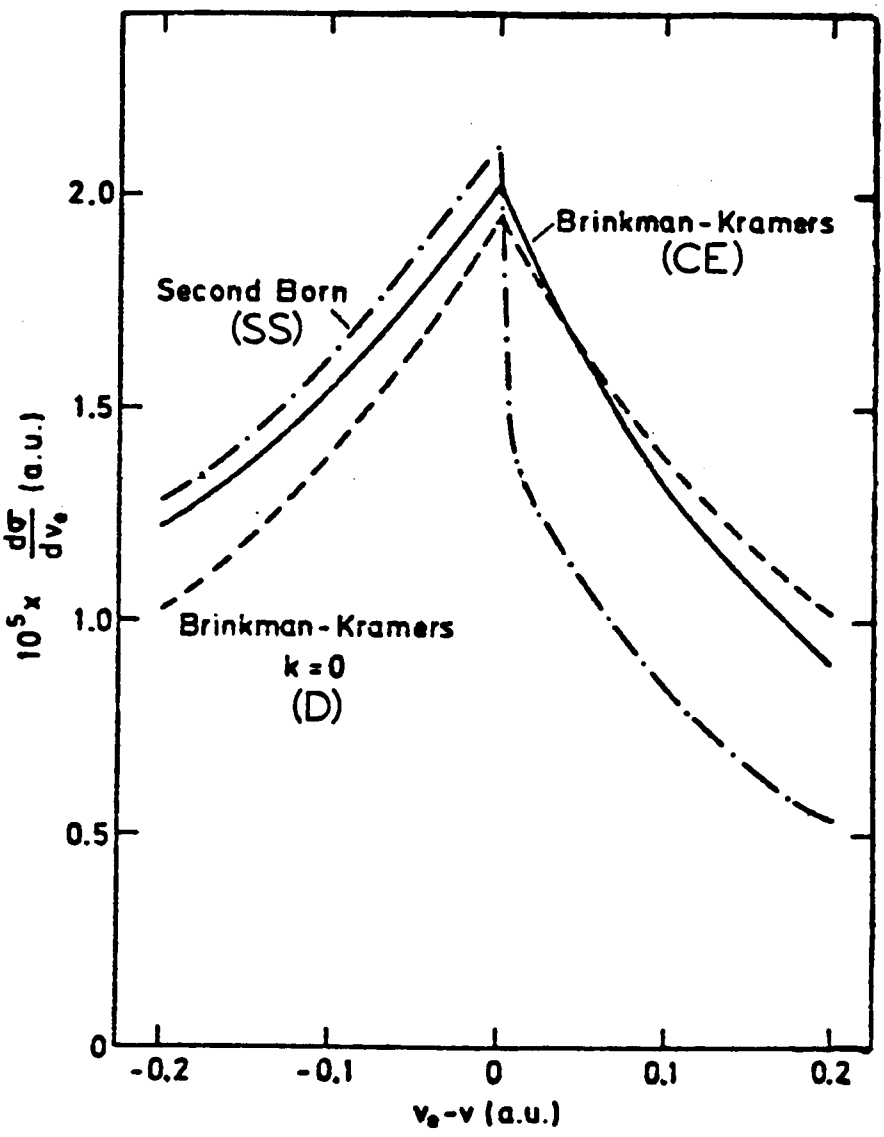

Figure 4. Comparison of Three ECC Theories.

Singly differential cross section for continuum electron capture from the 1s state of a hydrogen atom by a bare ion of $Z'=6$ incident with an energy of 2 MeV/nucleon in the laboratory frame. In the cross section, electrons are accepted which emerge into a cone of semiangle $\theta_o = 1.85^o$. The solid curve, marked "Brinkman-Kramers" represents the OBK result of Chan and Eichler[19] (CE) [equation (46)], and the dashed curve, the OBK results of Dettmann, et al.[18] (D) [equation (44)]. The dash-dotted curve gives the contribution to the differential cross section of Shakeshaft and Spruch[20] (SS) from the sum of the first- and second-order Born terms, however, without inclusion of the $\bar{k}\cdot\bar{K}$ terms in the first Born (OBK) amplitude. (Reproduced from reference 19)

theory is used to describe the internuclear motion which is characterized by a classical time dependent trajectory. A semiclassical impulse approximation (SCIA) is applied to continuum charge transfer but no high velocity approximation is used. By assuming collisions between very asymmetric systems where the electron spectrum is produced predominantly by an unbound electron moving in the field of the projectile, i.e., continuum electrons, this impulse approximation can be used.[45] In this context, the term "asymmetric," signifies that the projectile charge Z', is much greater than the target charge Z, i.e.,

$$Z' \gg Z. \tag{47}$$

The impulse approximation assumes that the interaction potential V_{13}, between the projectile and the electron bound to the target atom is much stronger than the interaction potential V_{23}, between the electron and the target nucleus where the projectile, target nucleus and electron are designated as particles 1, 2, and 3, respectively. Then the total Hamiltonian for the system can be written as,

$$H = H_o + V_{23} + V_{13}, \tag{48}$$

where H_o is the sum of the kinetic energy operators. In the region of the target nucleus, the potentials V_{13} and V_{23} can be written as

$$V_{23} = -\frac{Ze}{r_{23}} \text{ and } V_{13} = -\frac{Z'e}{r_{13}} \tag{49}$$

where r_{13} and r_{23} represents the distance between the projectile and electron and the target nucleus and the electron, respectively. The impulse approximation assumes that $V_{13} \gg V_{23}$ from which the condition

given by (47) arises for $r_{13} \cong r_{23}$. Generalizing the theory for the capture of an electron by a heavy projectile[22] in the impulse approximation to that for ECC, Jakubassa-Amundsen[21] writes the doubly differential cross section for impact parameter $\bar{b}$ as

$$\frac{d^2\sigma}{d\varepsilon_f d\Omega_f} = K_f \int d^2\bar{b} \, |a_{fi}|^2, \tag{50}$$

where $\varepsilon_f = \frac{\hbar^2 K_f^2}{2m}$ is the final energy of the electron, Ω is the solid angle into which it is emitted, and $\hbar\bar{K}_f$ is the final momentum of the electron in the projectile frame. The expression for the transition amplitude a_{fi}, is evaluated by inserting projectile centered unbound Coulomb waves for the final state wavefunction of the electron. A peaking approximation[22] is used to simplify evaluation of the integrals. This approximation assumes that the emitted electron momentum distribution occurs predominantly in the forward direction. The differential cross section in the projectile frame is found to be

$$\frac{d^2\sigma}{d\varepsilon_f d\Omega_f} \alpha \frac{Z'/K_f}{1 - \exp\left(\frac{-2\pi Z'}{K_f}\right)} \int |M_{if}|^2, \tag{51}$$

where M_{if} is a matrix element for the transition to the continuum state by the electron. The quantity $\hbar\bar{K}_f$ is the final electron momentum in the projectile frame and can be written as,

$$\frac{\hbar K_f}{m} = \left|\frac{\hbar}{m}\bar{k}_f - \bar{v}_p\right|, \tag{52}$$

where $\hbar\bar{k}_f$ is the final electron momentum in the target frame. This term will produce a singularity as $\frac{\hbar\bar{k}_f}{m} = \bar{v}_p$ which will cause a symmetric

cusp-shaped peak in the cross section. However, there is another singularity at $\frac{\hbar\bar{k}_f}{m} = \bar{v}_p$ in the matrix element M_{if}, appearing in the cross section. For electrons emitted at 0^o, the hypergeometric function ${}_2F_1$, used in the expression for the unbound Coulomb wave, has a discontinuity at $\frac{\hbar\bar{k}_f}{m} = \bar{v}_p$, i.e.,

$$ {}_2F_1 \begin{cases} <1 \text{ for } \frac{\hbar k_f}{m} \to v_p \\ \\ \simeq 1 \text{ for } \frac{\hbar k_f}{m} \to v_p \end{cases} \begin{matrix} \\ -0 \\ \\ +0 \end{matrix} . \tag{53} $$

This discontinuity produces an asymmetric cusp-shaped peak in the cross section and it has been explained by Lucas[34] in terms of a transformation to the projectile frame. In this frame, electrons with $\frac{\hbar}{m} k_f < v_p$ are emitted in the same direction as the target motion and electrons with $\frac{\hbar}{m} k_f > v_p$ move in a direction opposite to the target motion. The action of the target potential causes the intensity of the lower velocity electrons to be enhanced relative to the higher velocity electrons, thus producing an asymmetric cusp.

Jakubassa-Amundsen compares the numerical results of equation (51) with a second order Born calculation of Miraglia and Pounce[46] given by

$$ \frac{d^2\sigma_{MP}}{dE_f d\Omega_f} = \frac{2\pi Z'/K_f}{1 - \exp\left(\frac{-2\pi Z'}{K_f}\right)} \frac{d^2\sigma_{Born}}{dE_f d\Omega_f}, \tag{54} $$

where $\frac{d^2\sigma_{Born}}{dE_f d\Omega_f}$ is the result from a first Born approximation calculated by Jakubassa-Amundsen.[21] Jakubassa-Amundsen states that the Miraglia

and Ponce result includes higher order contributions from the projectile field through the nomalization constant used in the projectile wavefunction. A comparison of $\frac{d^2\sigma_{MP}}{dE_f d\Omega_f}$, $\frac{d^2\sigma_{Born}}{dE_f d\Omega_f}$, and the cross section in equation (51) is shown in Figure 5. The binary encounter peak shown in the figure is the energy-momentum conservation peak. As mentioned in Chapter I, this peak occurs due to the elastic collision of a stationary free electron with a much heavier particle. The resultant energy of the electron is such that it has a velocity almost twice that of the incoming heavy particle. The velocity of the incoming bare krypton ion is high enough so that the bound state energy of the electron is considered negligible.

As seen from the figure, $\frac{d^2\sigma_{Born}}{dE_f d\Omega_f}$ fails to produce the peak entirely at $\frac{\hbar}{m} k_f = v_p$ but describes the binary encounter peak well. The SCIA theory falls in between the first order Born calculation and the Miraglia and Ponce theory.

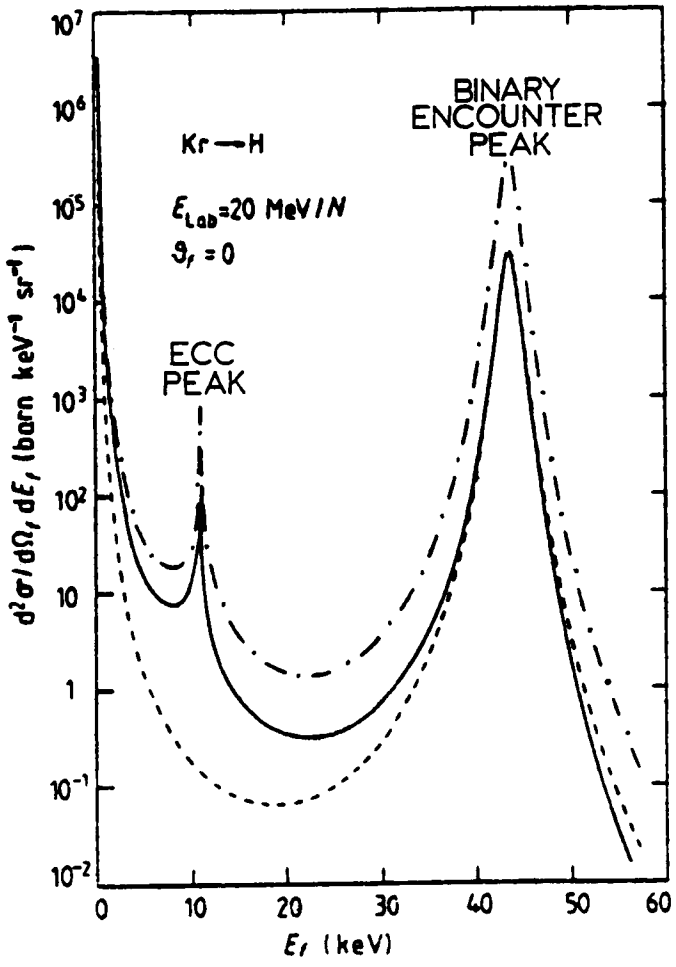

Figure 5. Semi-Classical Impulse Approximation ECC Spectrum.

Cross section for electron emission in collision of Kr with H at a collision velocity of $v_p/C = 0.2065$ as a function of electron energy at zero emission angle. The full curve denotes the SCIA theory (equation 51), the broken curve is the first Born theory and the dash-dot curve is the Miraglia-Ponce theory (equation 54). (Reproduced from reference 21.)

CHAPTER III

EXPERIMENTAL METHODS AND APPARATUS FOR ECC MEASUREMENTS

Description of Experiment

As discussed in Chapter I, ECC is one of the physical processes by which a projectile ion, through an interaction with a target atom, strips at least one electron from the target atom. The ECC electron(s) stripped from the atom subsequently has a velocity with magnitude and direction nearly equal to that of the projectile ion. If that electron is not in a bound state of either the projectile ion or target atom it is assumed to originate from the ECC process. The energy distribution of ECC electrons assumes the cusp shape shown in Figure 4 on page 32.

The acquisition of an ECC spectrum imposed several constraints on the experimental apparatus: 1) The entire experimental system, including the projectile ion source, generally demanded the maintenance of high vacuum, with certain parts of the system requiring ultra-high vacuum. 2) The ECC electrons produced by the interaction of the projectile ion beam with the atomic hydrogen target gas had to be collected efficiently and the data stored. The number of electrons collected must be related in an easily calculable manner to the ECC cross section. This electron collection system required a spectrometer which could distinguish electrons with nearly equal energies, and traveling in the same direction as the ion beam. An energy spectrometer was used instead of a velocity spectrometer because of certain physical limitations of the chamber in which the spectrometer was to be placed and because the energy spectrometer was readily available. Also, it was doubtful how well certain components

of a velocity spectrometer would withstand blackbody radiative heating due to the dissociation oven. Actual data acquisition required the use of the spectrometer in conjunction with electronic control systems. 3) An atomic hydrogen target was required. The oven developed for this study is discussed in Chapter IV. 4) A gas handling system capable of delivering ultrapure gas to the ion-target interaction region of the oven was required. This gas handling system was required to maintain a preset gas flow into the oven so that the target density in the interaction region could be determined accurately. 5) A collimating system was necessary to prevent the ion beam from striking any surfaces near the oven or electron spectrometer.

The path of the ion beam through the experimental beamline and the interaction of the ion beam with various apparatus can be summarized, quite generally, in the following way.

The ion beam was tightly collimated upon entering the H-oven beamline. ECC electrons were produced by the interaction of the projectile ions with the gas inside the oven. These electrons were emitted within a narrow cone in the forward direction and traveled toward the entrance of the electron spectrometer. The radial electric field between the sectors of the spectrometer deflected the ECC electrons while the ion beam continued on through a hole in the outer sector of the spectrometer. Electrons having an energy appropriate for the voltage on the spectrometer sectors followed essentially circular paths through the spectrometer and were detected by a channel electron multiplier (CEM) positioned at the exit of the spectrometer. The ion beam was ultimately collected in a Faraday cup placed at the end of the beamline.

Detailed descriptions of the methods and apparatus used in this study will be given in the remainder of this chapter.

Projectile Ion

Determination of the energy and ion species of projectile to be used was based on several factors. All of the theories in Chapter II, with the exception of the SCIA theory of Jakubassa-Admundsen,[21] assume that the final laboratory energy of the continuum captured electron is much greater than the initial bound state energy of the electron in the hydrogen atom, i.e., $\frac{1}{2}mv_p^2 \gg Z_H^2 e^2/a_B^2$, where $a_B \equiv$ Bohr radius, $Z_H = 1$, $v_p \equiv$ projectile velocity, $m \equiv$ electron mass, and $e \equiv$ electron charge. This condition can be written alternatively as $v_p \gg v_B$, where $v_B \equiv$ Bohr velocity. In terms of atomic units of velocity, $v_p \gg 1$ au $= 7.296 \times 10^{-3} c$ where $c \equiv$ velocity of light. In order that the experimental ECC spectrum could be compared with theory, two conditions were necessary: 1) $v_p \gg 1$ au, and 2) the projectile must be a bare ion. The latter condition is an experimental requirement imposed so that the competing process of electron loss to the continuum by the projectile ion can be eliminated from the interaction since electrons cannot be "lost" by a bare ion. Also, most theories consider only bare ion projectiles, and the SCIA theory of Jakubassa-Amundsen assumes that $Z_p \gg Z_H$, where $Z_p \equiv$ projectile ion nuclear charge.[21] Fulfilling condition 1) is limited by practical considerations. The EN Tandem accelerator at ORNL could efficiently produce bare ion projectiles of elements with a nuclear charge of eight or less. This restricts the available projectile beams to elements no heavier than oxygen. Also, as seen from Chapter II, the ECC cross section increases with increasing projectile nuclear charge and decreases with projectile

energy.[18] These factors have a direct bearing on the data acquisition rates. Therefore, the energy and ionic species of the projectile beam were chosen to be the most satisfactory combination consistent with theoretical considerations and reasonable data acquisition rates. The projectile beam finally chosen was 12 MeV C^{6+}. The projectile velocity corresponding to this energy is 6.3 au, and the electron laboratory energy at the peak of the ECC spectrum is found to be 544.4 eV by use of equation (1) on page 5.

Experimental Configuration and Vacuum Systems

The 12 MeV C^{6+} ion beam was produced by the ORNL EN Tandem accelerator and was magnetically analyzed by two calibrated magnets to insure a high purity beam before entering the experimental beam line. The first magnet encountered out of the acceleration region of the EN Tandem used the nuclear magnetic resonance technique to calibrate the magnetic field required for ions of a given charge to mass ratio and kinetic energy. The ion beam was bent through an angle of 90^{o} when passing through this analyzing magnet and most of the "cleaning" of the beam of unwanted charge states was performed by this magnet. The second magnet was a 90^{o} bending magnet designed to steer the ion beam to one of several experimental beam lines. Further purging of the undesirable charge states in ion beam was obtained when the beam passed through this magnet. Vacuum of $1x10^{-6}$ Torr was maintained throughout this accelerating and analyzing system.

Upon exiting the second magnet the ion beam entered the beamline containing the apparatus for the H-oven experiment. This portion of the beamline is shown in Figure 6. The beamline was maintained under high

Figure 6. Hydrogen Oven Beam Line

C1	First set of collimating (1.0 mm) apertures
C2	Second set of collimating (0.33 mm) apertures
D	Horizontal deflection plates
OVEN	Atomic Hydrogen Dissociation Oven
PL	Photon Limiters (1.67 mm diameter)
DP 1,2,3	Diffusion Pumps
Q1, Q2	Magnetic Quadrupole Beam Focusing Elements

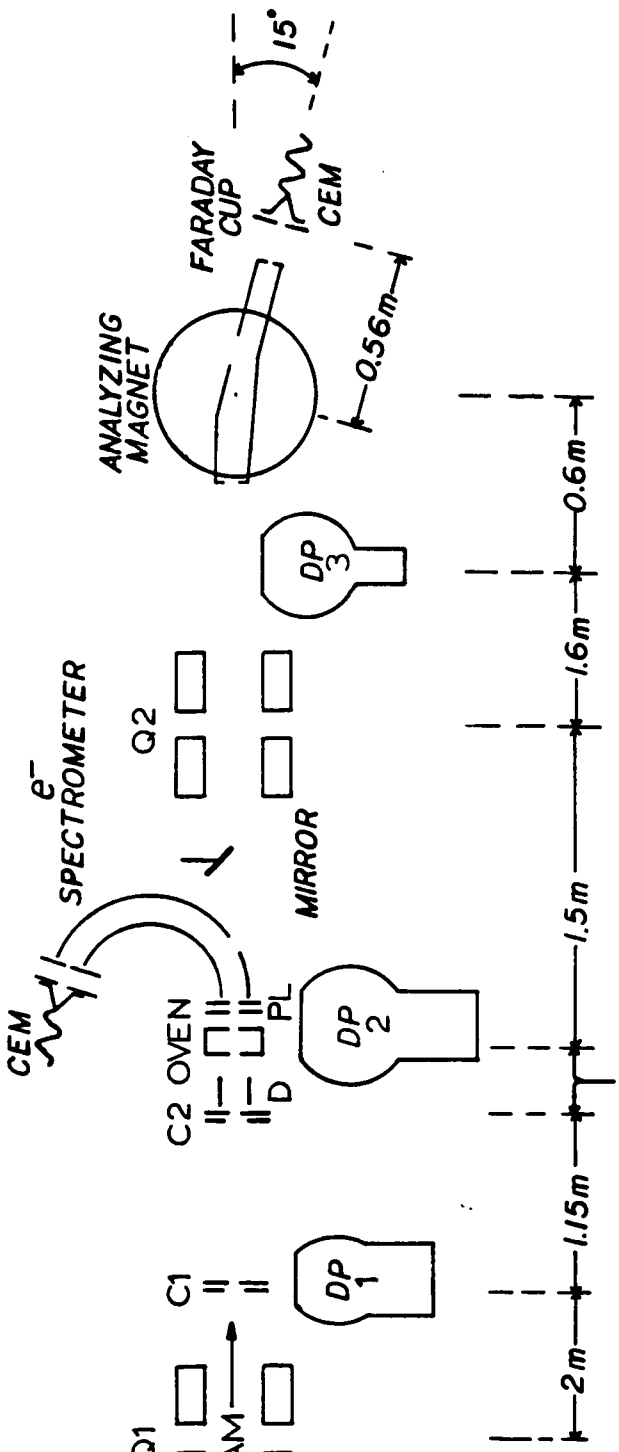
Q1
BEAM
C1
DP 1
C2 OVEN
D
PL
DP 2
CEM
e⁻ SPECTROMETER
Q2
MIRROR
DP 3
ANALYZING MAGNET
FARADAY CUP
CEM
15°
0.56m
2m
1.15m
13cm
1.5m
1.6m
0.6m

Figure 6.

vacuum by three Varian oil diffusion pumps denoted by DP in Figure 6. The pump sizes were 6", 8", and 6" for DP1, DP2, DP3, respectively. The typical vacuum at DP1 was 2×10^{-7} Torr, at DP2, 3×10^{-8} Torr, and at DP3, 1×10^{-6} Torr. All diffusion pumps had liquid nitrogen cryotraps which were kept filled during data acquisition and vacuum lines between forepumps and diffusion pumps contained oil traps to prevent back-streaming of forepump oil into diffusion pumps.

After passing through a magnetic quadrupole doublet lens the beam encountered the first collimator denoted as C1 in Figure 6. This collimator actually consisted of a set of two circular apertures of 2 mm and 1 mm diameters separated by $\sim$3 mm, the 2 mm aperture being encountered first by the beam. The 1 mm aperture was held at ground potential while the 2 mm aperture was connected to a ammeter in the Tandem control room via electrical feedthroughs in the vacuum flange. This setup provided a means by which the beam could be more easily monitored through the apparatus. Immediately preceding the hydrogen oven was another two aperture collimator set consisting of a 2 mm and a 0.33 mm aperture separated by $\sim$3 mm. This set is denoted by C2 in Figure 6. This first of these two apertures was also electrically isolated in order that beam current could be monitored. The actual beam collimation was accomplished by the second aperture in each set, i.e., the 1 mm and 0.33 mm aperture.

The ion beam next passed through the interaction region in the oven, and subsequently, through the photon limiters (PL in Figure 6). For a description of the function of these photon limiters see Chapter IV,

page 105. Immediately after the photon limiters, the beam entered the spherical sector electrostatic electron spectrometer at the midpoint of the analyzer sector separation. This spectrometer is described more fully in a later section in this chapter. The continuum electrons produced in the oven were separated from the ions and were analyzed by the electron spectrometer. The ion beam, which was negligibly deflected by the electric field in the spectrometer passed through a 0.32 cm diameter hole through the outside sector and continued through another magnetic quadrupole doublet lens prior to entering the Faraday cup.

Oven Vacuum Chamber

The chamber containing the atomic hydrogen oven and the electron spectrometer was a six-way stainless steel cross with 10" diameter Conflat^{R} flanging. The bottom flange of the cross bolted on to an 8" Varian oil diffusion pump (DP2 in Figure 6) with a liquid nitrogen cryotrap between the chamber and the diffusion pump. Typical pressure in the oven chamber of 3×10^{-8} Torr with the oven off and 9×10^{-8} Torr with the oven hot (no gas flowing into the oven) was measured by a standard ionization vacuum gauge. Partial pressures of impurities in the oven chamber could be monitored with a Residual Gas Analyzer (RGA). The oven was supported vertically from above by a high precision XYZ manipulator which allowed for placement of the oven in front of the 160° spherical sector electrostatic electron analyzer. The electron analyzer mounting required that the electron trajectories through it would lie in a horizontal plane. Magnetic field nulling was accomplished using a cubical coil arrangement (described in more detail on page 62).

One of the two gas feeds from the gas handling system (see page 53) was connected to the oven supporting rod and the other was connected directly to the chamber via a small flange in the upper cross flange.

ECC Data Acquisition

In order to be able to obtain a differential cross section for ECC an atomic hydrogen with reasonably well-predicted associated errors, data was required for two pertinent measurements. The first of these was the actual measurement of the number of continuum electrons produced as a function of energy when an ion beam traversed the target gas in the oven. The second measurement was the resolution calibration of the 160^{o} spherical sector electron spectrometer. The first measurement required an ion beam, while the second was performed using an electron beam produced by an electron gun; however, the electronics used in both measurements was basically the same. The following general description refers to the acquisition of data for the counting of continuum electrons but only small changes are necessary to include resolution calibration of the electron spectrometer.

The block diagram of the electronics is shown in Figure 7. The ion beam passed through the oven and electron analyzer, and subsequently entered the Faraday cup. The beam was forced to hit the walls of the Faraday cup by appropriately setting the magnetic field of the magnet in which the chamber containing the Faraday cup was positioned. The ion current thus collected was measured by an electrometer which amplified the current and sent it to a current digitizer. Pulses from the digitizer were sent to a timer/scaler which served as the "clock" for

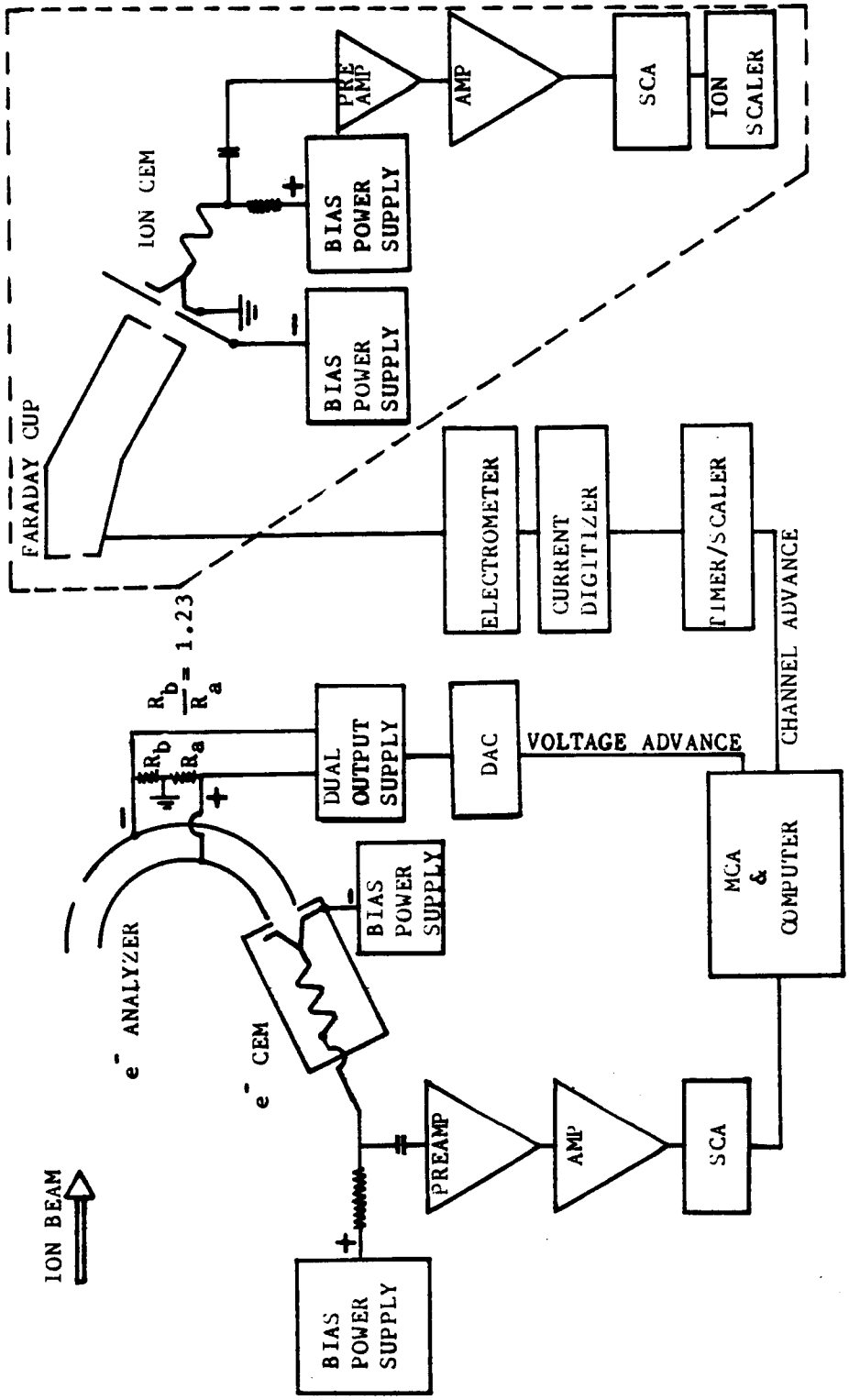

Figure 7. Block Diagram of Electronics.

the data acquisition system. The electron analyzer was supplied voltage by the dual output power supply with polarities to the analyzer sectors as shown in Figure 7. The resistors R_a and R_b, acted as a voltage divider which forced the potential at the circular arc midway between the two analyzer sectors to be at ground potential. The theoretical value for the ratio R_b/R_a is determined by the physical dimensions of the sectors. The energy spectrum to be studied was divided into a specific number of equally spaced energies by the digital-to-analog converter (DAC). A particular energy was obtained by adding a constant energy increment to the preceding lower energy. Each energy corresponded to a specific channel in the multichannel analyzer (MCA). The electron energy being analyzed by the spectrometer was directly proportional to the voltage on the sectors. This constant of proportionality is called the analyzer constant and is discussed on page 74. The DAC received a digital signal from a control unit in the MCA and computer. This signal incremented the channel in which data was being accumulated by one channel, thereby increasing the voltage on the analyzer sectors by some preset increment. This channel advance signal came from a pulse sent by the timer/scaler after a preset number of pulses had been received from the current digitizer. The channel advance continued until the entire spectrum was scanned. Since the time spent in each channel was determined by the charge collected in the Faraday cup, small variations in ion beam current were automatically accounted for and spectra could be normalized to one another easily by knowing the total charge collected in the Faraday cup for the scan. Since charge exchange cross section sections are relatively small, the difference in the ion beam mean charge before and after the gas cell was considered to be negligible.

This technique for determining data acquisition time also simplified the conversion of the data to cross section estimates, since the cross section is directly related to the number of ECC electrons produced for each projectile ion passing through the oven.

The continuum electrons captured by the incident ion beam from the target gas were deflected by the radial electric field produced by the voltages applied to the sectors of the electron spectrometer. For a given voltage on the analyzer sectors, only electrons of a specific kinetic energy (see page 68) could be transmitted through the 160^{o} analyzer into the electron CEM. A conducting box surrounding the CEM was electrically connected to the cone of the CEM. Both were then biased negatively with respect to ground (-300 V) by another bias power supply. This negative biasing was used mainly to reduce backgrounds due to photoelectrons produced by photons from the hot oven (see Chapter IV, page 104). The signal from the CEM was further amplified, inverted and sent to the single channel analyzer (SCA) at which time the small amplitude noise pulses were discriminated from the larger amplitude real pulses. The output pulse from the SCA was a square wave positive pulse of constant amplitude which went directly into the multichannel analyzer (MCA). Each pulse was counted as an electron in the channel gated open at the time of arrival of the signal. When stepping to the next channel the gate to electron counts was closed until the analyzer sector voltage had been changed. An entire ECC spectrum was obtained by scanning the analyzer voltage over the full range of voltages as determined by the analyzer starting voltage, the voltage increment per channel, and the number of channels per scan. The scan could be repeated several times in order to build up counting

counting statistics, and as long as the total charge collected in the Faraday cup was known, spectra with a different number of scans could be normalized to one another.

Each time a spectrum was obtained with gas in the oven, it was necessary to run a background scan afterward. This background scan consisted of scanning the same energy range as the previous ECC spectrum but instead of flowing the gas through the oven, the same flow rate of gas was introduced directly into the oven vacuum chamber. This procedure, in effect, counted all those electrons produced outside of the gas cell which could possibly reach the electron CEM at the exit of the spectrometer. This spectrum was subtracted from the ECC spectrum to give a resulting spectrum which was assumed to be due solely to interactions inside the gas cell. This final background subtracted spectrum was used for cross section determinations. This background correction does have one experimental shortcoming: it does not account for ECC electrons produced in the plumes of gas outstreaming from the beam passage holes in the oven. These plumes increase the effective target length of the gas region. It was found that the effect of this increased target length was ∿10% (see Chapter V, page 137). Corrections were made for this effect when determining actual cross sections.

ECC Background Noise

Because of the low electron count rates expected when using H_2 and H in the gas cell, certain precautions had to be taken to insure a satisfactory signal to noise ratio. Since the electrons to be studied had velocities approximately equal to the incident ion velocity and, consequently, fairly high laboratory energy (∿544 eV) low energy

background electrons would not appear in the relatively small energy width spectrum scanned by the spectrometer. However, since the ECC process can occur with solid as well as gaseous targets, care had to be taken to prevent the ion beam from scraping any surfaces immediately preceding the spectrometer entrance. The ECC spectra obtained from solid targets, although not exactly the same shape as those from gaseous targets,[14] would nevertheless exhibit the same cusp structure and the peak of the cusp would appear at the same electron energy. The resulting background of electrons would have a count rate which could easily be many times that due to the H or H_2 target. Also, any small changes in the ion beam steering would change the count rates in an unpredictable manner. Referring back to Figure 6 on page 42, it is seen that there are four possible places that can act as sources of solid targets which could produce background ECC electrons: 1) The first collimator system, 2) the second collimator system, immediately in front of the oven, 3) the oven itself and, 4) the photon limiters. It was assumed that by choosing the sizes of the apertures in the two collimators, the beam could be made physically small enough to prevent it from hitting either the oven or the photon limiters. The ion beam diameter at the position of the photon limiters with aperture diameters of 1 mm and 0.33 mm at C1 and C2, respectively, of Figure 6 on page 42 was calculated from geometry to be $\sim$0.9 mm. This was less than the 1.67 mm diameter of the photon limiters. In actual practice, the beam diameter was probably smaller sine the geometric calculation is a "worst case" estimate which neglects effects of beam focusing, etc. Therefore, the background originating from both the oven and photon limiters could be eliminated relatively easily by sufficient collimation of the beam. However, during the collimation, the beam

necessarily struck the collimators. Therefore, preventing background electrons from originating at the oven and photon limiters produced another electron background. Since the beam struck both collimating apertures as it passed through, each collimating system contributed to the electron background. However, electrons produced at the first collimating system (C1 in Figure 6, page 42) were required to pass through the second collimator (C2 in Figure 6, page 42) before entering the electron spectrometer. By suppressing all electrons emanating from the second collimator, the background electrons originating from both of these collimators could be eliminated simultaneously. This was accomplished with a pair of parallel steering plates (D in Figure 6, page 42), each lying in a vertical plane parallel to the beam direction. The plates were attached to the oven collimator system (C2 in Figure 6, page 42) immediately downstream from the aperture. One plate was held at ground potential while the other was maintained at some positive voltage. The resulting electric field of $\sim$750 V/cm deflected the electrons produced at the collimators away from the oven while permitting the ion beam to continue with negligible deflection. Using the combination of beam collimation and deflection plates, the electron background count rate could be reduced to $\sim$0.05 sec^{-1} with the electron spectrometer set to transmit electrons with energies corresponding to the position of the peak of the cusp, i.e., the point in the ECC spectrum where the count rate would be greatest.

A test was performed to determine the ECC count rate to be expected from atomic hydrogen. The could rate obtained when using H_2 as a target was assumed to be approximately twice the rate for H, provided the target density and ion beam current were held constant. This rough

estimate determined that a count rate of $<\frac{1}{2}$ sec^{-1} for an atomic hydrogen target could be expected, assuming an ion beam current of $\sim$100 pA. This results in a signal to noise ratio of >10 when considering only the background due to the collimators noted in the previous paragraph. A more significant background was present when the oven was hot, and this is discussed in Chapter V.

Gas Handling System

The gas flow rate into the oven had to be accurately and precisely controlled in order to obtain accurate dissociation fractions. A gas handling system was therefore designed that was flow regulated rather than pressure regulated since thermal transpiration of the gas inside a hot oven would preclude using a pressure regulated delivery system. The fact that both argon and molecular hydrogen were to be used added two other constraints on the system. The first of the constraints was that the system had to be easily pumped out, and secondly, upon pumping, the quickly attainable base pressure in the system had to be $\sim 1 \times 10^{-6}$ Torr. Both of these two conditions were met by constructing the system from the largest possible diameter tubing and minimizing the total length of the tubing used in the system. The low base pressure requirement was necessary for the following reason. When determining the dissociation fraction, both argon and H_2 gases were required since the double capture method employed for the dissociation fraction used a comparison of the double electron capture signals from both argon and H_2. The cross section ratios (and therefore the signal ratios) of this process for Ar to H_2 are large. Since argon is a relatively heavy gas, small impurities from either the gas handling system or

from the main vacuum chamber would cause little error in the double capture signal. However, because of the much smaller cross section for H_2, any small impurity could greatly affect the double capture signal. If, for example, a small amount of argon were present in the gas handling system and flowed into the oven with the H_2, the double capture signal would be much larger than it should be. In anticipation of this possible problem, the gas handling system was designed so that low base pressures could be quickly and easily attainable.

The entire gas handling system is depicted in Figure 8 and was constructed from standard Mini-Conflat^R tees, nipples, crosses and bellows, and all valves had Mini-Conflat^R flanges on both end connections. Valves (2) through (5), (8) and (11) through (13) in Figure 8 were stainless steel bellows sealed valves. All tubing was type 303 or 304 stainless steel; in fact, the only non-stainless steel surfaces in the system were the palladium leak and the copper gaskets. The vacuum line from the forepump was, of course, trapped in order to prevent oil contamination. Hard vacuum pumping was done through the connections into the oven and the one into the oven chamber as well as through one line which led to another chamber upstream of the oven chamber. Since all valves, tubing, etc. were standard lengths, the system could be changed into another configuration fairly rapdily. This allowed testing of several prototype systems before the final design was decided upon, and this final design used basically the same parts as the first prototype - just in different places.
The gas flow into the oven was regulated by a Granville-Phillips motorized leak valve (9). This valve was controlled by a MKS Baratron capacitance manometer (10) which measured the difference in the pressure on each side of an aperture through which the gas flowed. The capacitance

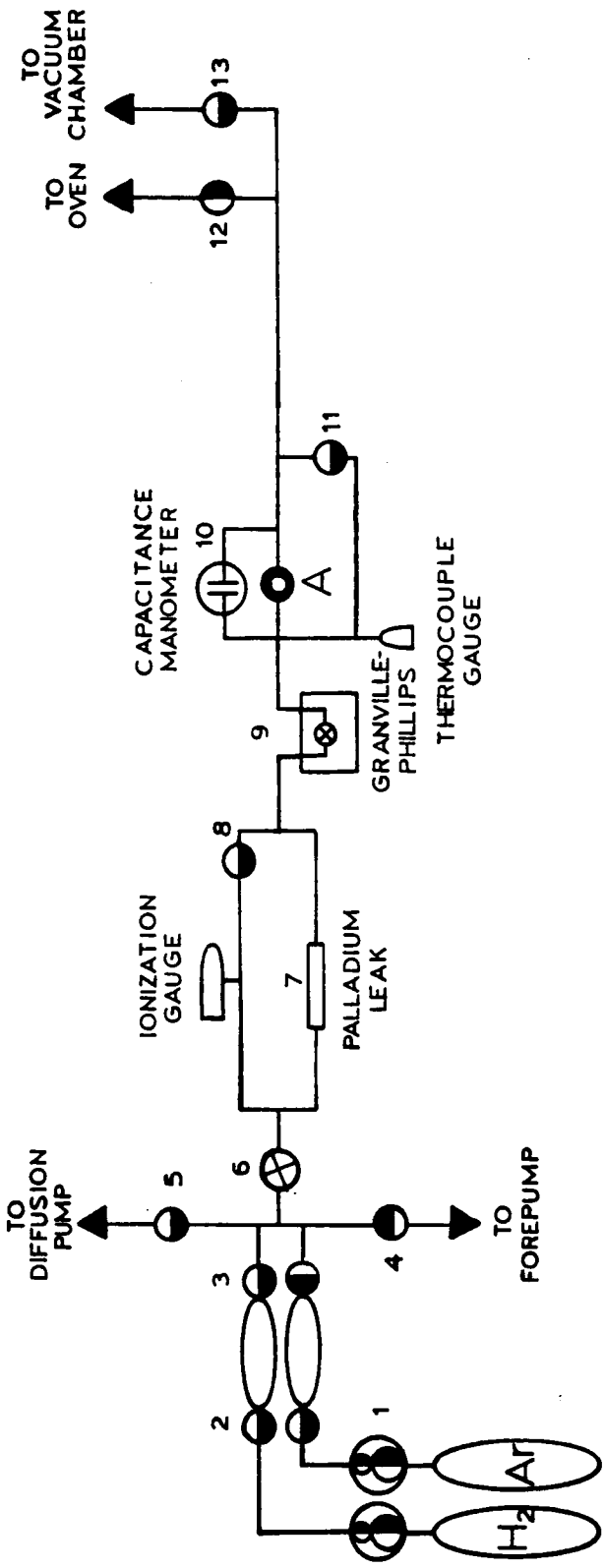

Figure 8. Schematic Diagram of Gas Handling System.

Capacitance manometer measures gas flow through aperture A into oven.

manometer was set to a desired pressure difference between the two sides of the flow aperture and this setting provided the means by which the flow through the Granville-Phillips leak valve was regulated.

Gas flow into the system was initially regulated by a two-stage stainless steel regulator (1) in Figure 8. The gas next entered a small buffer reservoir. These reservoirs could, if necessary, be isolated from the system with the valves (2) and (3). In practice, however, the valves on either side of these small reservoirs were left open and the gas flow into the system was regulated by the second stage of the regulator (1). The gas then flowed through the manual leak valve (5) which served as another buffer in the system. It was found that the Granville-Phillips valve could easily control $\sim$1 atm on the high pressure side with no noticeable loss or difficulty in maintenance of the flow. The manual leak valve was opened approximately halfway during the experiment. Two isolation valves, (4) and (5), immediately before the manual leak valve, provided connection to both the forepumps and a diffusion pump. Immediately after the manual leak valve, an ionization gauge tube was inserted in order to determine when the system had reached its base pressure. Opposite to this gauge was a palladium leak valve (7), which was used to further purify the H_2 gas. When H_2 was in the system, valve (8) could be closed and the palladium leak valve opened; and when argon was present, valve (8) could be opened and the palladium leak valve closed. It was found that H_2 gas of 99.9995% purity was sufficient for these studies, so the palladium leak was rarely used. The gas then entered the Granville-Phillips valve (9). As previously noted, this valve, in conjunction with the capacitance manometer (10), controlled the flow of gas into the oven. Not only could the pressure

difference between the two sides of the flow aperture be observed but the pressure on the high pressure side of the aperture (A) could be observed directly using a thermocouple gauge. The thermocouple gauge was sufficiently accurate to serve the purpose of determining whether or not the pressure was too high for the condition of molecular flow to be valid, since this molecular flow condition was necessary in order that the flow equations assumed in the next section were valid. A bypass valve (11), was used to allow quicker pumping of the high pressure side of the aperture when the Granville-Phillips valve was closed. During normal operations, valve (11) remain closed. Valves (12) and (13) were the final valves isolating the gas system from the oven and its vacuum chamber. Gas flowed into the oven through valve (12) and into the vacuum chamber directly through valve (13). This "direct" path through valve (13) was used to allow background determination. Valve (12) was closed during this background determination. One particular advantage of the flow regulated system is that the chamber background pressure could be matched to exactly that when gas was flowing through the oven. This was possible since the gas flow through the aperture was independent of the path into the oven vacuum chamber.

Determining Oven Pressure for Non-Dissociating Gas

The flow regulated gas system has an additional advantage in that the actual cell pressure can be determined to a reasonable degree of accuracy simply by knowing the flow rate into the cell. The highly schematic depiction of the gas delivery system is shown in the following diagram. Gas flows from the reservoir at temperature T_R through the aperture of area A. The pressures, P_H and P_L, are the gas pressures on

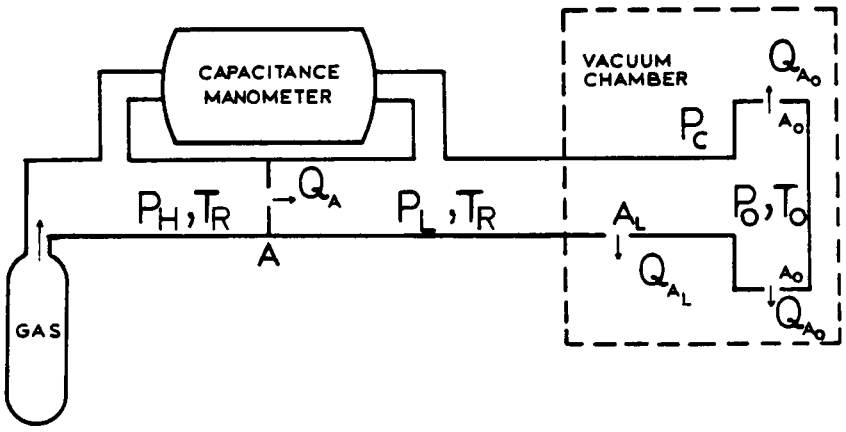

each side of the aperture. The capacitance manometer measures the quantity of $P_H - P_L$. For $P_H > P_L$ there is a net flow rate Q_A, through the aperture from left to right. Upon entering the vacuum chamber, the gas may follow one of two paths. It may flow into the oven and then out the chamber at a rate Q_{A_o}, through each of the oven apertures of area A_o, or it may flow into the chamber via small gaps in the gas feed tubes into the oven. This leak rate is depicted as Q_{A_L} where A_L is a representative "leak aperture" area. The chamber pressure is denoted as P_c and the pressure in the oven is P_o. The gas flow rate through different parts of the system must be conserved. So,

$$Q_A = Q_{A_o} + Q_{A_o} + Q_{A_L} \tag{55}$$

It was calculated from the dimensions of the oven parts that $Q_{A_L}/Q_{A_o} \leq 1 \times 10^{-4}$, so Q_{A_L} can be neglected in the following discussion. The flow is given by,

$$Q = \sqrt{\frac{kT}{2\pi m}}\,(P_i - P_f)A \text{ cgs units.} \tag{56}$$

Using equation (56) in (55) gives

$$\sqrt{\frac{kT_R}{2\pi m}}\,(P_H - P_L)A = \sqrt{\frac{kT_o}{2\pi m}}\,(P_o - P_c)(2A_o) \tag{57}$$

where k ≡ Boltzmann's constant, T ≡ absolute temperature of gas flowing through aperture, m ≡ mass of one molecule of gas flowing through the aperture of area A cm^2 and $P_{i,f}$ ≡ pressure on either side of the aperture. Since $P_c/P_o \lesssim 10^{-3}$, then P_c can be neglected. Rearranging (57) and defining $\Delta P_B \equiv (P_H - P_L)$

$$P_o = 0.6711 \sqrt{\frac{T_R}{T_o}}\,\Delta P_B\,\frac{A}{A_o} \text{ mTorr.} \tag{58}$$

For $T_R = T_o$ and using $A_o = 1.29$ mm^2 and $A = 0.785$ mm^2

$$P_o = 0.408 \Delta P_B \text{ mTorr.} \tag{59}$$

Equation (58) and (59) are valid providing certain conditions are met: 1) molecular flow conditions hold; 2) all leaks are negligible; and 3) the mass of a molecule of gas in the reservoir is the same as the mass of a molecule of gas in the oven. This third condition may seem rather obvious but if the oven is hot enough for dissociation of a molecule to take place, this requirement does not necessarily hold. However, the corresponding relation giving the pressure in the oven for the case of dissociating molecules can still be derived and will be shown in Chapter IV. Note that equation (58) and (59) will hold exactly even for a hot oven when a nondissociating gas such as argon is used. The molecular flow condition

can be considered valid if[47]

$$PD < 15 \text{ mTorr-cm} \tag{60}$$

where P ≡ pressure in mTorr and D ≡ diameter of aperture in cm. Using the Maxwellian distribution of velocities, it can be shown that the mean free paths λ_i, for Ar and H_2 are given by,[47]

$$\lambda_{H_2} = 3.085\text{x}10^{-2}\,\frac{T}{P} \text{ cm and } \lambda_{Ar} = 1.74\text{x}10^{-2}\,\frac{T}{P} \text{ cm}, \tag{61}$$

where P ≡ mTorr and T ≡ absolute temperature. Using (61) and (60) it is found that the pressure P must be low enough so that

$$\lambda_{H_2} > 2.07\text{x}10^{-3}\,DT \text{ cm}, \tag{62}$$

$$\lambda_{Ar} > 1.16\text{x}10^{-3}\,DT \text{ cm}. \tag{63}$$

In order to apply the preceding equations for the pressure in the oven, it is found using (62) and (63) that the absolute pressure in the immediate vicinity of the gas flow aperture must be less than ∿150 mTorr. If the dimensions of the tube adjoining either side of the flow aperture are taken into account, the resulting pressure requirement turns out to be somewhat lower (∿10 mTorr). In practice, it was noted that even with 200 mTorr on the high pressure side of the aperture, the pressure in the oven calculated for (59) agreed to within 10% with the pressure determined by the direct experimental means (see page 136).

Impurities in Gas Cell

As mentioned previously, it was critical that when the H_2 gas flowed into the oven, no significant impurities would be introduced

along with it. If the number density of the H was not very large compared to the number density of the impurities in the oven, then the ECC signal to noise ratio could possibly be less than 1. It would then be very difficult to extract the signal due to H alone. It was therefore necessary to determine the existence and quantity of any impurity introduced by flowing H_2 into the oven. The RGA mentioned previously has an electric quadrupole mass filter which selects ions of different mass which have been ionized by an internal electron gun. These ions can be collected as current in a Faraday cup or counted individually on a CEM. As the field of the quadrupole is scanned upward, peaks will appear on an oscilloscope trace corresponding to the different masses allowed through the filter. Although the CEM is much more sensitive than the Faraday cup for counting ions it is necessary to use both in order to get a good estimate for the partial pressure of a particular ionic species. Figure 9 shows the change in the relative partial pressures of H_2 and the significant impurities in the vacuum system as a function of increasing H_2 gas flow into the oven. As seen from the figure, the amount of impurity as introduced by the gas handling system is negligible. The impurities shown in the figure are usually present in most vacuum systems. Table I compares the partial pressures for the cold versus hot oven as determined by the RGA. As seen from the table, there is an increase in partial pressures of all species due to heating of the oven, but none of the impurity pressures increase significantly. This fact is especially satisfying for the materials Mo, Ta, and W since these materials are used for construction of the radiation shielding and the oven itself. At the operating temperature shown there seems to be no problem due to evaporation of the oven parts

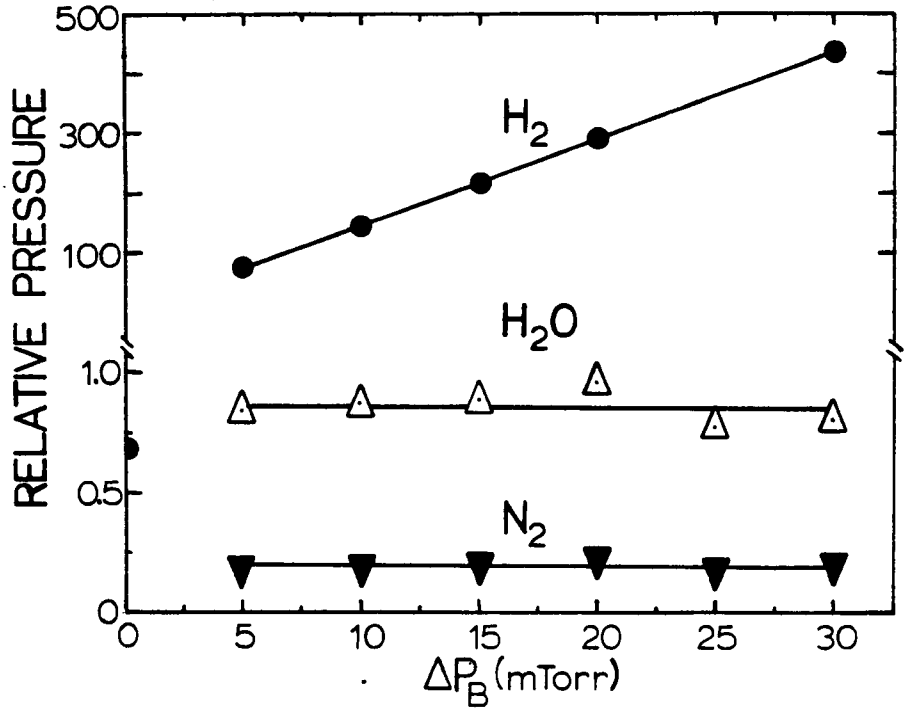

Figure 9. Impurities Flowing Into Oven From Gas Handling System.

N_2 and H_2O are residual impurities normally found in vacuum systems.

either concerning deterioration of the parts or the interaction of the consequent impurity species with the ion beam.

Magnetic Field Nulling

Since the electrons to be studied had laboratory kinetic energy of ∿544 eV, even small magnetic fields could have a noticeable effect on the trajectories of these electrons. The components of the magnetic field in the H-oven chamber will be designated B_{Hor}, B_{11}, and B_{vert}. B_{vert} denotes the vertical component, B_{11} denotes the horizontal component which is parallel to the beam direction and B_{Hor} denotes the

TABLE I

IMPURITIES IN OVEN VACUUM CHAMBER

Species	Partial Pressure (Torr) T=293K	Partial Pressure (Torr) T=2340K
H_2^*	1.39×10^{-5}	1.5×10^{-6}
C	5.6×10^{-10}	1.7×10^{-9}
CH	5×10^{-10}	7.7×10^{-10}
N, CH_2	5×10^{-10}	5.9×10^{-10}
NH	4×10^{-10}	1.8×10^{-0}
O, CH_4	1×10^{-9}	6×10^{-9}
OH	1×10^{-9}	1×10^{-8}
H_2O	9×10^{-9}	4×10^{-9}
N_2	4×10^{-9}	1.5×10^{-9}
O_2	0	1×10^{-10}
CO_2	0	5×10^{-9}
M_o	0	5×10^{-10}
T_a	1×10^{-10}	6×10^{-10}
W	2×10^{-10}	9×10^{-10}

*H_2 gas was being flowed into the oven for these measurements but the flow rates for hot and cold oven measurements were not the same.

horizontal component normal to the beam direction. The region inside the oven vacuum chamber in which the oven and electron spectrometer were located had the approximate shape of a cube with sides ∿20 cm in length. The average values of the magnitudes of B_{vert}, B_{11}, and B_{Hor} throughout this cubical volume were 290 mG, 103 mG, and 123 mG, respectively. The electron spectrometer was positioned so that the trajectories of the electrons being analyzed were in the horizontal plane containing B_{Hor} and B_{11} as shown in the following diagram. The deflection d, of a particle of mass m (amu), charge q (electron charge), kinetic energy E_k(keV), after traveling a distance of X cm in a uniform magnetic field of B (Gauss) can be shown to be

$$d = \frac{4.552\times10^{3}}{qB}\ mE_k - \sqrt{\frac{2.072\times10^{6}}{q^2B^2}\ (mE_k) - X^2}\ . \qquad (64)$$

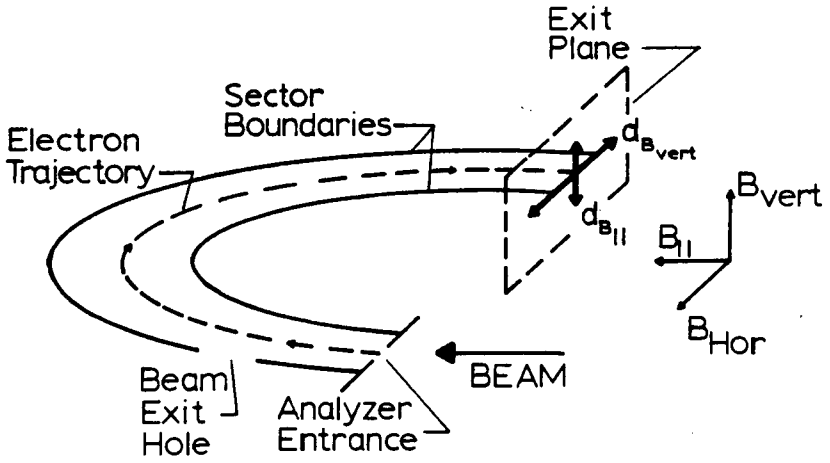

Note that X is the distance traveled from the point of entry into the magnetic field as measured along the initial direction of motion of the particle.

The magnetic field component having the most noticeable effect on the electron trajectories was B_{vert} since the electron velocities were always perpendicular to this field component. Assuming a path length of $\sim$12 cm through the spectrometer (a complete description of the electron spectrometer begins on page 68) the deflection of an electron due to B_{vert} is calculated from equation (64) as $\sim$2.7 mm. This deflection is greater than the diameter of the energy resolving aperture (1.9 mm) and had the effect of changing the analyzer constant. The spectrometer uses a radial electric field to allow transmission of electrons with a specific energy E_e, for a given potential difference between the sectors V_s. The relationship between E_e and V_s is such that $V_s=kE_e$, where k $\equiv$ analyzer constant. For a given energy E_e, if a magnetic field alters the radius of curvature of the essentially circular electron trajectories, the analyzer constant would appear to change also, since a change in V_s would be required to maintain the transmission of electrons. As long as the effects of the magnetic field are constant and not too drastic, the deviations in the analyzer constant from the theoretical value should not affect the ECC results.

Of the two remaining components of the magnetic field, B_{Hor} and B_{11}, only B_{11} had a significant effect on the electron paths through the spectrometer. A deflection of $\sim$0.6 mm (for X=10 cm) caused by B_{11}, while much less than the deflection caused by B_{vert}, nevertheless could still noticeably affect the number of electrons being transmitted through the

spectrometer. There are two methods by which the effects of magnetic fields in the region of the spectrometer could have been eliminated: 1) enclosing the region in a high permeability metal shield or 2) externally compensating for each component of the magnetic field. The former of these two methods was practically impossible because of space limitations. The latter method was therefore chosen. For this purpose a cubical magnetic field coil arrangement was designed to separately null each component of the magnetic field in the vicinity of the oven chamber. This cubical coil arrangement was centered about the center of the oven vacuum chamber. By separately nulling each component of the field and repeating the process until minimum fields were established it was found that all components of the magnetic field inside the oven chamber could be reduced to less than 20 mG.

Although, in principle, complete nulling of the magnetic field inside the oven chamber would be desirable, in actual practice this was not the optimum condition for maximum transmission of electrons through the spectrometer. When aligning the spectrometer with the ion beam path an optical telescope was used to visually set the position of the spectrometer. The 1.67 mm diameter photon limiters could be used in conjunction with the 3.2 mm diameter beam exit hole in the rear sector of the spectrometer to align the axis of the spectrometer with the optical axis of the telescope. It was assumed that the ion beam would travel along the optical axis of the telescope. The beam exit hole was centered in the crosshairs of the telescope by adjusting the position of the spectrometer. The photon limiters were then inserted in place and centered in the crosshairs. By iterating between the positioning of these two points the spectrometer axis (i.e., the line joining the center of the photon

limiters and the beam exit hole) could be aligned closely with the optical axis of the telescope, but perfect placement of the spectrometer axis was impossible. If it is assumed that at least one of the two aforementioned apertures could be positioned with its center along the optical axis of the telescope, two possible errors in the positioning of the spectrometer could result: 1) rotation of the spectrometer axis in a horizontal plane about the point at which the correctly placed aperture is located and 2) rotation of the spectrometer axis in a vertical plane parallel to the optical axis about the aperture position. The first of these positioning errors effectively changes the analyzer constant and is analogous to changing B_{vert}. The second corresponds to a change in the magnitude of B_{11} required for maximum transmission through the spectrometer. Although there was no way to visually ascertain that the alignment was perfect, a method was devised by which any small errors in alignment could be compensated for with the magnetic field coils. By first setting the currents in the coils so that the magnetic field was brought to its minimum value, some gas (either H_2 or Ar) was admitted to the oven. The voltage on the analyzer sectors was adjusted so that electrons with energy corresponding to the peak of the cusp should be transmitted through the spectrometer. Then by changing the magnetic field components slightly, the maximum transmission was obtained. It was found that, in optimizing the transmission through the spectrometer, B_{vert} and B_{Hor} were changed negligibly from the null values However, B_{11} was brought to the value corresponding to the initial value before nulling; i.e., it was necessary to turn off the nulling field. This indicated that the electron trajectories were being deflected

$\sim$1.4 mm out of the horizontal plane containing the centers of the entrance aperture, exit aperture, and beam exit hole. This corresponded to an angular deflection of $\sim 1^{o}$.

Electron Spectrometer

The electron spectrometer used to analyze the energies of ECC electrons was a 160° spherical sector electrostatic analyzer of the type first introduced by Purcell.[48] The plane of the analyzer is defined as being the plane containing the central ray through the analyzer, while the perpendicular plane denotes the plane perpendicular to the analyzer plane and parallel to the initial beam direction. The analyzer accepts a generally diverging beam of electrons with angular divergences α and β in the plane of the analyzer and in the perpendicular plane, respectively. This is shown in the following diagram. It can be

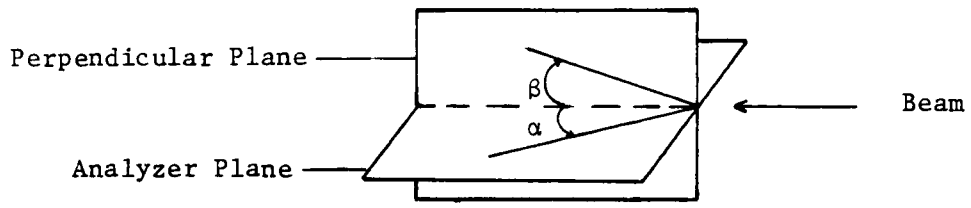

shown that the focusing condition for the analyzer is such that the sectors subtend an angle of 180°.[1] The basic equation obtained from applying the focusing condition and a second order approximation is found to contain one term with α^2 but has no β dependence. Such an analyzer is said to have first order focusing in the analyzer plane and perfect focusing in the perpendicular plane.

The electron CEM was positioned at the exit of the spectrometer as shown in Figure 10. Although the analyzer is strictly only doubly focusing when the angle subtended by the sectors in 180^{o}, the sectors in the analyzer used in this study subtended an angle of 160^{o}. This allowed for easier external placement of the electron CEM and also moved the entrance focal point a distance of $\sim$1.9 cm away from the boundaries of the sectors. The beam exit side of the oven could then be placed at the approximate position of the focal point. The outer sector was held at negative potential while the inner was biased positively as shown in Figure 10. The potential of the central ray through the analyzer was maintained at ground potential by the voltage divider comprised of resistors R_a and R_b. The electrically isolated copper sectors were held at the correct relative positions with two stainless steel side plates and the exposed parts of the sectors were then covered with 0.013 cm thick tantalum to prevent stray electrons from the oven heating electron gun (see page 101) from entering the region between the sectors.

The electron CEM was enclosed by an aluminum box which was electrically connected to the cone of the CEM and both were biased to -300 V. The back of the CEM was biased to +3700 V. The negative bias on the CEM cone and shielding box served a two-fold purpose. First, the negative bias on the box prevented any low energy electrons inside the oven vacuum chamber from reaching the CEM while also acting as a shield against stray electric fields. Secondly, since the CEM and the box were electrically in common, there was no electric field between the two. Consequently, the hole in the box did not have a focusing effect on the electrons exiting the spectrometer. This absence of a field

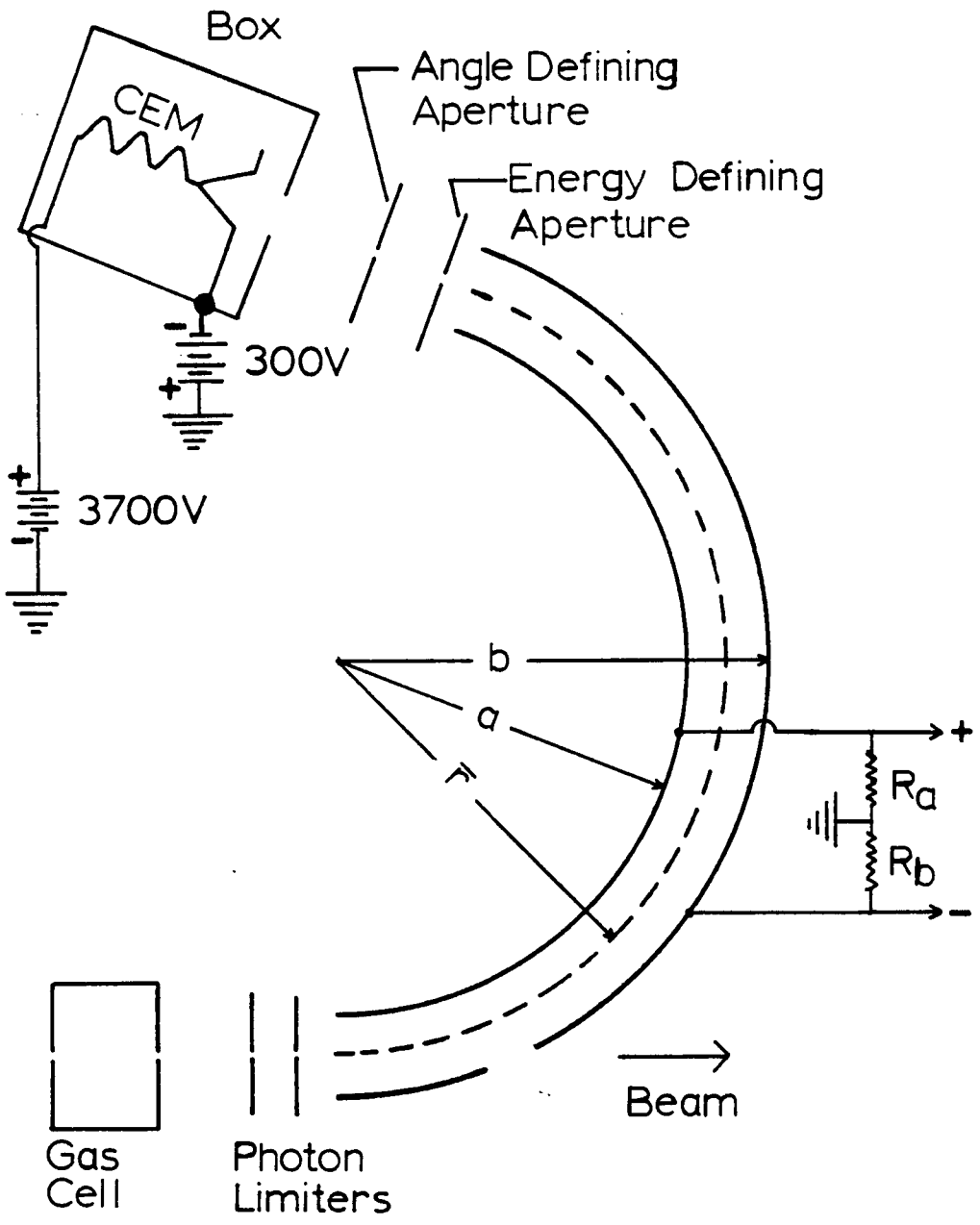

Figure 10. Electron Analyzing Apparatus.

ECC electrons produced in the oven (gas cell) were energy analyzed by the spherical sector electrostatic analyzer. The forward cone of electron accepted was limited by the angle defining aperture while the energy defining aperture set the energy resolution of the apparatus. See Table II, page 77 for definitions of a, b, $\bar{r}$, R_a, R_b, and aperture sizes.

combined with the applied -300 V bias was critical in reducing the electron background when the oven was hot (see page 106).

It was necessary that the spectrometer-CEM system be calibrated. In principle, it was required that an extended source of electrons, with energy and spatial distributions approaching that of the ECC spectrum, be used to calibrate the electron analyzing system. However, there was no way to produce an electron source with the correct energy and spatial distributions, so a compromise technique was used. An electron gun produced a beam of electrons of known energy with a beam size approximately the same as the ion beam at the analyzer entrance. This electron gun was attached directly to the front of the analyzer entrance. The emitting filament was heated by a 6 volt power supply and was biased at a high negative voltage to produce a high energy electron beam. The electron emission was controlled by raising or lowering the filament voltage with the Variac in Figure 11.

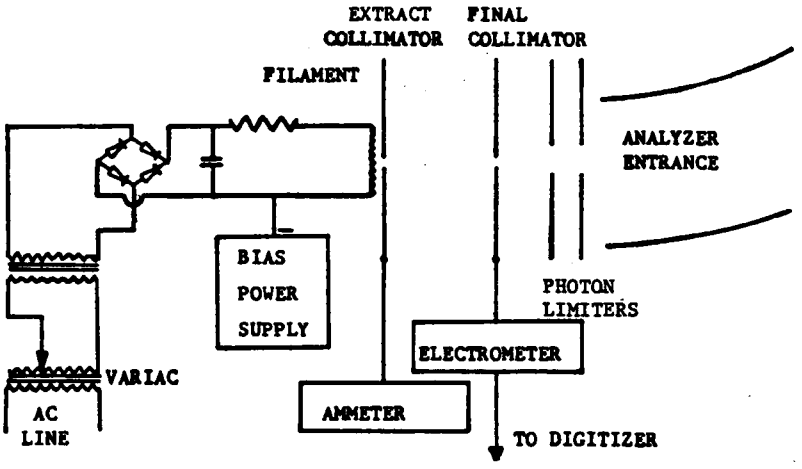

Figure 11. Spectrometer Calibration Electron Gun Electrical Schematic.

The spectrometer voltage was scanned over the voltage corresponding to the energy of the electrons being emitted and a spectrum was obtained. The acquisition time in each channel was controlled by the current collected on the final collimator. Several such transmission spectra were obtained over a relatively wide range of electron energies and most spectra exhibited an approximately triangular form as shown in Figure 12. Figure 13 shows a plot of the full width at half maximum (FWHM) of the electron transmission functions versus the analyzer voltage. The energy resolution of the spectrometer is given by the slope of the straight line and was determined using a least squares fit to the data. This analyzer transmission function is shown superimposed on a typical cusp spectrum in Figure 14.

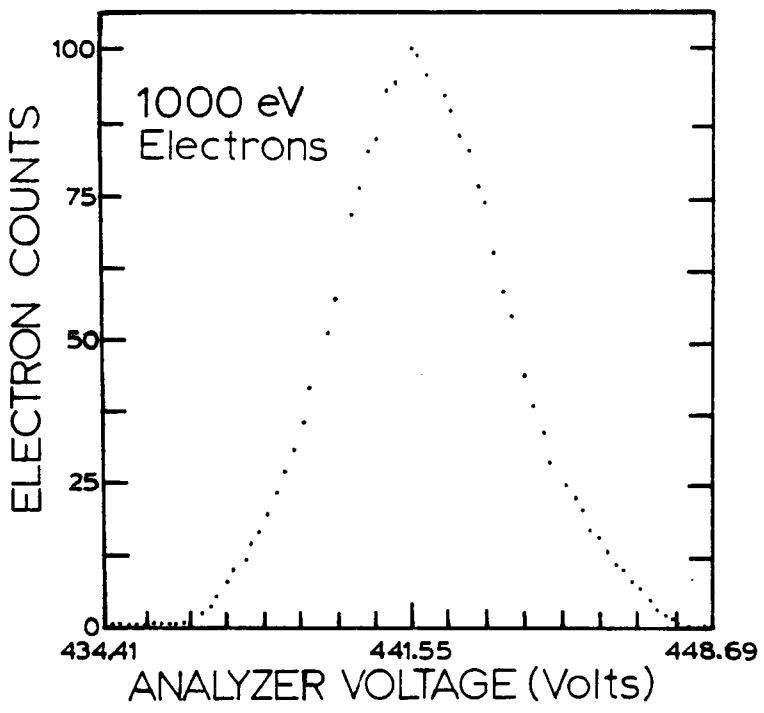

Figure 12. Analyzer Transmission of 1000 eV Electrons Produced by Electron Gun.

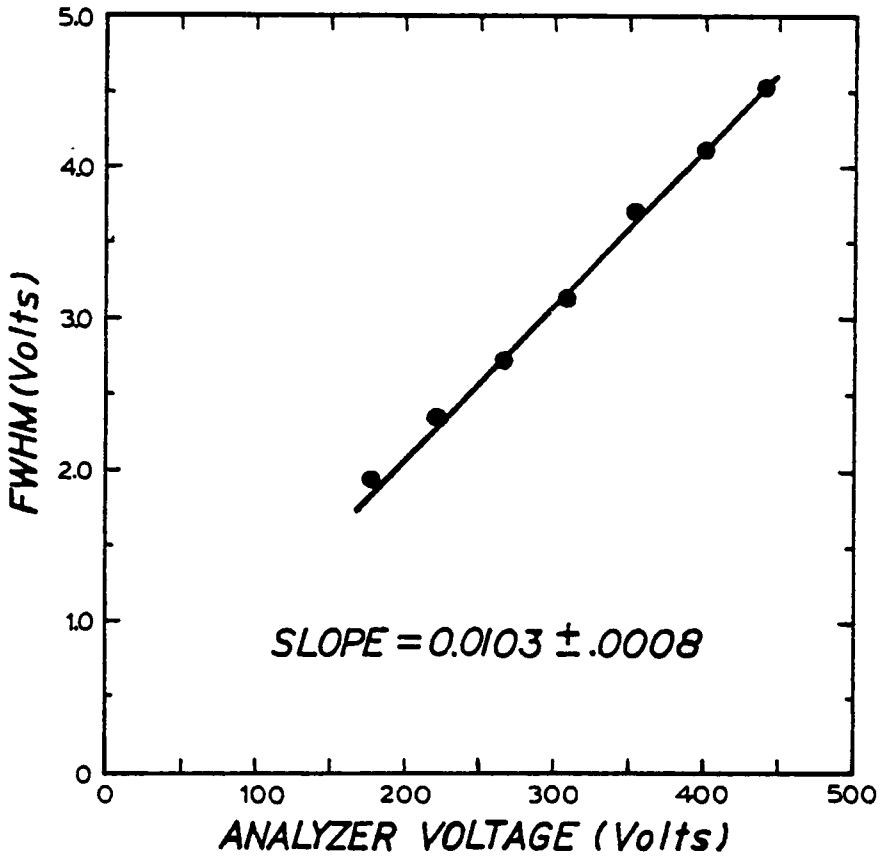

Figure 13. Analyzer Energy Resolution Calibration.

A plot of FWHM versus analyzer voltage at the peak of the transmission function for several electron energies.

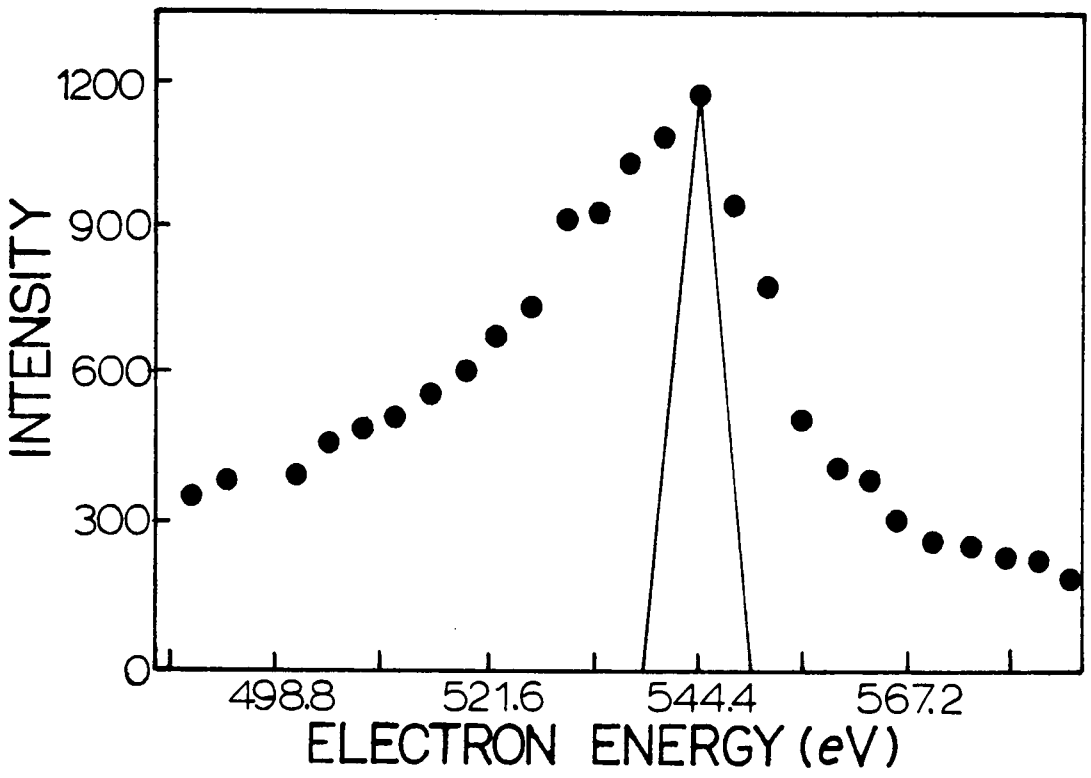

Figure 14. Analyzer Transmission Function Compared to Typical ECC Cusp. The ECC cusp is a result of 12 MeV C^{6+} incident on argon. The triangular transmission function of the analyzer is shown normalized to the cusp peak intensity and was calculated from the slope of the straight line in Figure 13.

The analyzer voltage at the peak positions of the transmission spectra varies linearly with the electron energy as shown in Figure 15. The slope of this line is defined as the analyzer constant k. It was assumed that the transmission efficiency of the spectrometer was 100% for the purposes of this study.[49] This assumption should be valid for the very small angles of entry into the

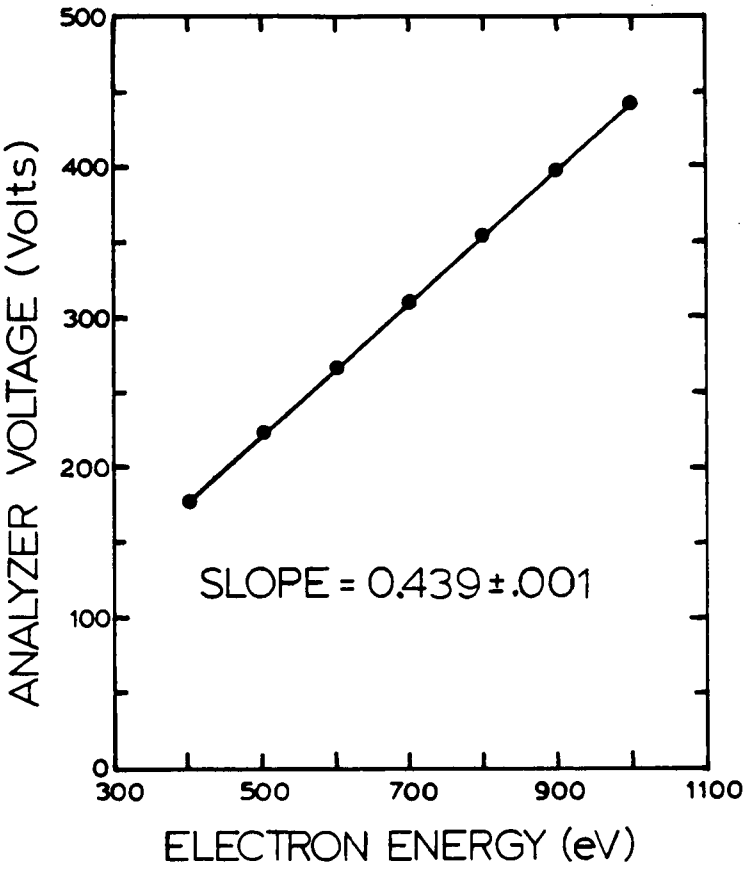

Figure 15. Analyzer Constant Calibration.

The analyzer voltage V, is related to the electron energy E, by the expression V = kE, where k is the analyzer constant and is the slope of the line shown in the figure.

spectrometer that were present in these measurements. The absolute detection efficiency of the electron CEM (muRata Ceratron EMS 1081 B) for 300 eV electrons is 70%±10%.[50] The electrons entering the CEM have energies within the range 180-400 eV after being slowed by the bias potential of -300 V. The detection efficiency of the CEM should be within the range of efficiencies noted for these energies. For the purpose of

cross section determinations, therefore, the number of counts in a spectrum was corrected by a multiplicative factor of 1.428.

Table II gives a summary of the operating parameters of the electron spectrometer. It should be noted that the expression for the theoretical energy resolution is approximate only. The expression used is strictly valid for rectangular entrance and exit slits, not circular apertures. The term $\frac{1}{4}W$, due to aberrations from the angular spread of the paths of the electrons, is included in the theoretical energy resolution.

The expression also assumes uniform and complete coverage of the entrance slit by the electron beam being analyzed, while in practice the electrons are contained within a narrow cone centered about the ion beam axis. This electron cone cannot diverge to a size appreciably larger than the ion beam before being separated from the ion beam by the electric field of the spectrometer. For this reason, the entrance aperture size was taken to be the same as the ion beam size for the purpose of this calculation; because of this, only the exit aperture radius enters into the formula for the theoretical energy resolution.

TABLE II

ELECTRON SPECTROMETER CALIBRATION PARAMETERS

Sector angle = 160°
Radius of outer sector ≡ b = 6.069 cm
Radius of inner sector ≡ a = 4.879 cm
Radius of central path = $\bar{r}$ = 5.474 cm
Dispersion ≡ D = $2\bar{r}$ = 10.95 cm
Angular acceptance ≡ θ_o = 2.0°
Resistor Divider R_b/R_a = 1.23
Theoretical Analyzer constant[1] ≡ k = Voltage/Energy = b/a - a/b = 0.440
Measured Analyzer constant k = 0.439±0.001 (see Figure 16)
Theoretical Energy Resolution (includes angular aberation term, ¼W)

$$\frac{\Delta E(FWHM)}{E} = \frac{W+\frac{1}{4}W}{D} = 1.08\%$$

Measured Energy Resolution = (1.03±0.08)% (see Figure 14)
Energy Resolving aperture ≡ W = 1.9 mm diameter (see Figure 10)
Angle Defining aperture = 1.0 mm diameter (see Figure 10)
Analyzer Transmission Efficiency = 100%[49]
Electron CEM Detection Efficiency at 300 eV = (70±10)%[50]

CHAPTER IV

THE ATOMIC HYDROGEN OVEN

Introduction

Perhaps the most efficient technique for producing a well-defined target region of high density and high purity atomic hydrogen for ion-atom collision experiments is by using a high temperature dissociation oven.[27-33,51] All furnaces used to produce static gaseous targets of atomic hydrogen by dissociation have been operated basically in the same way: A cylinder of tungsten with gas containment plugs in each end, which define an interaction region, is heated electrically by passing a large current at low voltage, either AC or DC, from one end to the other. Two beam passage holes allow an ion beam to pass through the interaction region normal to the cylinder axis. Molecular hydrogen is introduced into the interaction region through a gas inlet tube which can be inserted in a hole drilled radially at some point on the cylinder. Refinements such as radiation shields to minimize heat loss and baffles requiring the target gas to contact hot surfaces many times before entering the interaction region are also added to the basic design. The operating characteristics of these furnaces vary from one design to another depending on the amount of radiation shielding, target length, etc., and the operating characteristics of several widely used oven designs are summarized in Table III.

One disadvantage associated with the electrical resistance heating method is the production of relatively large magnetic fields associated with the large currents, typically 100-600 amps, required to heat the

TABLE III

OVEN CHARACTERISTICS

Reference	Oven Dimensions**	Operating Pressure	Temperature	Current (amps)	Voltage	Dissociation Fraction (%)
30	1.10x5 cm cylindrical	.03 mTorr	2500 K	600	8 VDC	96±4
33	0.635x1.27 cm cylindrical	1 mTorr	2400 K	325	2.75 VDC	88
62	0.64x4.19 cm cylindrical	1 mTorr	2700 K	100	3.3 VDC	
34	0.6x2.5 cm cylindrical		2350 K	130	10 VAC	92
31	cylindrical	1 mTorr	2373 K	144 rms		
35			3000 K	250		39
41	7.5x0.6 cm	1 mTorr	2200 K	70	4 VAC	80
Present Design	1.5x0.5 cm	>5 mTorr	>2400 K	0.250	6-8 KV	>90

*Calculated from the given values of $Y^*_{q,q-2}(H_2)/Y_{q,q-2}(H_2)$ and T^* and inserting into the general formula given by equation (B.13) of Appendix B.

**Diameter of cylinder is listed first.

furnace. These fields would not have any significant effect on ions passing through the oven. Charge exchange to and from bound state of projectile ions can therefore be studied with little regard for the magnetic fields. However, if one is attempting to study electrons ejected from ion-atom collisions, the magnetic fields would greatly disturb the paths of these electrons. The effect of these fields could be eliminated by gating the heating current off when counting, but this would greatly reduce both counting and heating efficiencies. However, if the oven could somehow be heated without producing the large magnetic fields, a 100% counting efficiency could be realized and, at the same time, no loss in heating would occur.

By assuming the simplistic model of a wire carrying current I, the magnetic fields associated with that current at a distance r, from the wire can easily be computed using the relation, $B(\text{gauss}) = 0.2\ I/r$. At a point 1 cm from the wire for I = 100 amps, B = 20 gauss (typical for resistance heating): for I = .250 amp, B = 50 milligauss ($\sim$0.10 x Earth's magnetic field).

Producing an oven design which could be heated to sufficient temperature throughout an acceptable region by electrical resistance heating using currents of 250 mA would be impractical. This small current would necessitate the use of either impractically thin walls on the cylinder to be heated or very high voltages. A solution to this dilemma can be found in the method of electron impact heating.

A beam of electrons produced by a special cathode was focused by an electrostatic lens system (see Appendix D) onto the outer wall of the gas containment region. The electrons are supplied $\sim$6 KeV of energy by the

lens system and it is the transfer of this energy upon impact with the wall that heats the oven. For example, in principle, a 200 mA beam of electrons with 6 KeV can produce up to 1200 watts of heating power assuming a 100% inelastic collision with the wall.

Besides the requirement of very low associated magnetic fields, several other factors relating to the exact design of the oven must be considered. 1) Since the oven will be very hot (∿2500 K), precautions must be taken in order to prevent harm to the vacuum chamber as well as any instrumentation in the chamber. For the present experiment, this "in vacuum" instrumentation consists of the channel electron multiplier (CEM) and the electron spectrometer. 2) In order to produce more efficient heating, shielding must be incorporated into the design which will minimize the heat loss by blackbody radiation. 3) Because the spectrometer must be placed reasonably close to the oven, the entire oven assembly must be compact. 4) All parts of the assembly must be durable. 5) The oven assembly must be easy to assemble and disassemble in order to minimize the time required to replace any parts. 6) The entire oven assembly must be moveable within the vacuum chamber in order to enable precise placement of the oven in front of the spectrometer in the path of the ion beam. 7) Finally, since the oven is being heated by an electron beam, measures must be taken to prevent any of the heating electrons from entering the electron spectrometer, thereby causing a potentially large background.

Construction and Design of the Oven

The oven, shown in Figure 16, consists of several components machined from tungsten. The interaction region is a cylindrical hole of 4.10 mm diameter. The one-piece main body of the oven consists of three

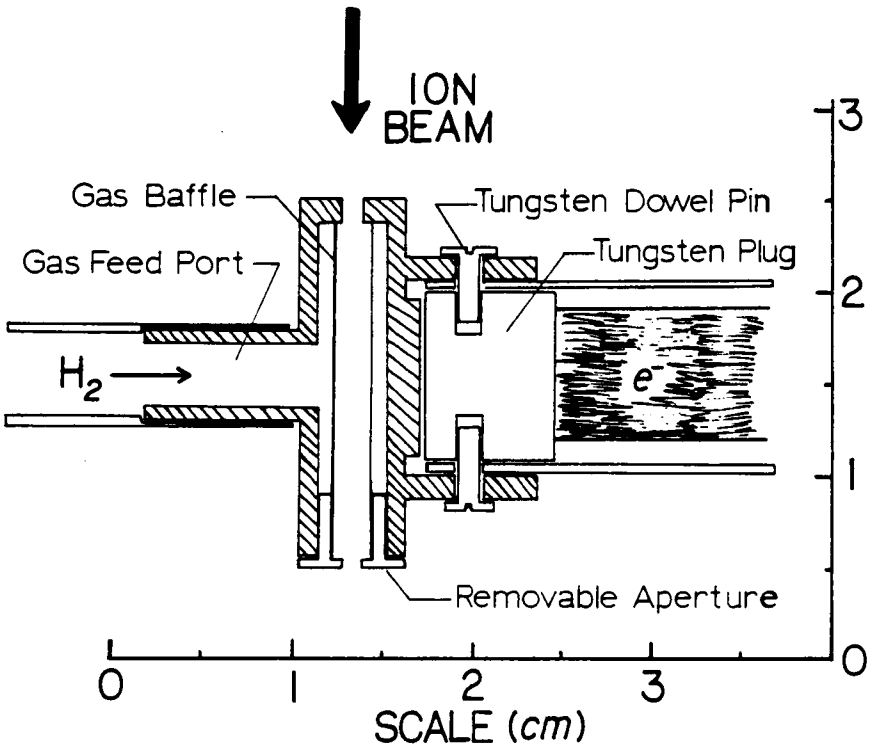

Figure 16. Close-up View of Atomic Hydrogen Oven.

Electron beam entering from right heats tungsten plug by electron impact which then transfers heat to the rest of the oven.

cylindrically symmetric regions with a common axis: 1) gasport, 2) main cell, and 3) plug securing port. The H_2 gas enters the oven through the gas port at the left of Figure 16. The main cell is at the center of the figure and can be best described as a thick disc. The interaction region is a cylindrical hole whose axis is perpendicular to that of the main cell. This hole does not extend completely through the main cell. A 4.1 mm hole begins at one side and stops 1.3 mm short of the other side. A 1.3 mm diameter hole extends through the remaining distance. This 1.3 mm hole is one of the defining apertures of the interaction region. The other 1.3 mm aperture is contained in a removeable plug which fits inside the 4.1 mm central hole. When this plug is inserted, a well-defined interaction region is formed. Its dimensions are 4.1 mm diameter by 15 mm long. The collimated ion beam can easily pass through the apertures and region without hitting any surface. Since the probability of an H_2 molecule dissociating is directly proportional to the number of times that molecule comes in contact with the hot tungsten surface, then in order to increase the probability that the ion beam will only "see" H atoms when passing through the interaction region the H_2 molecules must be forced to undergo many collisions with the hot surface before being allowed into the interaction region. This is accomplished by rolling a small sheet of .025 mm thick tungsten into a "semiclosed" cylindrical tube, a cross-section of which approximates a spiral as shown in the following highly schematic diagram. This tube is then inserted into the end of the gas containment aperture before it is inserted into the main body of the cell thereby forming a baffle which forces the entering H_2 molecules to

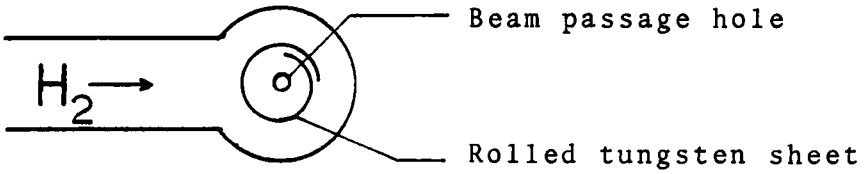

follow a long, tortuous path requiring many changes of direction and, therefore, many bounces off the walls to get into the interaction region. The equilibrium dissociation fraction is improved in the region through which the ion beam passes as a result of the increased surface area interacting with the H_2. The third portion of the oven is the plug securing port. The tungsten plug to which the electron beam imparts the energy to the heat oven fits inside this end of the oven. The "electron" tube, formed from .025 mm tungsten sheet, fits over the tungsten plug and inside the securing port of the oven. This tube not only provides essential support for the oven, but also contains the oven heating electrons in the immediate vicinity of the tungsten plug. The plug must be well secured to the oven since, in normal operation, the oven is supported vertically in the vacuum chamber.

The entire oven assembly is shown in Figure 17. The main oven assembly has cylindrical symmetry, and traveling in a direction radially outward from the axis of symmetry three radiation shields are encountered. These shields are .025 mm tungsten (F), 0.127 mm tantalum (E), and 1.6 mm molybdenum (C), respectively. The tungsten and tantalum shields are sheets which have been rolled into tubes, whereas the outer molybdenum shield is a seamless tube. The two inner shields are bounded on one end by a molybdenum plug (D) and on the other by a tantalum cap (L) which also

Figure 17. Atomic Hydrogen Oven Assembly.

A - Stainless steel oven support

B - Copper water jacket

C - Molybdenum outer radiation shield which screws onto A

D - Radiation shield support (molybdenum)

E - Radiation shield (tantalum)

F - Inner radiation shield (tungsten)

G - Gas feed tube (tungsten)

H - H-oven (tungsten)

I - Tungsten tube (requires that incoming molecules scatter from walls several times before entering interaction region)

J - Replaceable tungsten plug onto which electron beam is focused to heat oven

K - Rolled tungsten sheet (0.025 mm) forming tube which serves as a support for oven and also positions the plug end of the oven at focus of electron beam

L - Tantalum anode lens element which also serves as supporting end for radiation shields and oven

M - Tantalum electron baffle

N - Copper electron shield surrounding electron gun which also secures cathode lens at correct distance from anode lens

P - Tantalum cathode lens element

Q - Tungsten dispenser cathode

R - Water jacket enclosing electron gun

S - Cathode stainless steel supporting base

T - Al_2O_3 insulators

U - Molybdenum backplate (this plate can be biased relative to cathode in order to prevent electrons from exiting cathode shield region)

AA - Photon limiters - $\otimes$ marks the focal point of the analyzer

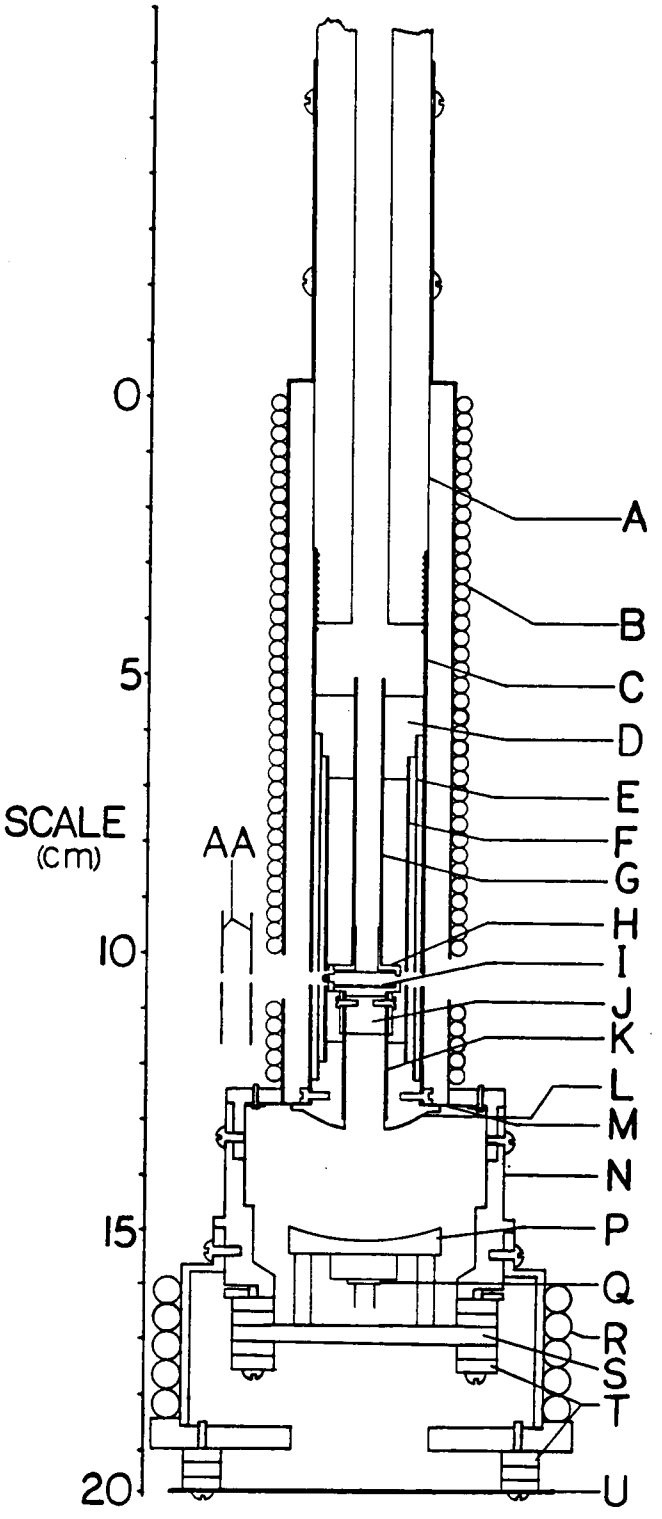

Figure 17.

serves as the anode of the electron gun lens system. These two end pieces have cylindrical steps with radii corresponding to the two different tube diameters. Once the sheets of tungsten and tantalum have been cut to the correct size, two 2 mm diameter holes are punched in each sheet. These holes are positioned so as to be diametrically opposed when the sheet is rolled into a tube, thereby allowing the ion beam to pass through. The center of the molybdenum plug has a 0.64 cm hole bored through it to accomodate the 0.55 cm id tungsten gas feed tube (G). H_2 gas is delivered to the tungsten gas feed tube from the gas handling system via the stainless steel supporting rod (A). A 1 cm hole through the center of this rod feeds H_2 gas into a buffer region on the cooler side of the molybdenum end plug. This buffer allows the molybdenum end plug to be moved relative to the oven (H) in order to allow for fitting the tungsten and tantalum radiation shields. One end of the gas feed tube passes through the molybdenum end plug into this buffer region and the other end fits over the gas port of the oven.

The main oven assembly, including the gas feed tube, oven, tungsten plug, and electron tube, is positioned between the molybdenum radiation shield support (D) and the tantalum anode lens element (L). The two inner radiation shields (E) and (F), are then attached, one at a time, so as to clamp (D) and (L) together. The result is a rigid construction consisting of (D) - (L). After the tantalum electron baffle (M) is positioned, the entire assembly is inserted into the molybdenum radiation shield (C). The tantalum anode lens element (L) is secured to the end of this molybdenum shield. Securing of the tantalum end cap was critical since, when oven assembly was placed vertically into the vacuum chamber,

the end cap prevented everything inside the molybdenum tube from sliding out. The outer molybdenum shield had threads which allowed it to be screwed onto the supporting rod (A). Before screwing the two pieces together, powdered graphite was applied to the threads to prevent the two pieces from sticking to one another when the oven was heated.

It was found that 0.051 mm provided adequate allowance for fitting together oven parts of the same metal, i.e., gas feed tube to oven gas port and oven aperture to oven. The tungsten plug, however, had a radius of 0.216 mm less than the electron feed tube since this plug could heat much more quickly than the surrounding tube. It was found that plugs with larger radii became welded to the electron tube during heating and, therefore, required machining in order to extract them. The hole in the molybdenum end plug for the gas feed tube had a 0.05 mm larger radius than the gas feed tube. Although this would have been a rather loose fit, inserting a piece of .025 mm tungsten sheet around the gas feed tube where it passed through the molybdenum end plug made the tube fit snugly inside the end plug without welding during heating.

The main function of the water jacket was to maintain a thermal environment inside the vacuum chamber which would not be harmful to either the electron spectrometer or the vacuum chamber. The jacket was required to perform two other important functions as well: One of these was to act as a support for the electron gun assembly and the other was to act as an enclosure preventing electrons from the gun from reaching the spectrometer.

The water jacket has two cylindrical sections of different radii which were machined from a single piece of oxygen-free copper. The smaller radius cylinder was machined to fit snugly over the support rod

and once it was secured by screws to the support rod, the water jacket exhibited no detectable motion relative to the support rod. This absence of motion was necessary in order to correctly position the electron gun system. The larger radius cylinder formed a shell around which water coding tubes were soldered. Two 3/16" copper tubes were wrapped side by side to form a spiral around the water jacket in order to afford a high water flow and, at the same time, minimize the overall size of the water jacket. Mini-Conflat^{R} flanges were silver soldered to the ends of these lines. Water was brought into the vacuum chamber through a single 1/4" tube, while another 1/4" tube served as a drain line. The in-vacuum water line connections were all made with Mini-Conflat^{R} flanging, since the seals afforded by these fittings helped in attaining the base pressure of 8×10^{-8} Torr when operating the oven. Since the oven assembly and water jacket were supported by the stainless steel oven support which in turn was connected to a high precision X-Y-Z manipulator while the water lines were attached to a separate, fixed flange, some flexibility was required in the water lines in order to allow movement of the assembly. This was accomplished by inserting some 1/4" stainless steel flexible tubing between the water jacket lines and the water lines coming from outside the chamber. Of course, these flexible tubes had Mini-Conflat^{R} flanges as well, and although use of the Mini-Conflat^{R} flanging for the water connection required slightly longer assembly times, the reliability of these seals was well worth the time.

Fitting over the anode lens end of the water jacket was the copper cathode support (N). This piece was also machined from a single piece of oxygen-free copper and had cylindrical symmetry. A counterbored

radius on one end of the cathode support allowed it to slide over a cylindrical projection on the end of the main water jacket. The 1.3 cm overlap provided an effective physical barrier to any electrons inside the gun region. The support was secured to the water jacket by means of four stainless steel screws. At the other end of the cathode support were four tapped holes by which the cathode support base (S) could be secured to the cathode support with stainless steel screws. The stainless steel cathode support base was electrically insulated from the copper cathode support by means of 6 mm id quartz sleeves and alumina spacers (S). The cathode support base was bolted to the cathode support which automatically positioned the cathode lens element at exactly the right position required for optimum focusing of the electron beam.

The copper electron gun water jacket (R) fitted over the end of the cathode support. A 1/4" copper water line was wrapped around this shield several times and silver soldered in place. This water line provided extra water cooling to this end of the water jacket assembly and was connected to the other water lines by means of Mini-Conflat^{R} flanges. The back end of the electron shield had an $\sim$2.5 cm diameter hole centered in it. This hold provided the only means for pumping out the electron gun region. Covering the hole in the electron shield and supported by stainless steel screws which were insulated with 6 mm id quartz sleeves and alumina spacers (T) was the bias plate (U). This bias plate was a solid 0.5 mm thick disc of molybdenum with a diameter of $\sim$6.5 cm and it was positioned $\sim$1.0 cm away from the back of the electron shield. Its function was to prevent electrons from leaving the electron gun region while still allowing adequate pumping of the gun region.

Three wires were required for the three electrical connections to the oven assembly inside the vacuum chamber. Two wires, which provided electrical connections to the cathode (Q) and cathode lens element (P), were each made by twisting together three 0.25 mm diameter molybdenum wires in order to reduce electrical resistance. Molybdenum wire was required since the connections had to be made inside a very hot region ($\sim 800^{\circ}C$) and copper wire would have outgassed severely in this region while stainless steel wire would have been too stiff. The two wires were each connected to a stainless steel screw protruding from the cathode lens base plate. The other end of each of the screws was insulated from the cathode base plate by means of quartz sleeves and alumina spacers. The molybdenum wires exited the gun region by passing between the electron shield and the molybdenum bias plate. Each wire passed through separate 6 mm id quartz tubes which were placed in the space between the bias plate and electron shield. The wire providing connection to the bias plate was the third wire inside the chamber. Each of these three wires passed through separate pyrex tubes of $\sim$10 mm id and 7.5 cm length. These tubes prevented the bare wires from making contact with the chamber walls and were wrapped with molybdenum wire which was grounded in order to reduce electrical charging of the outer wall of the pyrex insulators. Electrical connections to outside the vacuum chamber were made through two separate flanges. The cathode filament power and high voltage for the electron gun lens system went through one flange and the bias plate connection went through another flange. Both of these flanges bolted onto the same large side flange of the vacuum chamber.

Both the cathode and anode lens elements were made of tantalum. Although molybdenum was first tried, it was found that severe sputtering of the anode surface resulted after prolonged use. The durability of the tantalum parts seemed to be adequate, as the original tantalum parts were used for over 350 hours with little significant deterioration. The efficiency of the heating of the oven by the gun was found to be almost independent of the distance between the anode and the tungsten plug at the oven for distances of 1.9 cm to 4.83 cm. However, the useful lifetime of the tungsten plug and the tube surrounding the plug were critically dependent on this distance. In the first prototype, the plug was positioned at the point of minimum beam diameter calculated from the results of Appendix D; for the parameters used here, this corresponded to 4.83 cm. The tungsten plug deteriorated very quickly due to intense, local heating at the spot on the plug which the electron beam struck. The position of the plug was changed so that the beam diameter at the plug was the same as the plug diameter. Although at this position the plug showed little sign of sputtering or melting, the electron feed tube was vaporized at the point where the beam struck. The optimum position of the plug was found to be a point between these two extremes which was the center of the radius of curvature of the anode lens element, i.e., 2.54 cm. This position provided a maximum heating efficiency combined with a much slower rate of sputtering of the plug surface. The plugs required replacement after $\sim$60 hours of high temperature operation ($\sim$2400K) of the oven. At lower temperatures ($\sim$2300K) the average lifetime of the plugs was $\sim$90 hours. In order to protect the oven wall adjacent to the plug, replacement of the plug was routinely performed

with these lifetimes being used as the time limit for operation of the oven with a given plug.

The placement of the oven assembly relative to the electron spectrometer is shown in Figure 18. The electron spectrometer was positioned so that the plane containing the electron paths through it was normal to the cylindrical symmetry axis of the oven assembly, i.e., out of the page in Figure 18. Note that the oven assembly is suspended vertically in the vacuum chamber.

Electron Gun

The electrical schematic for the electron gun is shown in Figure 19. The BaO activated tungsten dispenser cathode used in the gun required an optimum operating temperature of $\sim 1100^{\circ}C$ at the emitting surface. The cathode temperature was controlled by increasing or decreasing the current through a heater filament with the variable output transformer (Variac) shown in Figure 19. This cathode typically required a conditioning period after which operating temperature was maintained with a filament current of ~ 2.5 amps and filament voltage of ~ 10.0 VAC. The high voltage power supply was a converted 10 KW electron beam welder power supply. The negative high voltage required for the electron gun cathode element was supplied to one side of the filament heater which was electrically in common with the cathode outer can, cathode base plate and also the cathode lens element. The other end of the filament heater was electrically isolated, except through the filament itself. This electrical isolation was easily obtained since the voltage difference between the two sides of the filament heater was only ~ 10 VAC. All of the emission current was supplied by the high voltage power supply and could be directly monitored by means of an ammeter.

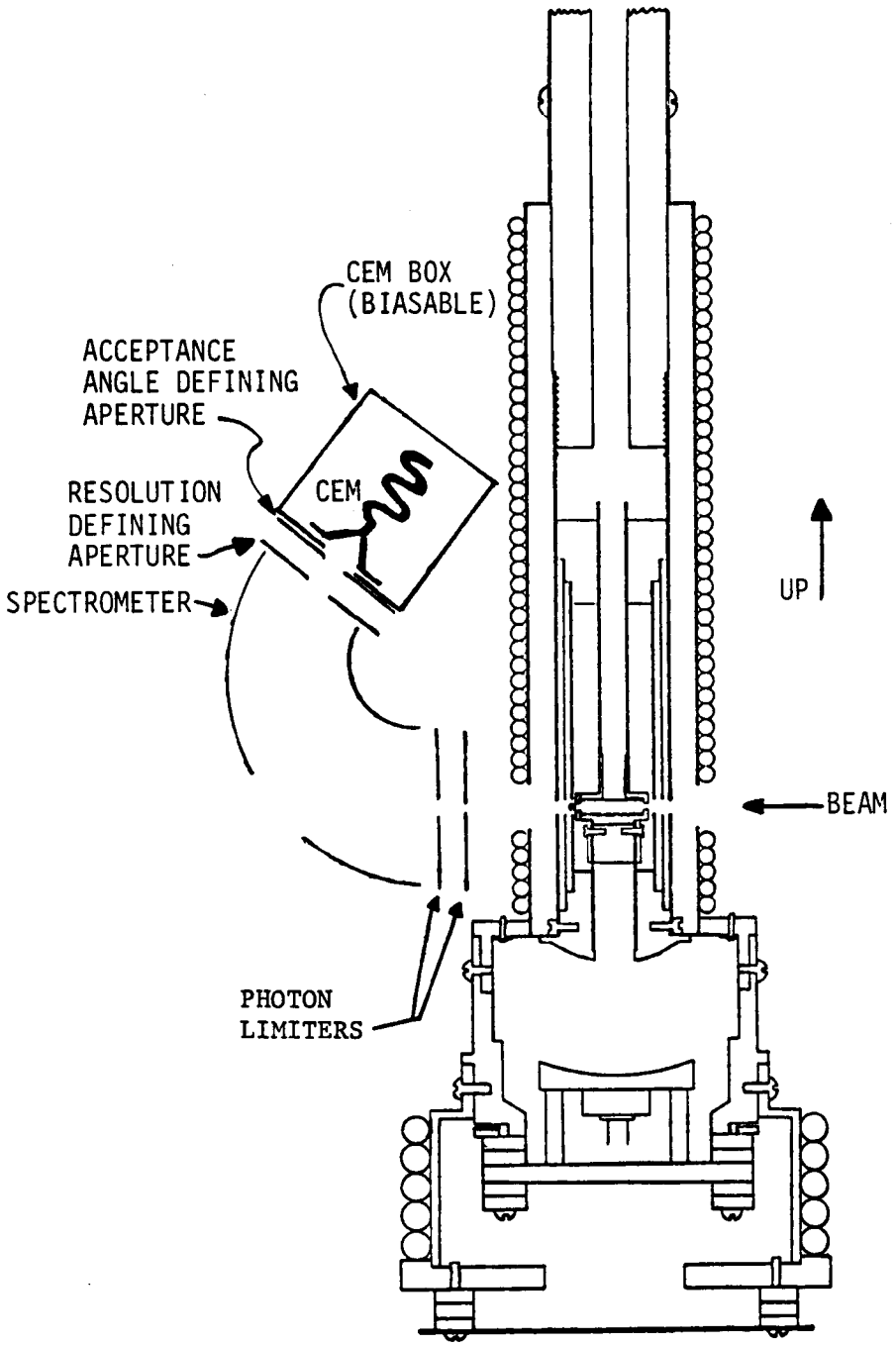

Figure 18. Placement of Electron Spectrometer.

The electron spectrometer is supported so that the electron path is in a plane normal to the cylindrical axis of the oven assembly, i.e., out of the page. The oven assembly is supported from above by an X-Y-Z high precision manipulator.

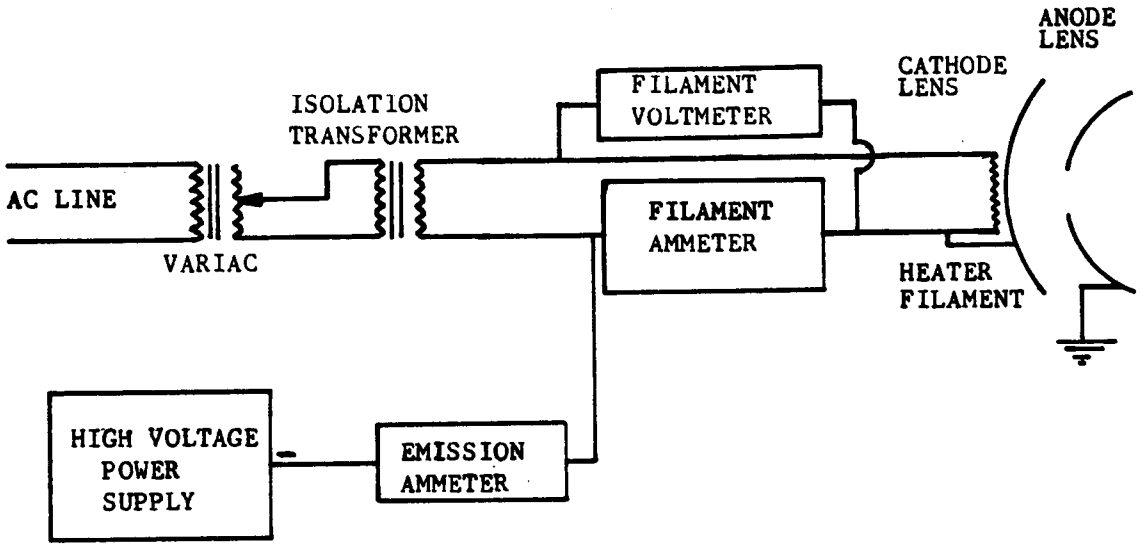

Figure 19. Electrical Schematic for Oven Heating Electron Gun.

The principles upon which the electron gun was designed are explained in detail in Appendix D. Table IV summarizes the physical characteristics pertinent to the construction of the electron gun as well as important parameters of actual operation. The cylindrical dispenser cathode with emitting surface on one end fit into a hole in the center of the cathode lens element so that the cathode's emitting surface was flush with the inside surface of the lens element. Although the lens element surface was spherical while the cathode emitting surface was flat, the lens element surface with the cathode in place closely approximated that of a spherical surface and the focusing properties of the lens were not adversely affected. It was found that the actual emission current of the electron gun exceeded the theoretical current as given in Appendix D, equation (D.5) by a factor of three or more. By enlarging the theoretical emitting angle of the cathode (see Appendix D) so that the electron paths from the cathode were limited by the radius of the hole in the anode, the experimental emission current was found to be comparable to the predicted current.

TABLE IV

ELECTRON GUN CHARACTERISTICS

Cathode - BaO filled tungsten dispenser cathode (Spectra-Mat Std 300) with tungsten heater.

Cathode lens element - Concave tantalum spherical sector lens with 5.08 cm radius of center of curvature.
Sector half angle = 19°.
0.76 cm diameter dispenser cathode fitted in hole through center of lens.

Anode lens element - Convex tantalum spherical sector lens with 2.54 cm radius of center of curvature.
Sector half angle = 39°.
Electron passage hole = 0.89 cm diameter.

Cathode lens element to anode lens element spacing = 2.54 cm.

Effective emitting surface of cathode lens element ≅ 25% of surface (see Appendix D).

Power Requirements: heater filament - 2.5 amp at 10 VAC.
Oven heating 200 ma at ∿7 kV.

There are three possible explanations for this discrepancy, one of which is that the space charge immediately in front of the cathode prevents electrons from being emitted in the forward direction but since a ground potential (the water jacket) exists around the cathode these electrons tend to move outward along the cathode lens surface until the space charge is low enough so that they are able to be accelerated toward the anode lens hole. This would make the apparent emitting surface larger than the physical size of the cathode. This phenomenon is basically the observable effect of the departure from spherical symmetry of the potential between the lens elements. The second possibility is that

once the cathode lens element becomes hot enough it begins to emit electrons which add to the emission current. The cathode lens element faces the tungsten plug on which the electron beam deposits the largest portion of its energy. This is the hottest part of the oven assembly and, because of this, the lens element may be heated by blackbody radiation emanating from the plug region. The heating of the cathode by blackbody radiation, in addition to the heat conducted away from the hot cathode itself ($\sim$1100^{o}C), could easily induce emission from the lens element surface. The fact that additional heating of the cathode occurs was established by a decrease in the filament heater current required for a given emission current once the oven had been heated for a short time.

The power delivered to the oven by the electron beam could be varied in one of two ways: Either changing the high voltage holding the emission current constant or, alternatively, keeping the high voltage constant and changing the emission current. It was found that high temperature operation required higher voltages and less emission current. This was due mainly to space charge effects on the electron beam since, for a given cathode-anode lens element voltage, there is a limiting amount of current that can be emitted from the cathode (see Appendix D). Increasing the temperature of the cathode will not increase the emission current indefinitely but will it reach a maximum emission which depends on what potential exists between the cathode and anode lens elements.

The dispenser cathode could not be exposed to atmospheric conditions for long periods since reactivation of the emitter becomes more difficult and eventually impossible after contamination, especially with H_2O. For

this reason, whenever the oven assembly was exposed to air for periods longer than two hours, the cathode lens element assembly (P in Figure 17, page 85) supporting the cathode lens and the cathode lens supporting base (S in Figure 17, page 85) were removed as an integral unit and placed inside a separate vacuum chamber. The chamber was maintained at a pressure of ≤10 mTorr and the cathode could be stored for periods of at least one month with no noticeable deterioration in emission. The molybdenum wires attached to the cathode filament heater remained connected during this process in order to prevent breaking the tungsten filament heater wires which became relatively brittle after being heated. The lifetime of an individual cathode was extended to as long as six months even with many cycles of the vacuum system.

Temperature

As mentioned earlier, the position of the tungsten plug relative to the opening in the anode lens element had to be optimized for maximum lifetime of the tungsten plug. It was found over several months of testing that the position of the plug did not significantly change the power required to heat the oven to a given temperature. The horizontal axis of Figure 20 is a measure of the emission current of the electron gun multiplied by the high voltage applied to the cathode lens element while the vertical axis is the temperature of the oven. As seen from the figure, there is no significant deviation from linearity between temperature and beam power over the range of temperatures shown. This is especially satisfying for the higher electron gun powers since it indicates that the heat being lost due to radiation through the radiation shields and thermal conductivity was not limiting the temperature attainable.

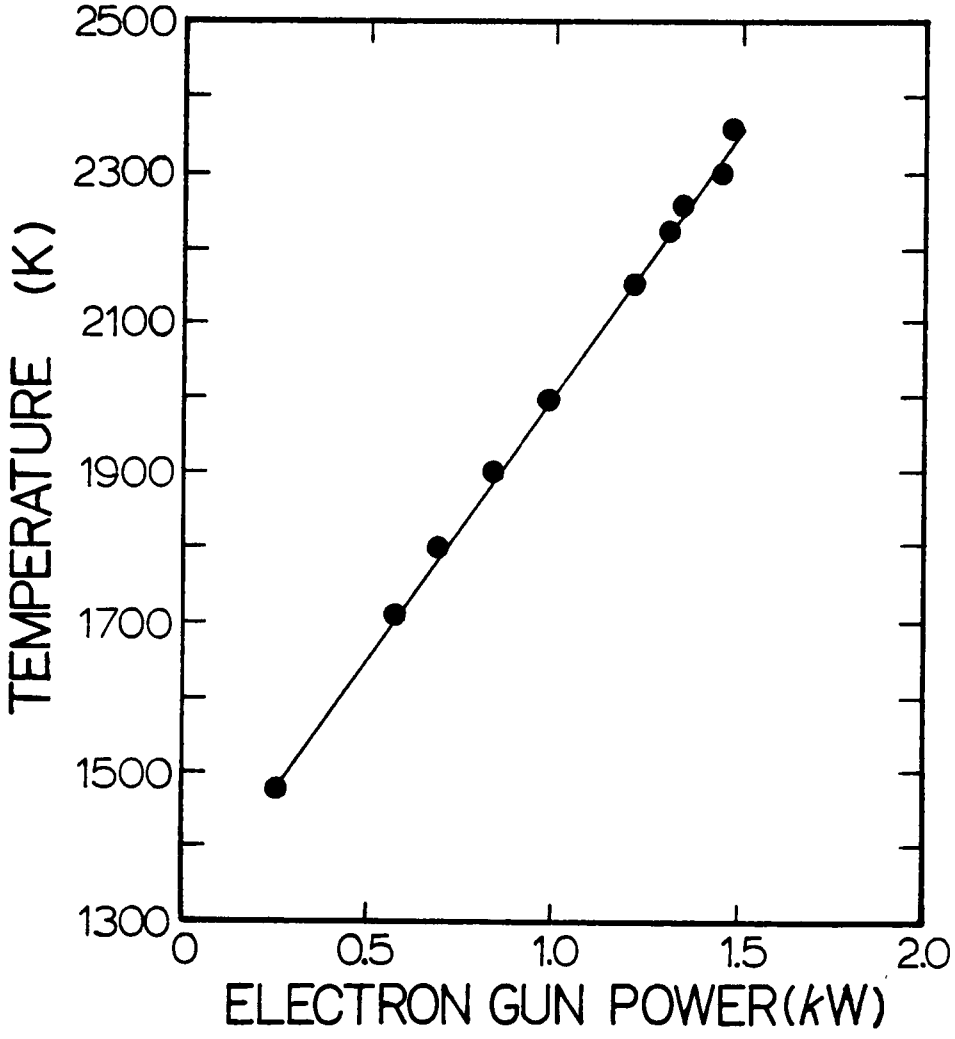

Figure 20. Temperature of Oven Versus Electron Gun Power.

Note that the temperature curve remains linear even at higher temperatures indicating that there is not yet significant heat loss by thermal radiation or conduction. High temperatures required higher voltages and lower current than did low temperatures.

in the oven. The temperatures shown in Figure 21 are corrected for the optical transmission properties of the mirror-window system through which the oven was viewed by an optical pyrometer (described in further detail on page 111). This correction (see Figure 25, page 112) amounted to an addition of 30 K to the temperature read on the pyrometer.

The dispenser cathode required a conditioning period to attain maximum electron emission. Once the cathode emission was optimized, it was necessary to also follow a conditioning procedure for the entire oven assembly in order to attain high oven temperature. This conditioning procedure consisted of slowly increasing the temperature of the oven over a period of two to three hours. This gradual heating process allowed the high-temperature oven surfaces to outgas slowly and steadily. The type of dispenser cathode used required fairly good vacuum ($\lesssim 1 \times 10^{-5}$ Torr) for optimum emission, as severe outgassing of surfaces inside the electron gun enclosure could poison the emitting surface of the cathode. Also, outgassing inside the electron gun enclosure was occasionally observed to produce sparking due to plasma conduction between the high voltage leads and the grounded water jacket enclosure. Controlled outgassing of contaminants from the surfaces therefore required gradual heating of the oven. Since the oven assembly was constructed from three basic metals tungsten, molybdenum, and tantalum, different parts of the oven assembly had varying thermal expansion coefficients. Although the number of these dissimilar metal joints was a minimum, it was still considered to be essential that the oven heated slowly to prevent parts adhering to one another. Once the oven had been operated at high temperature and subsequently cooled, very little additional

conditioning was required to attain high temperature again, provided the vacuum chamber had not been exposed to the atmosphere after the initial conditioning.

Background Rates

Of critical importance was the elimination of background or noise counts being registered by the electron CEM during the acquisition of an ECC spectrum. The Ceratron EMS 1081B CEM has a nominal dark current of 0.1 counts per second.[50] This count rate is smaller than the expected ECC count rates on atomic hydrogen. Also, since the noise due to the CEM is random in nature, the background counts accumulated in the ECC spectrum will be randomly dispersed throughout the spectrum. The resulting background is therefore small and independent of the energy of the electron being analyzed by the spectrometer. Of major concern, therefore, was the background produced by sources other than the CEM itself. Assuming that the background due to the ion beam collimation could be eliminated as discussed earlier (see page 50), the only remaining source of extraneous electron counts was the oven itself.

Unacceptable background signals registered by the CEM could be produced in one or more of the following ways: 1) electrons escaping the electron gun region (200 mA $\approx 10^{15}$ electrons/sec), 2) Bremsstrahlung X-rays produced by high energy (7 keV) electrons impacting surfaces around electron gun, 3) thermionic electrons emitted by the hot oven, and 4) blackbody photons emitted by the oven. Backgrounds due to electrons escaping from the electron gun could be prevented by two design features of the oven assembly. Physical barriers stopped a large fraction of these electrons from getting out of the gun region. The

copper water jacket enclosing the gun lens elements [(N) and (R) of Figure 17, page 85] along with the tantalum baffle [(M) of Figure 17, page 85] eliminated any unobstructed direct or indirect path by which the electrons could get out of the gun region. The electron spectrometer was covered by 0.13 mm thick tantalum sheet to prevent non-analyzed electrons from getting between the sectors. The bias plate [(U) of Figure 17, page 85] covered the pumping hole in the rear of the gun enclosure and by applying a small positive bias of +200 V it was found that relatively few electrons could then exit the region. The physical reasons of why a positive potential was required are not obvious. When first designing the oven, it was known that these electrons had to be prevented from exiting the gun region but, at the same time, the cathode required a vacuum region in which to operate satisfactorily. These two requirements are seemingly in contradiction to one another unless the gun region could be pumped independently of the main vacuum chamber, which was impractical. The pumping hole in the rear of the water jacket provided the only access through which the gun region could be evacuated. The bias plate was added to provide a means by which the trajectories of charged particles could be affected. The original intention was that the bias plate be given a negative potential with respect to the gun cathode lens element. This additional negative potential would serve to repel even the highest energy electron attempting to exit the region. However, since the region around the lenses was so hot, and since there was a fairly high density of electrons in the electron beam, a positive ion plasma was produced by outgassing atoms being ionized by the electron beam. These positive ions were then

attracted to the largest negative potential in the immediate area - the potential on the bias plate. The ions attained relatively high energies by the time they struck the bias plate, thereby producing approximately one secondary electron for each ion colliding with the plate. Many of these electrons were then repelled by the negative potential on the plate. Many were forced out into the vacuum chamber, thereby creating a sea of electrons in which the CEM resided. The background produced by these electrons was independent of analyzer voltage and, therefore, was caused by electrons (or Bremsstrahlung X-rays from these electrons) colliding with the CEM cone without passing through the analyzer. It is also believed that some electrons exiting the pumping hole at small angles could be forced out into the vacuum chamber by the electric field between the negative bias plate and the grounded water jacket. By applying a positive potential to the bias plate positive ions were repelled while electrons were attracted to the plate. The electrons which hit the plate produced only a relatively small number of secondary electrons and these electrons were also attracted toward the plate. The end result was that fewer electrons were able to exit the region and those that did exit probably had a much lower energy and, consequently, less chance of producing counts in the CEM. Any Bremsstrahlung X-rays produced by the electrons hitting the plate or any surface in the gun region required several changes in direction in order to reach the CEM. The probability of these X-rays reaching the CEM was therefore much lower than the X-rays produced by relatively high energy electrons (in the case of negative bias) hitting surfaces close to the CEM cone.

Any low energy electrons emitted by the hot oven were prevented from reaching the CEM by the fields produced by the sectors of the electron analyzer. Blackbody photons, however, could scatter through the sectors to reach the CEM. Even after the gun region had been sufficiently enclosed, there was still a relatively low background count rate of 1-2 counts/sec which seemed to be independent of voltage on the analyzer sectors and also dropped relatively sharply, as seen in Figure 21, when the negative bias on the box enclosing the CEM was approximately equal to the potential on the analyzer outer sector for a fairly wide range of analyzer voltages. This seemed to indicate that the

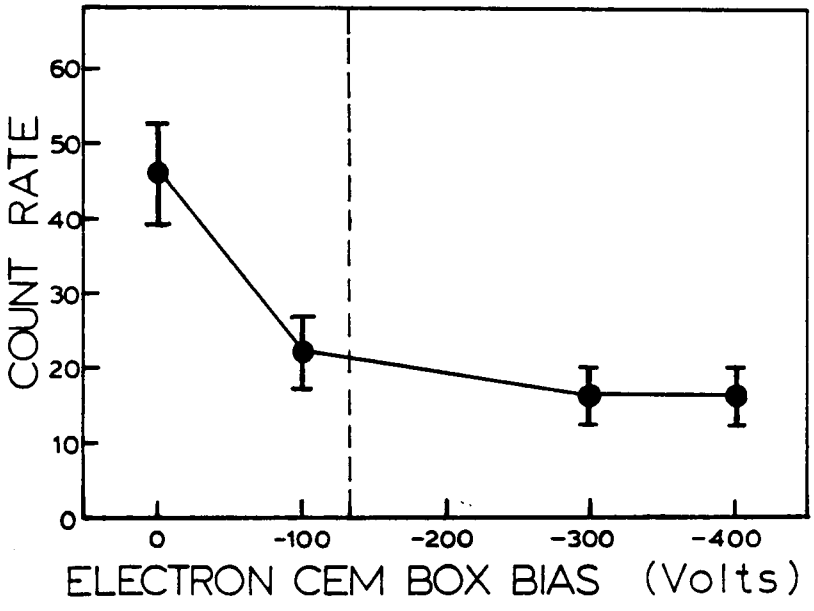

Figure 21. Background Count Rate Versus Electron CEM Box Bias.

The sharp drop in count rate occurs close to the potential corresponding to the potential on the outer sector plate which is denoted by the dotted line. The solid line connecting the data points is merely a visual aid. These count rates were obtained with the analyzer voltage set to analyze cusp electrons, i.e., electrons with energy 544.4 eV.

background was due to charged particles and these particles were not being energy analyzed by the spectrometer. Furthermore, since a negative bias potential on the CEM box reduced the count rate, these particles were probably electrons and probably being produced on the inside surface of the outer sector because the relatively sharp decrease in count rate at the bias potential corresponding to the outer sector potential showed that the electrons were probably created with relatively high energy. Photoelectrons produced by blackbody photons are normally low energy ($\sim$ eV) but if these electrons are produced at a surface of negative potential, the resulting energy of the ejected electrons will be appropriate to the potential at the surface. The explanation for this electron background seems to be that photoelectrons are produced at the surface of the outer sector near the exit of the analyzer. These electrons are then accelerated by the negative potential on the sector to a relatively high energy. Prevention of this electron background required three modifications to the physical apparatus. The first change was the addition of the two photon limiters between the oven and the analyzer entrance. These limit the cone of radiation that can impinge on the inside surface of the outer sector near the beam exit hole (see Figure 10, page 70). Secondly, the surfaces of the sectors, both inner and outer, near the entrance and exit of the analyzer were coated with carbon by application of a colloidal solution of graphite in alcohol. The carbon coating left after the alcohol evaporated reduced secondary electron emission and also increased the probability that a photon would be absorbed rather than scattered because the coating produced a microscopically rough surface without disturbing the transmission properties

of the spectrometer. The third modification was electrically connecting the CEM cone and CEM box to a common -300 V bias potential. The back bias of the CEM was, of course, changed appropriately to give a +4 kV potential difference between the CEM cone and the CEM back. Since the experimental spectra covered a range in electron energies of 480-600 eV the -300 V bias would not seriously affect the paths of electrons from the cusp but would repel those electrons produced at the outer sector. The CEM cone and the box, being only 2 mm apart, were connected in common in order to approximate a planar negative potential surface thereby allowing a more efficient separation of "noise" electrons from cusp electrons. This procedure also minimized any focusing effect of the hole in the CEM box through which the analyzed electrons passed.

After all modifications had been completed, the electron background count rate was found to be <1/sec with an ion beam passing through the hot oven. This count rate was essentially constant over the entire spectrum of energies being scanned and it is doubtful that there should be a realistic expectation of decreasing this background still further.

Determining Oven Pressure for a Dissociating Gas

The formulae necessary for the determination of the oven pressure have been derived and were shown to apply for any gas in a cold oven and for any nondissociating gas in a hot oven. However, it is now necessary to derive the corresponding relations for the dissociating hydrogen gas. Since molecular hydrogen will not be 100% dissociated inside the oven, the relative amounts of H and H_2 in the oven must be determined if corrections are to be made for the H_2 impurity in the atomic hydrogen target.

The following discussing assumes that thermal and chemical equilibrium conditions exist inside the oven.

Assuming that only H_2 enters the hot oven from the gas handling system, conservation of mass flow gives[27]

$$2n_2v_2 = 2n_2^*v_2^* + n_1^*v_1^*, \tag{65}$$

where $n_i \equiv$ number of particles/volume (1=H, 2=H_2), $v_i \equiv$ velocity of particle, and (*) denotes a hot oven. Using

$$P_i = n_i kT, \tag{66}$$

and

$$v_i \propto \sqrt{\frac{T}{m_i}}\ , \tag{67}$$

then

$$P_2\sqrt{\frac{2}{T}} = P_2^*\sqrt{\frac{2}{T^*}} + P_1^*\sqrt{\frac{1}{T^*}}\ . \tag{68}$$

The dissociation fraction is defined as[27]

$$f \equiv \frac{P_1^*}{P_1^*+2P_2^*} = \frac{n_1^*}{n_1^*+2n_2^*}\ . \tag{69}$$

Combining (69) with (68)

$$P_2^* = \sqrt{\frac{T^*}{T}}\left[\frac{1-f}{f(\sqrt{2}-1)+1}\right]P_2. \tag{70}$$

Also using (69)

$$P_1^* = \frac{2f}{1-f} P_2^* = \sqrt{\frac{T^*}{T}} \frac{2f}{f(\sqrt{2}-1)+1} P_2. \qquad (71)$$

Equation (70) and (71) relate the partial pressures of H and H_2 inside the hot oven to the H_2 pressure in a cold oven. These relations hold true only if the flow rate of H_2 into the oven cold is the same as the flow rate of H_2 into the oven hot. Note that equation (65) does not equate cold flow rate into the oven with hot flow rate into the oven but merely states that the H_2 gas going into the hot oven comes out of the hot oven as a mixture of H and H_2, i.e., whatever goes into the oven must also come out. This may seem at first to be a rather obvious and trivial statement, but it is the basis for all of these pressure relations. The calculation of the dissociation fraction also depends on this conservation of mass equation. By adding equations (70) and (71), the expression for the total pressure inside the oven can be obtained. It is given by

$$P^* = \sqrt{\frac{T^*}{T}} \frac{1+f}{f(\sqrt{2}-1)+1} P_2. \qquad (72)$$

Figure 22 is a plot of P_1^*, P_2^*, and P^* using equation (70) through (72). These results, relating the total pressure in the oven to the dissociation fraction, are needed to obtain plots of isothermal curves which give the equilibrium dissociation fraction as a function of pressure for a given temperature.

Perhaps of more importance is the number density inside the oven. By using $P = nkT$, the relations (70) through (72) can easily be converted to expressions giving the number density inside the oven as a function of the dissociation fraction. These plots are shown in Figure 23.

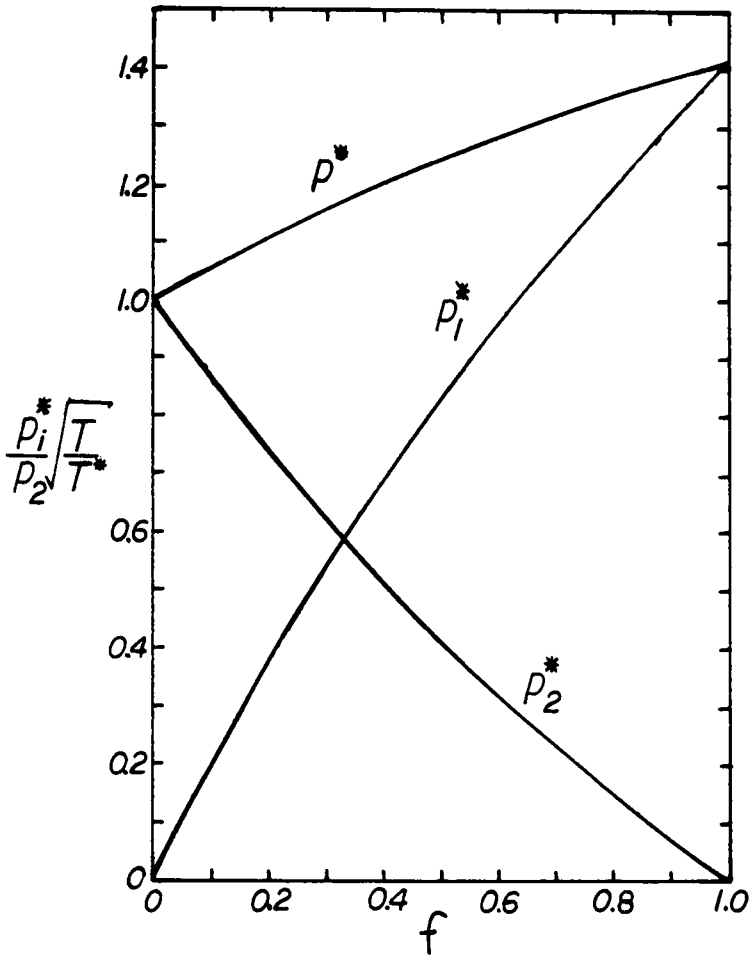

Figure 22. Atomic and Molecular Hydrogen Pressures Inside Hot Oven.

P_1^* and P_2^* denote partial pressure of H, H_2, respectively, and $P^* = P_1^* + P_2^*$.

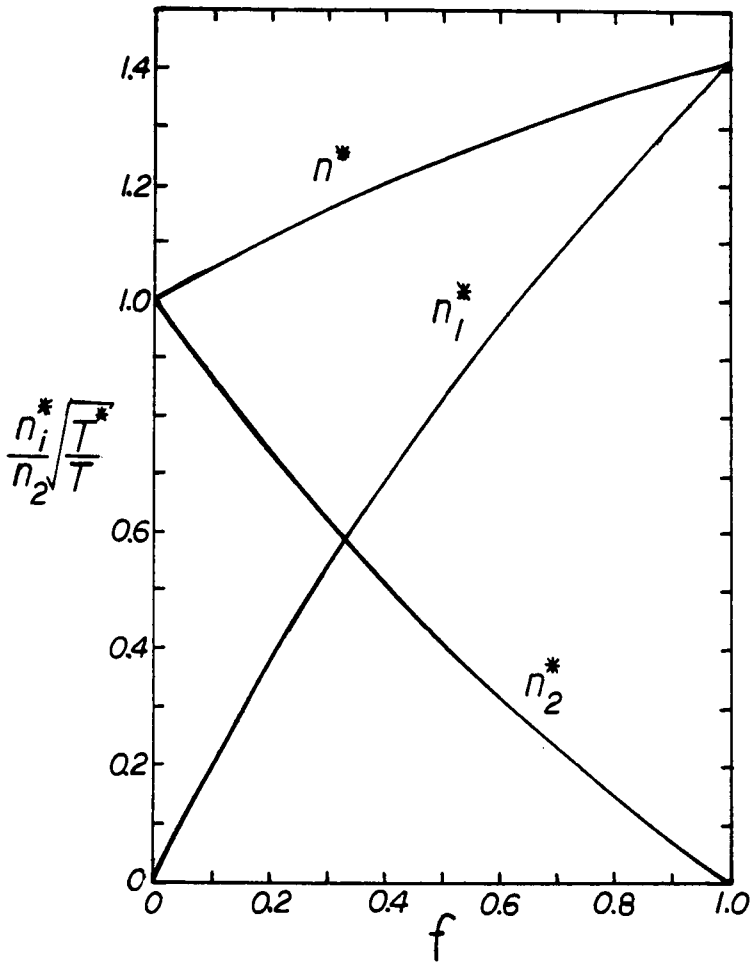

Figure 23. Atomic and Molecular Hydrogen Densities Inside Hot Oven.

n_1^* and n_2^* are the partial number densities for H and H_2, respectively, and $n^* = n_1^* + n_2^*$.

Temperature Correction for Mirror-Window Transmission

The temperature of the oven could be read using an optical pyrometer. By inserting a moveable mirror directly behind the beam passage hole in the electron spectrometer (see Figure 6, page 42), the oven could be observed. A calibrated filament inside the pyrometer was electrically heated until the oven and the filament were the same color. The temperature of the oven was then read directly off the scale of the pyrometer. The mirror was a front surface coated aluminized mirror which reduced refraction effects. However, there was still a possibility of a frequency dependent transmission of the light radiating from the oven after reflection by the mirror and transmission through the sapphire viewing window. If the mirror-window system preferentially transmitted lower frequencies, the temperature recorded would be less than the actual value. This transmission effect was tested by using a light source which connected to a variable output power supply. The pyrometer was positioned so that the filament in the light source could be read directly at one orientation, but a slight rotation of the viewing axis of the pyrometer would enable the same filament to be seen after the light had been reflected off a mirror and transmitted through a sapphire window. The temperature of the light filament was varied by changing the voltage provided by the power supply. Figure 24 shows that only an offset was required to correct for the transmission properties of the mirror-window system. This offset was added to all subsequent temperature measurements of the oven.

Experimental Determination of the Dissociation Fraction

Experimental determination of the dissociation fraction required the use of an additional CEM and associated electronics which is shown inside the dotted line in Figure 7, page 47. The ion CEM was located immediately

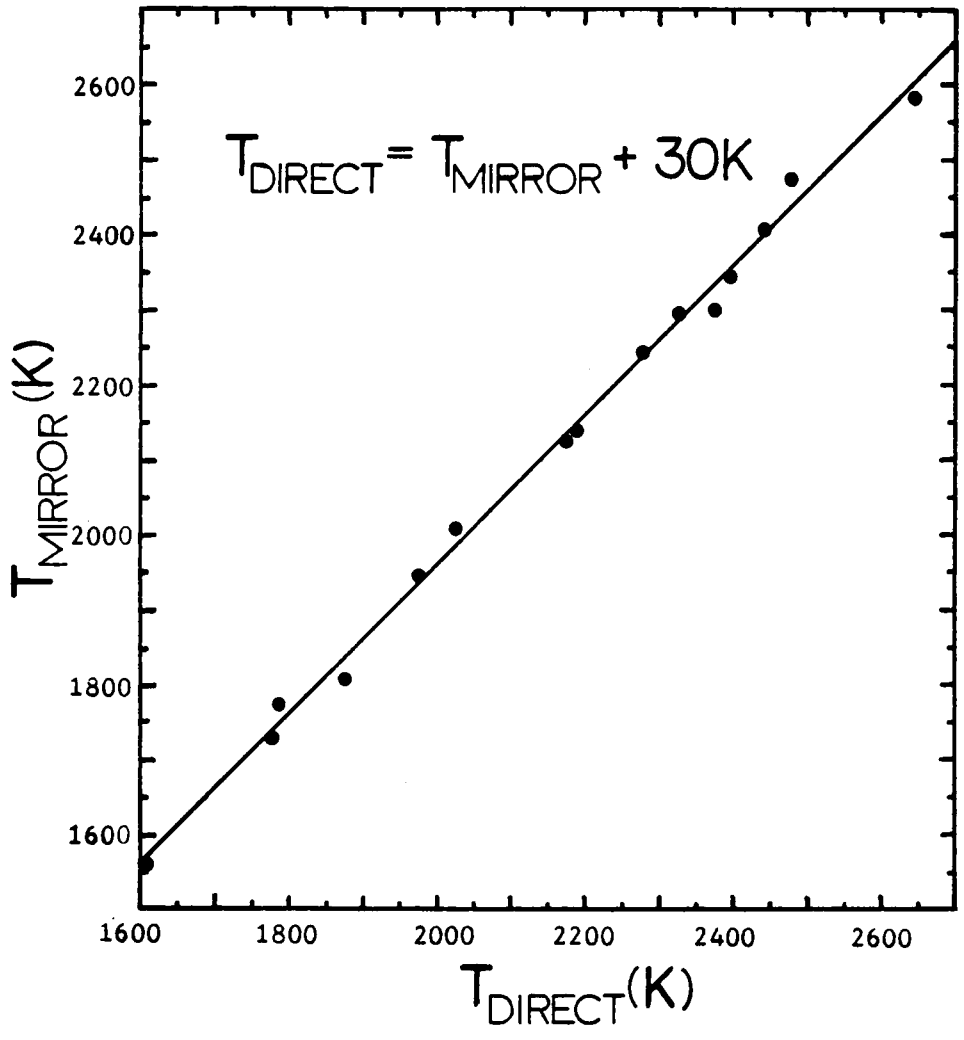

Figure 24. Correction of Oven Temperature Reading for Transmission Through Mirror-Window System.

The solid line is a least square fit to the data points. The actual temperature of the oven was determined using the relation $T_{direct} = T_{mirror} + 30K$, where T_{direct} is the actual oven temperature after the additive correction of 30K to the temperature read by the pyrometer T_{mirror}, through the mirror-window system.

behind a 6 mm hole in the rear of the Faraday cup and was supported by an arm attached to an X-Y manipulator. The particular method used for determining the dissociation fraction was the double capture method (see Appendix B). This method is based on the fact that some small amount of the incident ion beam will capture two electrons from the undissociated molecular hydrogen remaining in the oven. Assuming single collision conditions, if the ions that capture two electrons are counted, the dissociation fraction can be determined. The number of ions capturing two electrons for a given amount of ion charge collected is defined as the double capture yield. These ions were counted by the ion CEM when the magnetic field was set so that the desired final charge state was transmitted through the hole in the rear of the Faraday cup. The charge state was focused using the magnetic quadrupole doublet lens located immediately in front of the analyzing magnet. A negatively biased (-100 V) plate with an aperture immediately in front of the ion CEM cone opening prevented backscattered secondary electrons from escaping the CEM. The aperture in this biased plate was the same size as the opening in the CEM cone. The cone of the ion CEM was held at ground potential and the back was positively biased with the HV bias power supply. The pulses from the CEM were counted on the ion scaler after being processed by intermediate pulse shaping electronics. Counting time was determined by the amount of charge collected in the Faraday cup, and once a preset number of pulses was recorded by the timer/scaler, a gating pulse closed the gate of the ion scaler. The number of counts recorded by the timer/scaler was the double capture yield. Both (B.13) and (B.14) of Appendix B can be used for experimentally determining f. Equation (B.13) requires knowledge of the oven temperature while equation (B.14) requires the additional ratio

of double capture yields from argon. In principle, choosing which relation to use when determining f experimentally is dependent upon two factors: 1) whether or not the oven temperature T^*, can be determined by direct means, and 2) even if the temperature can be directly ascertained, it is possible that the yield ratio for argon which appears in equation (B.14) will be more accurate and precise than the directly obtained values of $\frac{T}{T^*}$. It would therefore be advisable to use whichever equation yielded the least error in measurement.

It can be shown (see Appendix A) that an expression for the dissociation fraction can be obtained by using the theory of chemical equilibrium. The resulting expression for f is given by

$$f = \sqrt{\frac{K_p(T^*)}{K_p(T^*)+4P^*}}, \tag{73}$$

where the dissociation constant $K_p(T^*)$, is given by (A.21) of Appendix A

$$K_p(T^*) = 4.814\text{x}10^6 \left[(T^*)^{3/2}\left[1-e^{\frac{-6325}{T^*}}\right]\right] e^{\frac{-5.2\text{x}10^4}{T^*}} \quad \text{mTorr.} \tag{74}$$

Note that $K_p(T^*)$ depends only on T^*, with a restrictive condition that ideal gas conditions exist; specifically, that the temperature not be so high that temperature induced molecular state transitions can occur. Because of this fact, equation (74) can be used to obtain either isobaric or isothermal curves, i.e., $f = f(T^*)_{P^*=\text{constant}}$ or $f = f(P^*)_{T^*=\text{constant}}$. It is a common practice[39,42,49] to compare experimental data with

$f(T^*)_{P^*=\text{constant}}$. The dissociation fraction is experimentally determined at several temperatures and compared with equation (73). However, since one of the objectives of the present oven design was to obtain the highest possible pressure inside the oven in order to allow the study of relatively low cross section phenomena, it was necessary to be able to quickly and easily determine the dissociation fraction for several pressures at a given temperature. This procedure was considerably simplified by comparing data to $f(P^*)_{T^*=\text{constant}}$. The oven temperature was easily obtainable by using the optical pyrometer. Once a particular oven operating temperature was attained (typically 2200-2400 K), the dissociation fraction could be experimentally determined to different oven pressures. The change in oven temperature due to changes in the gas flow rate was found to be $\lesssim 0.5\%$, which was considered to be negligible. Several isothermal curves plotted from equation (73) are shown in Figure 25. Observe that equation (72) on page 108 and equation (73) on page 114 are two independent calculations for the total pressure inside the hot oven. Equation (72) was based on gas flow conservation, while equation (73) was the result of thermal and chemical equilibrium conditions. Solving (72) and (73) for P^* and equating

$$\sqrt{\frac{T^*}{T}}\left[\frac{1+f}{f(\sqrt{2}-1)+1}\right] P_2 = \frac{K_p(T^*)(1-f^2)}{4f^2} \quad . \tag{75}$$

Using $P_2 = 0.408\ \Delta P_B$ mTorr from equation (59) gives

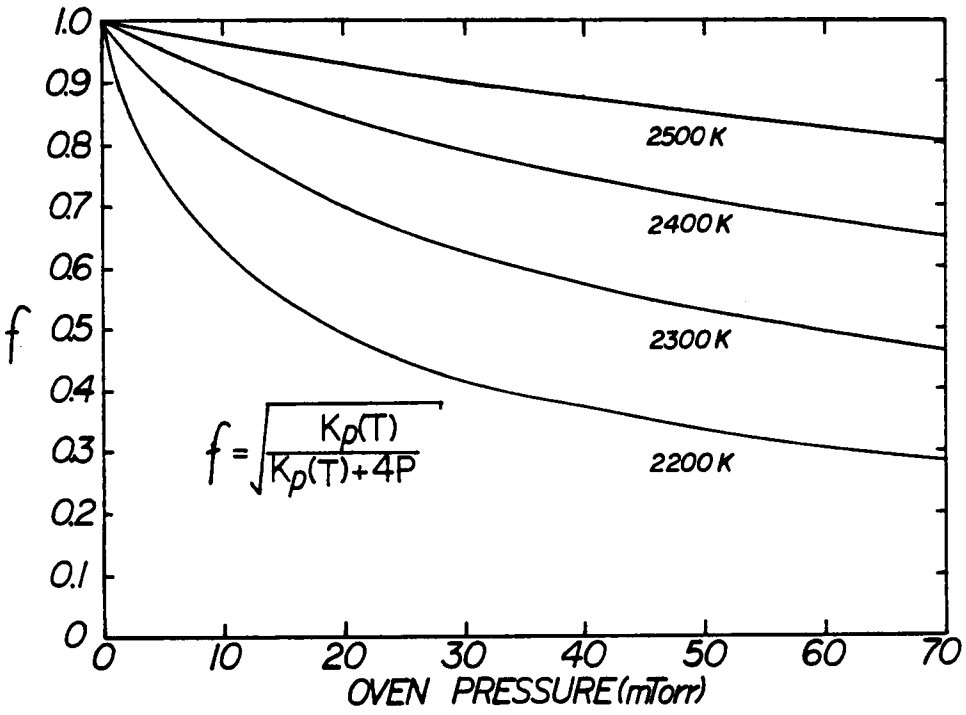

Figure 25. Dissociation Fraction Versus Pressure.

Isothermal curves plotted from equation (73).

$$\Delta P_B = 0.613 \frac{(0.414f+1)(1-f)^2}{f^2(f+1)} \sqrt{\frac{T}{T^*}} K_p(T^*). \qquad (76)$$

Equation (76) can be used to give the dissociation fraction as a function of the gas flow rate for a given temperature T. The value of $K_p(T^*)$ can be obtained from equation (74). The value of f obtained in this way can be used in lieu of an actual experimentally determined f as long as it is known that equilibrium conditions exist inside the hot oven. It is most convenient to plot isothermal curves using equation (76). Figure 26 gives $\Delta P_B(f)$ for $T^* = 2250$ K. Once ΔP_B is known, the value of f can be obtained graphically.

Although the isothermal curves obtained from equation (73) predict the dissociation fraction at a given oven pressure and temperature, experimental verification for the validity of the application of equation (73) for the oven is necessary. Several phenomena may occur which would render equation (73) invalid, or at least very inaccurate. If the molecular hydrogen flowing into the oven were to leak through spaces between the gas feed tube and its connections to the oven and other places, the gas entering the oven would be less than supposed and, consequently, the actual oven pressure would be smaller than the predicted value. The subsequent theoretically predicted dissociation fraction would be lower than the actual value. This discrepancy of both the pressure and the corresponding dissociation fraction could easily cause significant error in any experimentally determined cross section. In the case that a significant amount of hydrogen diffused through the walls of the hot gas feed tube or oven the same error in the dissociation fraction and

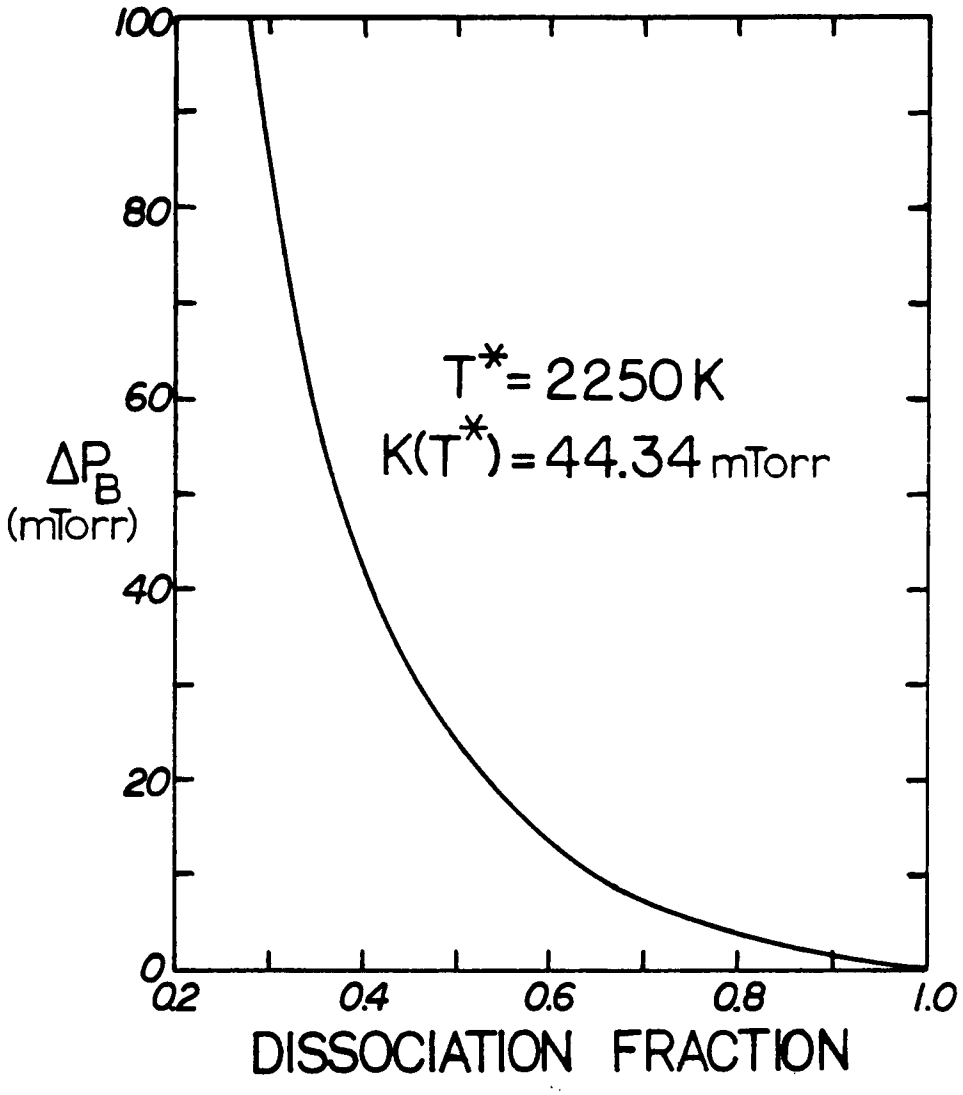

Figure 26. Pressure Difference Across Flow Aperture Versus Dissociation Fraction f.

Plotted from equation (76).

pressure could occur. It is also critical that the hot tungsten surfaces inside the oven are clean. If a monolayer of oxygen or nitrogen builds up on the surfaces the dissociation of molecular hydrogen can be slowed and, with extreme surface contamination, even halted. In that case, the oven may have to be heated for some period in order to allow outgassing of contaminants from the surface. The assumption that equilibrium conditions do exist within the oven is supported by the experimental evidence presented on page 124.

As stated earlier, the dissociation fraction was determined experimentally using the double capture method.[27] For this purpose, the ion beam chosen was 1.38 MeV C^{3+}. There were two reasons for this particular choice. The primary consideration was that the double bound-state capture of two electrons from H_2 by an ion has a relatively small cross section which decreases with increasing ion energy and increases with increasing ion charge.[53,54] The ion energy and charge state selected provided an acceptable amount of beam current for the lowest, easily attainable terminal voltage on the accelerator. The second reason for using this specific ion energy and charge state was the possibility of determining the dissociation fraction by a method other than the double capture method. However, this method was found to be too insensitive (see Appendix C).

As mentioned previously, the oven temperature could be measured easily, accurately, and precisely by use of a calibrated optical pyrometer, so measuring $\frac{T}{T^*}$ could be more accurate than the measurement of $Y^*_{q,q-2}(Ar)/Y_{q,q-2}(Ar)$. But, in practice, the average of the values obtained with (B.13) and (B.14) in Appendix B was used in the final determination of the dissociation fraction.

Since the incident ion beam chose for the dissociation fraction measurement was C^{3+}, the double capture method required that the number of C^{1+} ions produced by interaction with the H_2 left in the hot oven be counted. The procedure for doing this was as follows. Beginning with the oven cold, the C^{3+} beam was steered through the entire apparatus and the C^{1+} ions were focused into the ion CEM (see Figure 6, page 42). Fine tuning of the beam and repositioning of collimators and oven was necessary in order to reduce the number of background C^{1+} ions. These background C^{1+} ions were produced by charge exchange with the residual gas in the beamline, as well as charge exchange with the collimator. Next, H_2 gas was flowed into the oven and the C^{1+} ions were collected for a certain amount of charge accumulation in the Faraday cup. A background collection was done immediately afterward which consisted of flowing the same amount of H_2 into the oven chamber without passing through the oven and counting the C^{1+} ions for the same accumulated charge in the Faraday cup. The difference in these numbers was recorded as the number of C^{1+} ions resulting from collisions inside the oven. This procedure was done several times and the results were averaged. The same procedure was repeated several times with argon gas and the results were also averaged. The numbers thus obtained were the values used for $Y_{q,q-2}(H_2)$ and $Y_{q,q-2}(Ar)$ in equations (B.13) and (B.14) of Appendix B. The oven was then heated to some high temperature and the procedure was repeated. The values of $Y^*_{q,q-2}(H_2)$ and $Y^*_{q,q-2}(Ar)$ were thus obtained. The argon gas data was always taken last since a certain amount of time was required to sufficiently pump out the gas handling system and oven vacuum chamber. Double capture yields from small amounts of residual argon could have been as large as the H_2 yields.

Dissociation Fraction Results

The dissociation fraction in the oven was experimentally determined using the double capture method discussed in Appendix B. The average value of the result from equation (B.13) and (B.14) of Appendix B was used to obtain the experimental dissociation fraction for a given temperature and pressure according to the procedures established in the preceding section. Once f was determined, the pressure in the oven was calculated using equations (59) on page 59, and (71) and (72) on page 108

$$P^* = P_1^* + P_2^* = \sqrt{\frac{T^*}{T}}\left[\frac{1+f}{f(\sqrt{2}-1)+1}\right] P_2 = \sqrt{\frac{T^*}{T}}\left[\frac{1+f}{f(\sqrt{2}-1)+1}\right] 0.408\ \Delta P_B . \qquad (77)$$

The values of f and P^* thus determined were then compared to the isothermal curve given by equation (73), page 114

$$f = \sqrt{\frac{K_p(T^*)}{K_p(T^*)+4P^*}} . \qquad (78)$$

The results of dissociation fraction measurements at two different pressures with an oven temperature of 2350 K is shown in Figure 27. The error bars reflect only the statistical uncertainty in the data (see Appendix E) and are therefore somewhat misleading. It was found that charge exchange of the ion beam with the residual gas and with collimators in portions of the beamline was relatively high and this tended to contaminate the beam with

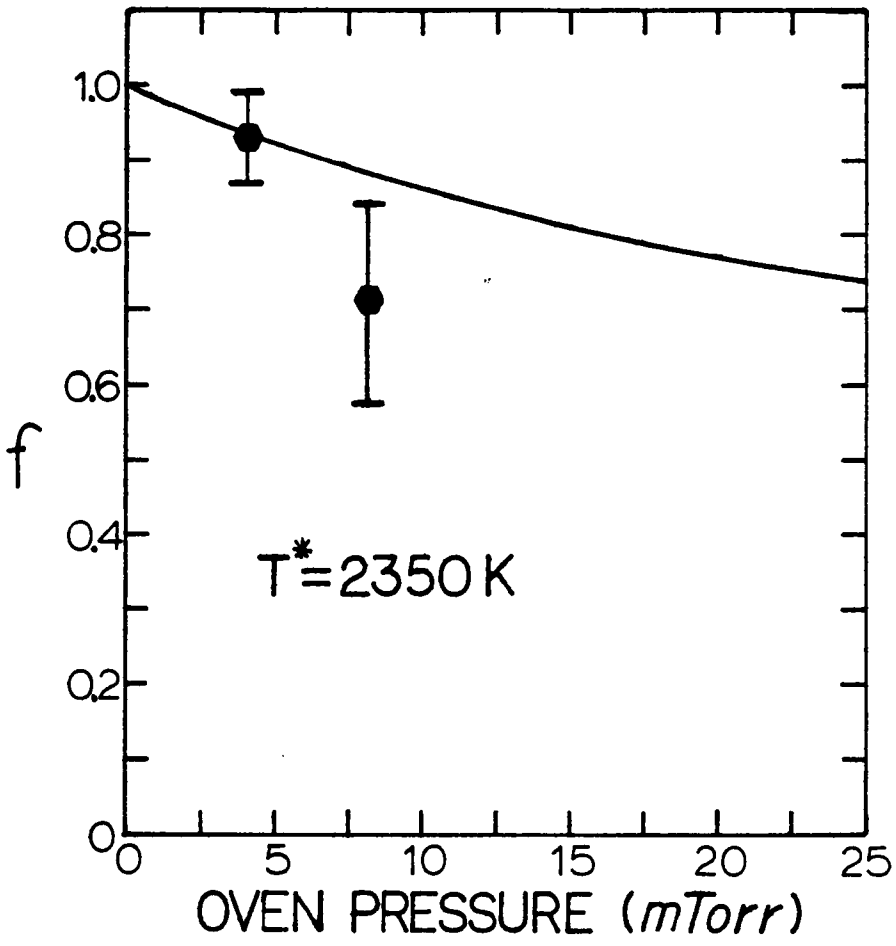

Figure 27. Experimental Dissociation Fraction at 2350K.

The error bars were calculated using the method of Appendix B and are purely statistical. The data points shown are $f = (93 \pm 6)\%$ at $P^* = 4.83$ mTorr and $f = (71 \pm 13)\%$ at $\bar{P}^* = 7.63$ mTorr which were calculated from the average of experimental values using equations (B.13) and (B.14) of Appendix B. The solid line is the curve resulting from equation (73) on page 114. The errors in the pressure are assumed to be $\lesssim 10\%$ (see Chapter V, page 142).

unwanted charge states and a relatively high background for the double capture yield. The double capture yield due to residual gas at a pressure of 10^{-6} Torr throughout the beamline is approximately equal to that with 10 mTorr H_2 in a cold oven. This required that the difference of two large numbers be taken in order to obtain the double capture yield due to interactions in the oven itself. These two numbers were almost equal to one another. The error introduced by this subtraction could be significant, especially if the difference in the two numbers was comparable to this statistical error in either of the two numbers. Possibly the largest single contribution to this contamination was the collimator immediately in front of the oven. Small changes in beam steering could significantly affect the interaction between the beam and collimator and therefore also affect charge exchange. It was found at times that the number of C^{1+} ions produced from double electron by the incident C^{3+} ion could actually show a steady increase independent of the variation of the gas flow into the oven. This indicated that beam steering conditions were changing, probably due to variations in the output voltages of power supplies controlling analyzing magnets and quadrupole magnets positioned before the experimental beamline. Because the probability of double electron capture from H_2 in the oven region was small, the production rate of C^{1+} in the oven was not much larger than the rate with no gas in the oven. Any unknown change in the incident charge state of the beam could adversely affect the number of double capture events.

Significant improvement in the accuracy of the determinations of the dissociation fraction could be realized if either of two modifications were made to the present beamline. The first is the addition of a charge

state cleansing device such as electrostatic steering plates, Wien filter, etc., between the collimator immediately in front of the oven and the oven. This would enable the beam to be purged of unwanted charge states. However, physical limitations in the present system probably make this choice impractical. The other possible change is to use a low energy (50-100 keV) proton beam as the incident ion beam when determining dissociation fractions. The double electron capture by the proton to form H^- is much more probable at these energies and, in fact, the method was originally designed for use with a proton beam of this energy.[27]

For the purpose of the ECC data, it was assumed that thermal and chemical equailibrium conditions existed in the oven and the dissociation fraction was then obtained graphically from Figure 26, page 118. As long as the rate of dissociation is much greater than the gas flow rate into the oven, this assumption should be well justified. Anderson, et al.[55] computed the dissociation rate for molecular hydrogen at a pressure of 15 mTorr and temperature 2100K from the data given in reference 63. The rate of production of atomic hydrogen was $R_H \simeq 6\times10^{18}$ atoms$\cdot$cm$^{-2}\cdot$s^{-1} for a tungsten surface. If the active surface of the oven is assumed to be the inner surface of the 0.4 cm diameter cylindrical hole plus both surfaces of the inner rolled sheet, the total surface area is 3.44 cm^2 and the corresponding rate of production of atomic hydrogen is 2×10^{19} s^{-1}. The flow rate of H_2 into the oven can easily be calculated from the value of ΔP_B and the flow aperture area A using equation (56) on page 59

$$Q = \sqrt{\frac{kT}{2\pi m}}\,\Delta P_B\, A. \qquad (56)$$

Using $A = \frac{\pi(0.1)^2}{4}\ cm^2 = 7.85 \times 10^{-3}\ cm^2$ and inserting other constants, $Q = 46.33\ \Delta P_B\ mTorr \cdot cm^3 \cdot s^{-1}$. With $\Delta P_B = 25$ mTorr, the flow rate of hydrogen atoms (in molecular form) into the oven is found to be

$$Q \simeq 7 \times 10^{16}\ atom \cdot s^{-1}. \tag{79}$$

The rate of production of atomic hydrogen in the oven is

$$R_H \simeq 2 \times 10^{19}\ atom \cdot s^{-1}. \tag{80}$$

Dividing (80) by (79) it is seen that the atomization rate is $\sim$300 times faster than the flow rate into the oven. This indicates that chemical and thermal equilibrium can be reached inside the oven for the temperatures and flow rates considered here.

CHAPTER V

DATA ANALYSIS

The primary goal of this study was to obtain an ECC spectrum for 12 MeV C^{6+} ions incident on atomic hydrogen. This spectrum was used to calculate an experimental value for the differential cross section.

ECC electrons are produced by the interaction of a beam of ions of intensity I_o particles per second which are incident on a target gas of $n \frac{\text{atoms}}{\text{cm}^3}$ and target length ℓ cm. If the cross section for the ECC process is denoted as σ cm^2 and if I is the number of ECC electrons produced per second over a solid angle of 4π steradians, then σ is defined by the equation

$$I = I_o \sigma n \ell, \tag{81}$$

assuming that each particle can undergo only one collision in the target. If all electrons are not being counted, but only those emitted within the solid angle between Ω_e and $\Omega_e + d\Omega_e$ and with energy between E_e and $E_e + dE_e$, then the relation (81) must be written as

$$\frac{dI}{dE_e d\Omega_e} = I_o n \ell \frac{d^2\sigma}{dE_e d\Omega_e}, \tag{82}$$

where $\frac{d^2\sigma}{dE_e d\Omega_d}$ is the differential cross section for the ECC process. In actual experiments, the count rates I and I_o, are integrated over some time interval to give the total number of counts N and N_o, i.e.,

$$\frac{d^2N}{dE_e d\Omega_e} = \int_0^{\Delta t} \frac{d^2I}{dE_e d\Omega_e}\, dt,$$

and

$$N_o = \int_0^{\Delta t} I_o\, dt.$$

The differential cross section is then given by

$$\frac{d^2\sigma}{dE_e d\Omega_e} = \frac{1}{N_o n \ell} \frac{d^2N}{dE_e d\Omega_e} . \tag{83}$$

The differential cross section in equation (83) is given in terms of experimentally obtained quantities N_o, n, ℓ, and $\frac{d^2N}{dE_e d\Omega_e}$ and can, in principle, be determined by simply substituting the values for these quantities. However, the number of ECC electrons collected $\frac{d^2N}{dE_e d\Omega_e}$, must be corrected for several factors which are a result of non-ideal experimental conditions. The spectrometer used to energy analyze the ECC electrons has a finite energy resolution as well as a finite angle of acceptance. This means that the quantity that is really being measured by the spectrometer is the convolution of $\frac{d^2N}{dE_e d\Omega_e}$ with the spectrometer transmission function $T(E_e - E_{e_o})$. In general, $T(E_e - E_{e_o})$ is energy dependent. Another factor $\varepsilon(E_e)$, due to the change in the direction efficiency of the electron CEM as a function of energy, is also required. This convolution is then integrated over the solid angle of acceptance $\Omega_e(\theta_o)$, and energy resolution width ΔE_e. The number of electrons which actually get transmitted through the analyzer and detected by the CEM for

an electron with energy E_{e_o} is therefore given by

$$N(E_{e_o}) = N_o n\ell \int_{\Delta E_e} \int_{\Delta\Omega_e(\Theta_o)} \frac{d^2N}{dE_e d\Omega_e} T(E_e - E_{e_o}) \varepsilon(E_e) dE_e d\Omega_e . \qquad (84)$$

where Θ_o is the angular acceptance of the analyzer and is determined by the angle defining aperture in Figure 10 on page 70. Using equation (83) in (84) gives,

$$N(E_{e_o}) = N_o n\ell \int_{\Delta E_e} \int_{\Delta\Omega_e(\Theta_o)} \frac{d^2\sigma}{dE_e d_e} T(E - E_{e_o}) \varepsilon(E_e) dE_e d\Omega_e . \qquad (85)$$

Since $T(E_e - E_{e_o})$ is essentially independent of entrance angle for the small angles allowed in this study,[50] the integrations in equation (85) can be written as

$$N(E_{e_o}) \simeq N_o n\ell \int_{\Delta E_e} T(E_e - E_{e_o}) \varepsilon(E_e) \int_{\Delta\Omega_e(\Theta_o)} \frac{d^2T}{dE_e d\Omega_e} d\Omega_e dE_e . \qquad (86)$$

The angular integration gives

$$\int_{\Delta\Omega_e(\Theta_o)} \frac{d^2\sigma}{dE_e d\Omega_e} d\Omega_e \simeq \frac{d^2\sigma}{dE_e d\Omega_e} \Bigg|_{\Theta_o} \Delta\Omega_e(\Theta_o) . \qquad (87)$$

This integration removes the discontinuity in $\frac{d^2\sigma}{dE_e d\Omega_e}$ at $\Theta_e = 0^o$,[12,21] and

since the cross section $\left.\frac{d^2\sigma}{dE_e d\Omega_e}\right|_{\theta_o}$, is essentially constant over the small energy interval considered in equation (86) this term may be removed from the energy integral giving

$$N(E_{e_o}) \simeq N_o n\ell\, \Delta\Omega_e(\theta_o) \left.\frac{d^2\sigma}{dE_e d\Omega_e}\right|_{\theta_o} \int_{\Delta E_e} T(E_e - E_{e_o})\varepsilon(E_e) \tag{88}$$

The transmission function of the analyzer is very nearly triangular, as seen in Figure 15, page 75, so that the integral of the function $T(E_e - E_{e_o})\varepsilon(E_e)$, over the energy range E_{e_o} to $E_{e_o} \pm \Delta E_{e_o}$, where ΔE_{e_o} is the FWHM of the transmission function is given by,

$$\int_{E_{e_o} - \Delta E_{e_o}}^{E_{e_o} + \Delta E_{e_o}} \varepsilon(E_e) T(E_e - E_{e_o})\, dE_e = \tfrac{1}{2}(2\Delta E_{e_o})\varepsilon(E_{e_o}) = \beta E_{e_o}\varepsilon(E_{e_o}), \tag{89}$$

where β is the analyzer energy resolution. Equation (88) can now be written as

$$N(E_{e_o}) = N_o n\ell\beta E_{e_o}\, \varepsilon(E_{e_o})\Delta\Omega_e(\theta_o) \left.\frac{d^2\sigma}{dE_e d\Omega_e}\right|_{\theta_o}. \tag{90}$$

As discussed in Chapter III, the energy spectrum of ECC electrons was scanned by dividing the spectrum into 256 channels. The time spent in each channel was determined by the charge collected in the Faraday cup at the end of the beamline, i.e., N_o. Equation (90) can be applied to the j^{th} channel, centered on energy E_{e_j}, by writing the counts in the j^{th}

channel as

$$N_j(E_{e_j}) = N_o n\ell\beta E_{e_j} \varepsilon\Delta\Omega_e(\theta_o) \left.\frac{d^2\sigma}{dE_e d\Omega_e}\right|_{\theta_o} , \qquad (91)$$

where it has been assumed that the detection efficiency ε, of the CEM is constant over the energy range of the spectrum.[50] Using equation (91), the channels in k scans can be summed to give the differential cross section integrated from energy E_1 to energy E_2, corresponding to channels j_i and j_2, respectively,

$$\int_{E_1}^{E_2} \left.\frac{d^2\sigma}{dE_e d\Omega_e}\right|_{\theta_o} dE_e \simeq \frac{1}{n\ell\beta\varepsilon\Delta\Omega_e(\theta_o)} \sum_{i=1}^{k} \frac{1}{N_{o_i}} \sum_{j=j_1}^{j_2} \frac{N_{ij}(E_{e_j})}{E_{e_j}} . \qquad (92)$$

Since the Faraday cup collects the total charge incident, then this total charge C_o, must be divided by the charge per ion to give N_o, i.e., for the C^{6+} ion used in this study

$$N_o = \frac{C_o}{6e} , \qquad (93)$$

where $e = 1.6\text{x}10^{-19}$ Coulomb. Rewriting equation (92),

$$\int_{E_1}^{E_2} \left.\frac{d^2\sigma}{dE_e d\Omega_e}\right|_{\theta_o} dE_e \simeq \frac{6e}{n\ell\beta\varepsilon\Delta\Omega_e(\theta_o)} \sum_{i=1}^{k} \frac{1}{Co_i} \sum_{j=j_1}^{j_2} \frac{N_{ij}(E_{e_j})}{E_{e_j}} . \qquad (94)$$

Equation (94) provides a means by which experimental data can be converted into a quantitative estimate for the ECC differential cross section. The

values of C_{o_i}, $N_{ij}(E_{e_j})$, ε, and $\Delta\Omega(\theta_o)$ can be obtained either by direct measurement or, in the case of ε, from previously published data. Estimates of the gas density n, and target thickness ℓ, must be obtained by more indirect means. Before examining these, however, some discussion is necessary on the nature of the backgrounds encountered when performing an ECC experiment.

Subtracting Background From ECC Spectrum

As seen from Figure 2, page 7, the number of electrons for velocities (or energies) relatively far away from the peak velocity (or energy) does not seem to approach zero, i.e., the cusp seems to be superimposed on an underlying background. As mentioned in Chapter II on page 12, the total integrated cross section includes not only ECC electrons, but also electrons produced from direct ionization. When obtaining the total cross section, the contribution due to the ECC process is relatively small and, therefore, even if the ECC process is neglected, calculations of total cross sections produce good agreement with experimental data. But when calculating differential cross sections for electrons with laboratory velocities close to that of the incident ion velocity, only by including the ECC process can even fair agreement with experiment be obtained.[2,12,21,26] The contribution due to direct ionization and ECC can be separated when calculating theoretical values by choosing the final state wavefunction which best describes the process under consideration.[3,12] Experimental apparatus, on the other hand, cannot distinguish between electrons produced by ECC and those produced by direct ionization, despite the fact that relatively high electron velocities are being studied. Although the greatest percentage of

directly ionized electrons will have velocities much less than the ion velocity, a finite number will have velocities close to that of the ion. These electrons are physically indistinguishable from ECC electrons, even in principle.[3,12] Subtracting a background presumably attributable to direct ionization from the experimental ECC cusp would therefore be arbitrary and incorrect. This would be true even if the background was calculated theoretically from wavefunctions appropriate to the direct ionization process. Spurious background signals however, such as those due to scattering from collimators or from heating the oven, as mentioned in Chapters III and IV, could be realistically subtracted from the experimental cusp data since these signals originate from independent physical processes. The methods used to account for these spurious backgrounds are explained in Chapters III and IV.

Figure 28 shows the ECC cusp obtained for 12 MeV C^{6+} incident on $H+H_2$ in the hot oven, along with the corresponding background with gas flowing into vacuum chamber without passing through oven. The background from all other sources was found to be $\sim$10% of the background due to the hot oven and oven heating electron gun. Chapters III and IV discuss the background contribution of various parts of the experimental system. The average background per channel was then subtracted from the "raw" cusp data of Figure 28 to give the background corrected cusp shown in Figure 29. As seen in Figure 29, the data appears to be rather scattered; nevertheless, the asymmetry of the ECC cusp is clearly evident. The spectra in both Figures 28 and 29 are 64 channel spectra that were produced by straightforward four-channel averaging of the original 256 channel spectra, i.e., four adjacent channels in each of the original spectra

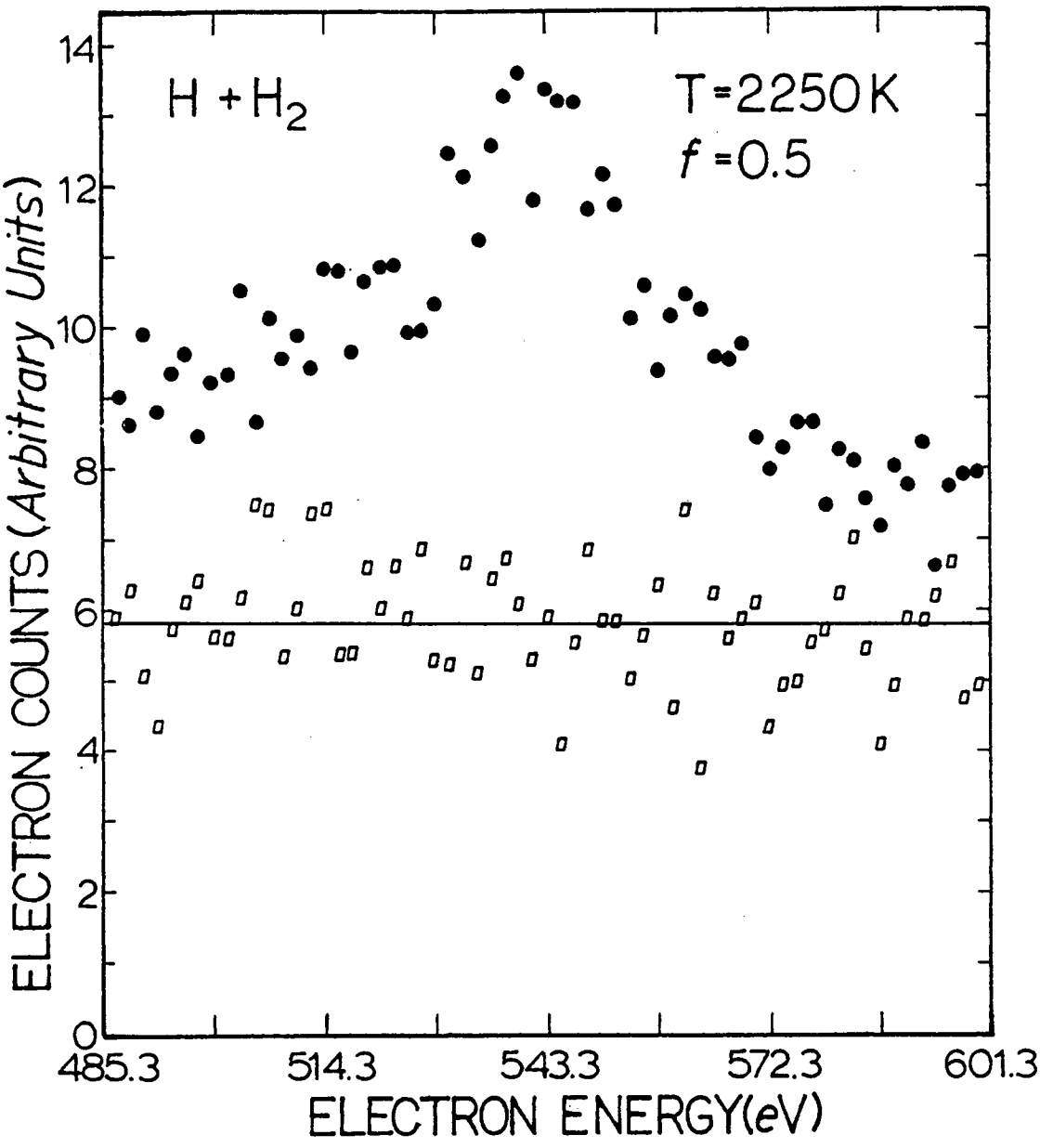

Figure 28. ECC Cusp and Background From Mixture of H and H_2 in Hot Oven.

The background (□) due to heating the oven is seen below the cusp (•). This background is flat and easily discernible from the ECC cusp. It was obtained by flowing gas into vacuum chamber without passing through oven. The solid line is the average of the background data.

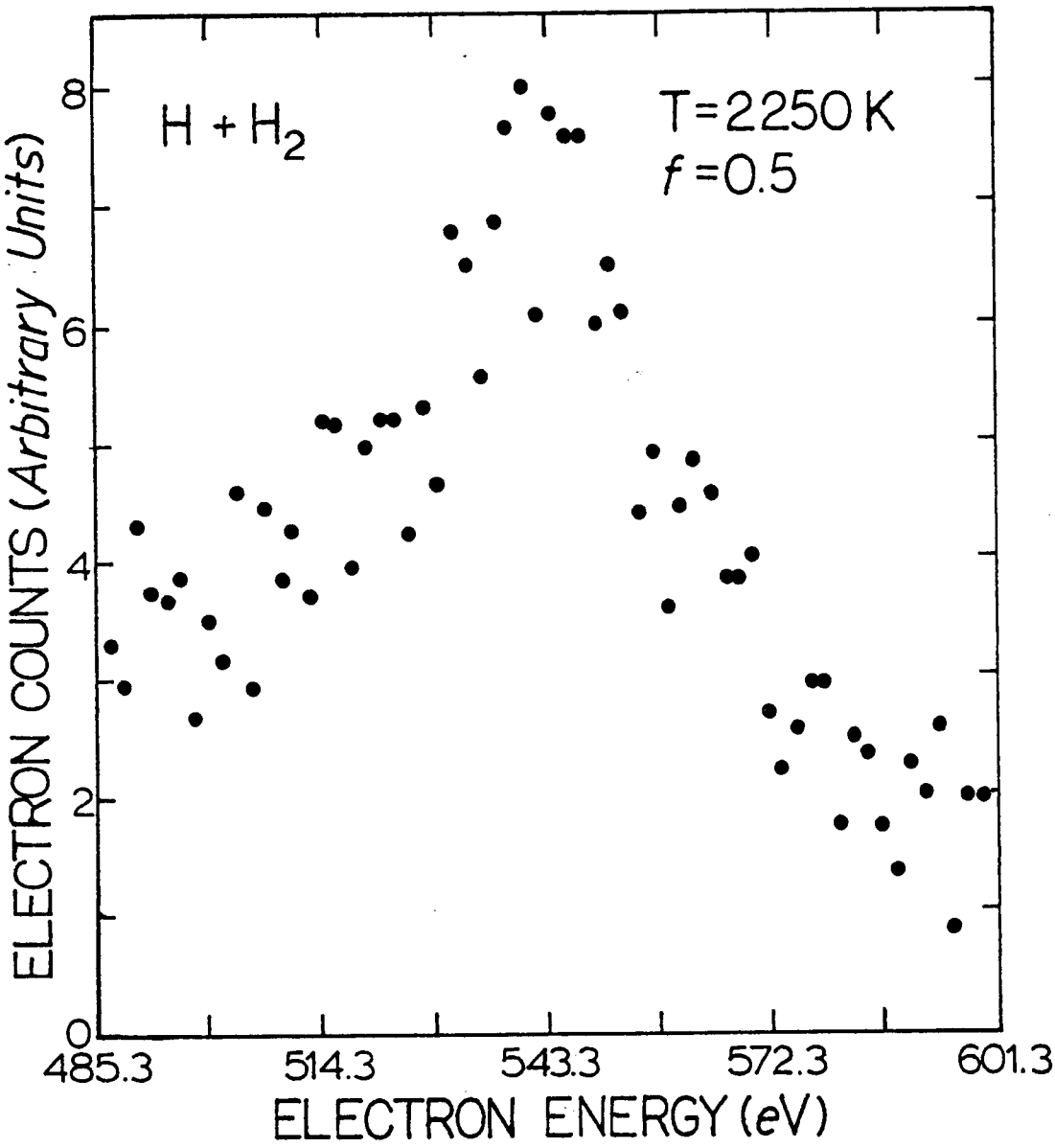

Figure 29. Background Subtracted ECC Cusp From Mixture of H and H_2.

The average background per channel obtained from the background shown in Figure 28 was subtracted from each channel of the ECC cusp in Figure 28 to give this corrected cusp.

were added and the result placed in the channel corresponding to the energy which was the average of the energies in the four channels. This process was continued through each spectrum and resulted in 64 channel spectra with energy resolutions four times worse than the 256 channel spectra but with better counting statistics in each channel. Note that the summing of adjacent channels was not a moving average but corresponded to a compression of each spectrum from 256 channels to 64 channels.

The value of the dissociation fraction f given in Figures 28 and 29 was determined graphically from Figure 26 on page 118, as discussed in Chapter IV. The value f=0.5, is lower than the values obtained when the dissociation fraction of the oven was measured (see Figure 27, page 122). This difference is a consequence of two experimental procedures: 1) When the ECC data was being acquired the oven temperature was 2250K, while the dissociation fraction measurements were made at 2350K. 2) The flow rate of H_2 into the oven during ECC measurements was set so that ΔP_B = 25 mTorr, but during the dissociation fraction measurements the flow rate corresponded to $\Delta P_B \leq 5$ mTorr Although it was known that the dissociation value would be reduced, these two procedures were considered necessary for the following reasons. Lowering the temperature of the oven extended the useful lifetime of certain parts of the oven (see Chapter IV). This allowed longer uninterrupted data acquisition periods since experimental availability of the ORNL EN Tandem Accelerator facilities were limited. Also, for high dissociation fraction even at relatively high temperatures, the pressure in the oven was required to be low (see Figure 27, page 122). Because the background count rate was relatively large, it was necessary that precise oven positioning

adjustments, collimator alignment, etc. be made periodically to maintain the prerequisite small background. Direct effects of these adjustments could be observed only with higher pressures in the oven. It is believed that the corrections employed to account for the additional amount of H_2 in the hot oven adequately compensated for the use of higher pressure and lower temperature. These corrections are discussed in the remainder of the chapter.

Calibrating Gas Flow

It was fairly certain that the gas pressure in the oven could be determined by applying the gas flow equations in Chapter III, nevertheless, a check was performed to calibrate the gas flow system. The pressure P_2, of H_2 in the cold oven is given by equation (59) on page 59,

$$P_2 = 0.408\ \Delta P_B\ \text{mTorr}, \tag{59}$$

where ΔP_B is the pressure difference across the flow aperture as measured by the capacitance manometer. If a C^{3+} ion beam is incident on the H_2 gas in the cold oven at pressure P_2, target length ℓ cm, and absolute temperature T, and if the number of C^{1+} ions produced per incident C^{3+} ion is $N_{3,1}(H_2)$, then P_2 is given by,

$$P_2 = \frac{kT}{\sigma_{3,1}(H_2)\ell}\, N_{3,1}(H_2), \tag{95}$$

where $\sigma_{3,1}(H_2)$ is the cross section for the double electron capture process. There were no tabulated values of $\sigma_{3,1}(H_2)$ available but this quantity was obtained by first writing the ratio of the double electron capture cross section to that of the single electron loss cross section,

$$\frac{\sigma_{3,1}(H_2)}{\sigma_{3,4}(H_2)} = \frac{N_{3,1}(H_2)}{N_{3,4}(H_2)} \tag{96}$$

where equation (95) has been applied for each process, assuming that P_2, ℓ, and T are held constant. The ratio on the right hand side of (96) was measured using a 1.38 MeV C^{3+} incident ion beam and the value of $\sigma_{3,4}(H_2)$ obtained by Goffe, et al.[65] was inserted to give

$$\sigma_{3,1}(H_2) = 6.44 \times 10^{-18} \text{ cm}^2. \tag{97}$$

This value for $\sigma_{3.1}(H_2)$ was used to obtain the pressure of H_2 in the cold oven by inserting into (95). The length ℓ, of the gas target was assumed to be equal to the length ℓ_{oven}, of the oven itself plus 10% to account for plume effects at the holes in the oven. So,

$$\ell = \ell_{oven} + 0.10\ \ell_{oven}. \tag{98}$$

The additive correcting in equation (98) was determined by means of an independent study (see page 142). The flow of gas into the oven was controlled by setting the value of ΔP_B. Table V shows the pressure in the cold oven calculated from equation (59) denoted as P_{2_F}, compared with the pressure determined using equations (95) through (97), denoted as P_{2_σ}. The calibration pressures ΔP_B, were chosen to correspond to those values used in the dissociation fraction measurement. There is sufficient agreement between the two independent measurements of the pressure to believe that either method of determining the pressure should be valid. This validity is further supported by the data of Figure 30 which shows that the number of ECC electrons increases linearly as the gas flow into

TABLE V

CALIBRATION OF PRESSURE IN THE OVEN

ΔP_B(mTorr)	P_{2_F} (mTorr)	P_{2_σ} (mTorr)	$\frac{(P_{2_\sigma} - P_{2_F})}{(P_{2_\sigma} + P_{2_F})} \times 100\%$	$\frac{(P_{2_\sigma} - P_{2_F})}{P_{2_\sigma}} \times 100\%$
3	1.22	1.32	4%	7.6%
5	2.04	2.25	5%	9.3%

$P_{2_F} \equiv H_2$ pressure calculated from equation (59) on page 59.

$P_{2_\sigma} \equiv H_2$ pressure calculated from equations (95) through (98).

the oven is increased. This indicates that single collision conditions exist for a wide range of flow rates, and since the pressure calibration was shown in Table V to be accurate within 10% for lower pressures, this calibration should remain valid also for the higher pressures indicated in Figure 30.

Calibrating the pressure in the oven for two low pressures and showing that the electron counts increase linearly with increasing flow rate are both necessary conditions to indicate that there is a negligible flow rate of gas through leaks in the various fittings in the oven. The magnitude of these leaks was calculated to be negligible by applying gas flow equations[47] to the various leaks in the fittings of the oven parts. Calculations showed that these leaks were negligible and the results of calibrating the pressure in the oven have served to support this contention. However, there still existed the possibility that heating the oven would

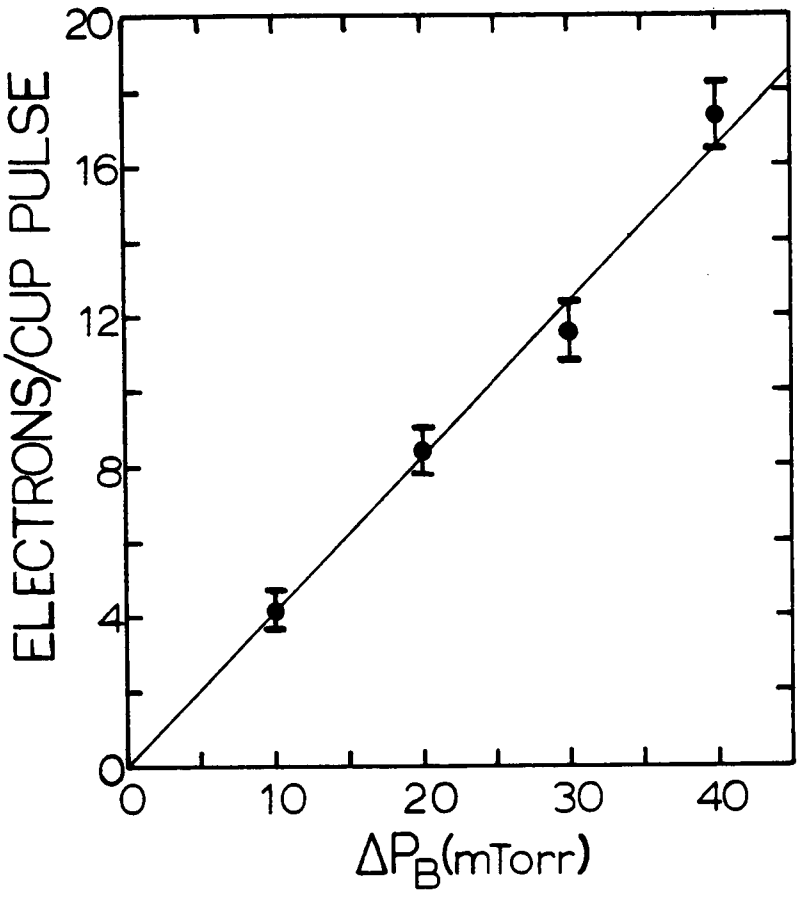

Figure 30. ECC Electrons Versus Gas Flow Into Oven.

The linear increase in the electron count rate with increasing gas flow $Q \alpha \Delta P_B$ (see equation 56, on page 59) indicates that single collision conditions exist inside the oven for a wide range of pressures.

cause the negligible size leaks to become significant, either by enlarging of actual leaks in the oven fittings or by allowing diffusion of gas through hot tungsten surfaces.

A comparison was made between the number of ECC electrons produced per incident ion N(Ar), with an argon gas target for a given ΔP_B with the oven cold and hot. The ratio of these numbers should be given by equation (B.12) of Appendix B, i.e.,

$$\frac{\pi^*(Ar)}{\pi(Ar)} = \frac{N^*(Ar)}{N(Ar)} = \sqrt{\frac{T}{T^*}}, \qquad (B.12)$$

where * denotes a hot oven and $\pi=n\ell$. The thermal transpiration curve obtained from the rightmost side of equation (B.12) is shown in Figure 31. The value obtained for $\frac{N^*(Ar)}{N(Ar)}$ with T = 293K and T^* = 2200K is also shown in the figure. This experimental value is within 6% of the predicted value, a fact which indicates that there was essentially no argon gas passing through physical leaks in the oven fittings. The argon would not be expected to diffuse effectively through the rather thick hot tungsten surfaces, but this diffusion could possibly occur with H_2.

If H_2 gas was diffusing through the hot tungsten, the actual amount of H_2 entering the oven would be less than the supposed quantity. This would tend to lower the probability that an ion passing through the hot oven would capture two electrons. The result would be a systemmatic increase in the experimental dissociation fraction since the value of $\frac{Y^*_{3,1}(H_2)}{Y_{3,1}(H_2)}$ in equations (B.13) and (B.14) of Appendix B would be artificially small. However, the experimentally determined dissociation fractions are not higher than expected but, to the contrary, the data for ΔP_B = 5 mTorr in Figure 27 on page 122 actually appears slightly smaller than the predicted value, indicating that no H_2 gas was diffusing through the hot tungsten. The error associated with the determination of the absolute pressure in the oven, either hot or cold, will therefore be taken to be 10%. This error corresponds to an uncertainty in pressure of about the width of the data points in Figure 27 on page 122.

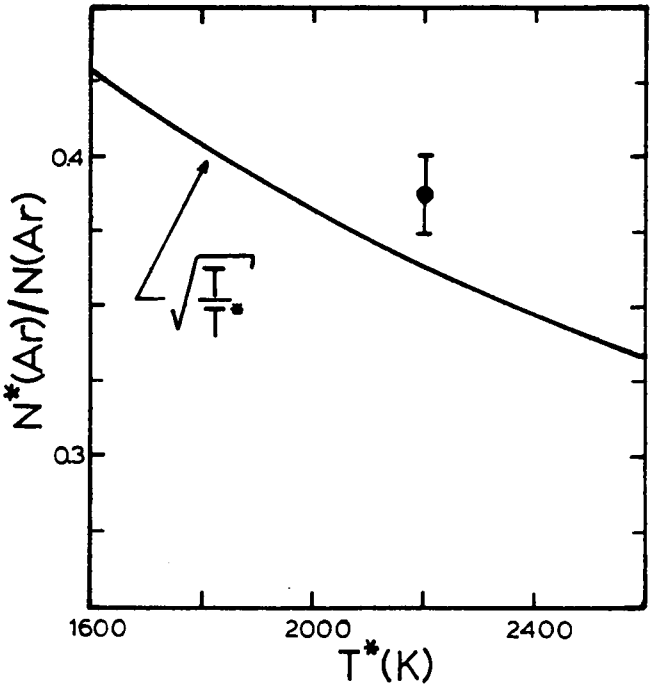

Figure 31. Thermal Transpiration Curve for Argon.

The data point was taken at $T^* = 2200K$ and is within 6% of the theoretical value (—) plotted from equation (B.12) on page 140.

Estimates of Errors Associated With the ECC Cross Section

Every quantity used in equation (94) had some inherent error associated with it, either due to counting statistics or instrumental uncertainties. Within a fair degree of accuracy, the quantities ε, β, $\Delta\Omega(\theta_o)$, and $\frac{N(E_{e_j})}{E_{e_j}}$ are independent of one another, so that the errors associated with each are also independent. The determinations of the number density n, and the length ℓ, of the interaction region are not

strictly independent, however, since the accurate experimental determination of n usually assumes a knowledge of ℓ, and vice versa. The study resulting in equation (98) measured the effect of the gas plumes exiting the oven apertures. A double-walled gas cell was used in place of the oven to create the two plumes without allowing gas to enter the interaction region itself. The number of ECC electrons produced in these plumes was then compared to the number of ECC electrons produced when gas was flowed directly into the interaction region. This plume effect was found to be $\lesssim$10%, hence the additive correction to the gas cell length in equation (98). The error associated with n is the same as the error associated with the pressure measurements of Table V. The resultant error of the product $n\ell$ will, therefore, assume to be the error in n as long as ℓ is given by equation (98). The values of n^*, n_1^*, and n_2^* for a hot oven are obtained directly from the plot in Figure 23 on page 110. The error in the number densities was therefore dependent on the error in the dissociation fraction f, which was believed to be less than 10% (see Figure 27, page 122). The error associated with ε was assumed to be the same as that quoted in Reference 50, while the error in β was 8%, as shown in Figure 13 on page 73. The value of $\Delta\Omega(\Theta_o)$ was determined by

$$\Delta\Omega(\Theta_o) = 2\pi \int_0^{\Theta_o} \sin\Theta d\Theta = 2\pi(1-\cos\Theta_o), \tag{99}$$

where Θ_o is the angular acceptance and was obtained from direct measurement of aperture sizes, etc. This error was believed to be less than

3%. The errors associated with C_{o_i} and E_{e_j} in equation (94) on page 130 were assumed to be negligible.

One final quantity $\frac{N_{ij}(E_{e_j})}{E_{e_j}}$, from equation (94) remains to be considered. It will be assumed that $\frac{N_{ik}(E_{e_k})}{E_{e_k}}$ is independent of $\frac{N_{ij\neq k}(E_{e_{j\neq k}})}{E_{e_{j\neq k}}}$, or at least that the dependence is accounted for by the factor $1/\beta$ in front of the summation. If the terms in the summation are independent, then the statistical error σ_Σ, associated with the sum is,

$$\sigma_\Sigma = \left[\sum_{i=i}^{k} \sum_{j=j,}^{j_2} \frac{N_{ij}(E_{e_j})}{E_{e_j}} \right]^{\frac{1}{2}}. \qquad (100)$$

Denoting the errors in $n\ell$, β, ε, and $\Delta\Omega(\theta_o)$ by $\sigma_{n\ell}$, σ_β, σ_ε, and σ_Ω, respectively, the total percentage error associated with the determination of equation (94) can be written as,[56]

$$\sigma_{Tot} = \left[(\sigma_D)^2 + \frac{1}{\sigma_\Sigma} \right]^{\frac{1}{2}} \times 100\%, \qquad (101)$$

where $\sigma_D^2 \equiv \left(\frac{\sigma n\ell}{n\ell}\right)^2 + \left(\frac{\sigma_\varepsilon}{\varepsilon}\right)^2 + \left(\frac{\sigma_\beta}{\beta}\right)^2 + \left(\frac{\sigma_\Omega}{\Delta\Omega(\theta_o)}\right)^2$. Table VI summarizes the errors associated with σ_D.

Spectral Shape Analysis

The differential cross section can be written according to equation (37) on page 26 as

$$\frac{d^2\sigma}{dE_e d\Omega_e} \alpha \left| T_{if} \right|^2,$$

where T_{if} is the transition matrix defined by equation (26) on page 18. T_{if} can be expanding in a power series in v', where v' is the

TABLE VI

ERRORS ASSOCIATED WITH CROSS SECTION

$\frac{\sigma_\varepsilon}{\varepsilon}$ @ 300 eV[50]	$\leq$14%
$\frac{\sigma_\beta}{\beta}$	8%
$\frac{\sigma_\Omega}{\Delta\Omega(\Theta_o)}$	3%
$\frac{\sigma_{n\ell}}{n\ell}$	10%
σ_D	19%

electron-ion velocity difference.[56] The coefficients of the v' terms in the expansion are then expanded in a Legendre polynomial series $P(\cos\Theta')$, to introduce the angular dependence of T_{if}, where Θ' is the angle between the incident ion velocity vector $\bar{v}_p$, and the vector $\bar{v}'$. The final result for the differential cross section is,

$$\frac{d\sigma}{d\bar{v}} = \frac{1}{v'} \sum_{n,j} v'^{n} P_j(\cos\Theta') B_j^{(n)}(v_p), \qquad (102)$$

where $\bar{v} \equiv$ velocity of electron in laboratory frame and $B_j^{(n)}(v_p)$ is a term including the momentum transfer between the electron and the incident ion. The measured velocity distribution of ECC electrons is given by

$$Q(v,\Theta) = \int_v \int_\Omega S(v,\Omega) v^2 \frac{d\sigma}{d\bar{v}} \, dv d\Omega, \tag{103}$$

where Ω is the solid angle of collection by the apparatus and $S(v,\Omega) = T(v)G(\Theta)$ is the transmission function of the analyzer which is separable into velocity $T(v)$, and angular $G(\Theta)$, functions. By inserting (102) in (103), an expression can be obtained relating the coefficients of the cross section expansion with the measured electron distribution.[57]

Since the electrostatic analyzer used in this study was an energy analyzer, the measured distribution was an energy distribution rather than the velocity distribution in equation (103). A least squares procedure was adapted for use with this energy spectrum by S. D. Berry.[59] The resulting energy distribution is given by

$$Q(E,\Theta) = \int_E \int_\Omega S'(E,\Omega) \frac{d^2\sigma}{dE d\Omega} \, dE d\Omega, \tag{104}$$

where $\frac{d^2\sigma}{dE d\Omega} = \frac{v}{m} \frac{d\sigma}{d\bar{v}}$. The least squares fit[58,59] employed a gradient search method[56] to fit the measured spectra to the functional form in equation (104).

CHAPTER VI

RESULTS AND CONCLUSION

As seen from Figure 29 on page 134, the scatter in the data precludes any comprehensive study of the cusp shape; however, a procedure was devised by which some general cusp shape information could be obtained. In order to account for the nondissociated H_2 left in the oven, a spectrum with H_2 in a cold oven was obtained. The number density of H_2 in the hot oven for a given dissociation fraction f, and oven temperature T^*, can be obtained from Figure 23 on page 110. The cold H_2 spectrum was then normalized to this number density. The least squares fit to the normalized cold H_2 data was subtracted from the least squares fit to the hot H, H_2 mixture. The resultant "derived" fit was attributable to atomic hydrogen.

Figure 32 shows the data spectrum for cold H_2 along with the computer generated least squares fit to the data. The data obtained for the hot mixture of H and H_2 (see Figure 29, page 134) and the curve resulting from the least squares fit to that data are displayed in Figure 33.

Figure 34 shows the data attributable to atomic hydrogen along with the fitted curve derived from the difference between the fit to the hot mixture in Figure 29 and the normalized fit to the cold H_2 data in Figure 32. The data points were obtained by subtracting the normalized H_2 fit from the hot mixture data.

Calibration of System for Absolute Cross Sections

When calculating the cross section according to equation (94) on page 130, there is a factor $n\ell\Delta\Omega(\Theta_o)$, appearing in the denominator,

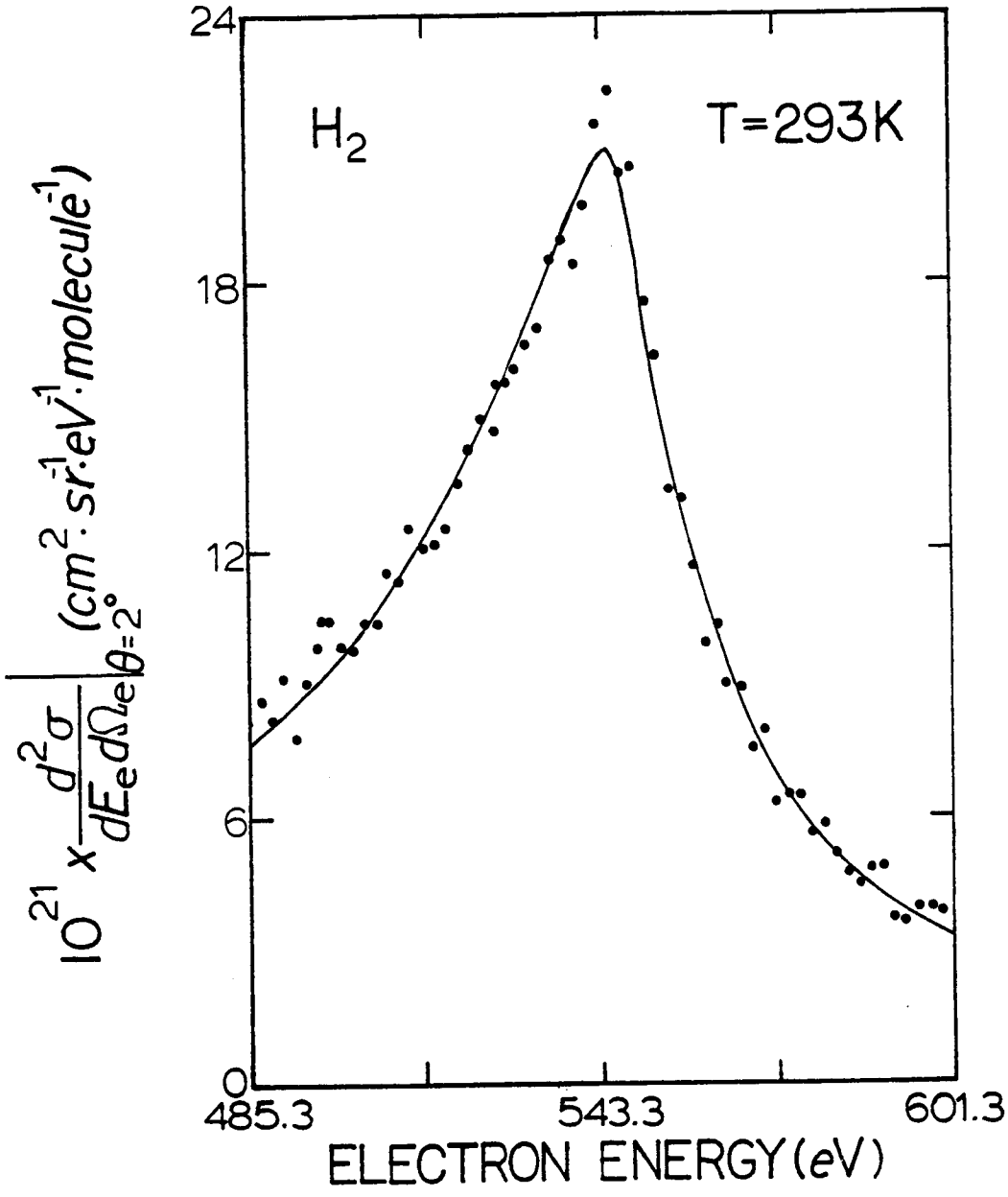

Figure 32. ECC Spectrum for 12 MeV C^{6+} Incident on H_2. Solid line is a least squares fit using equation (104).

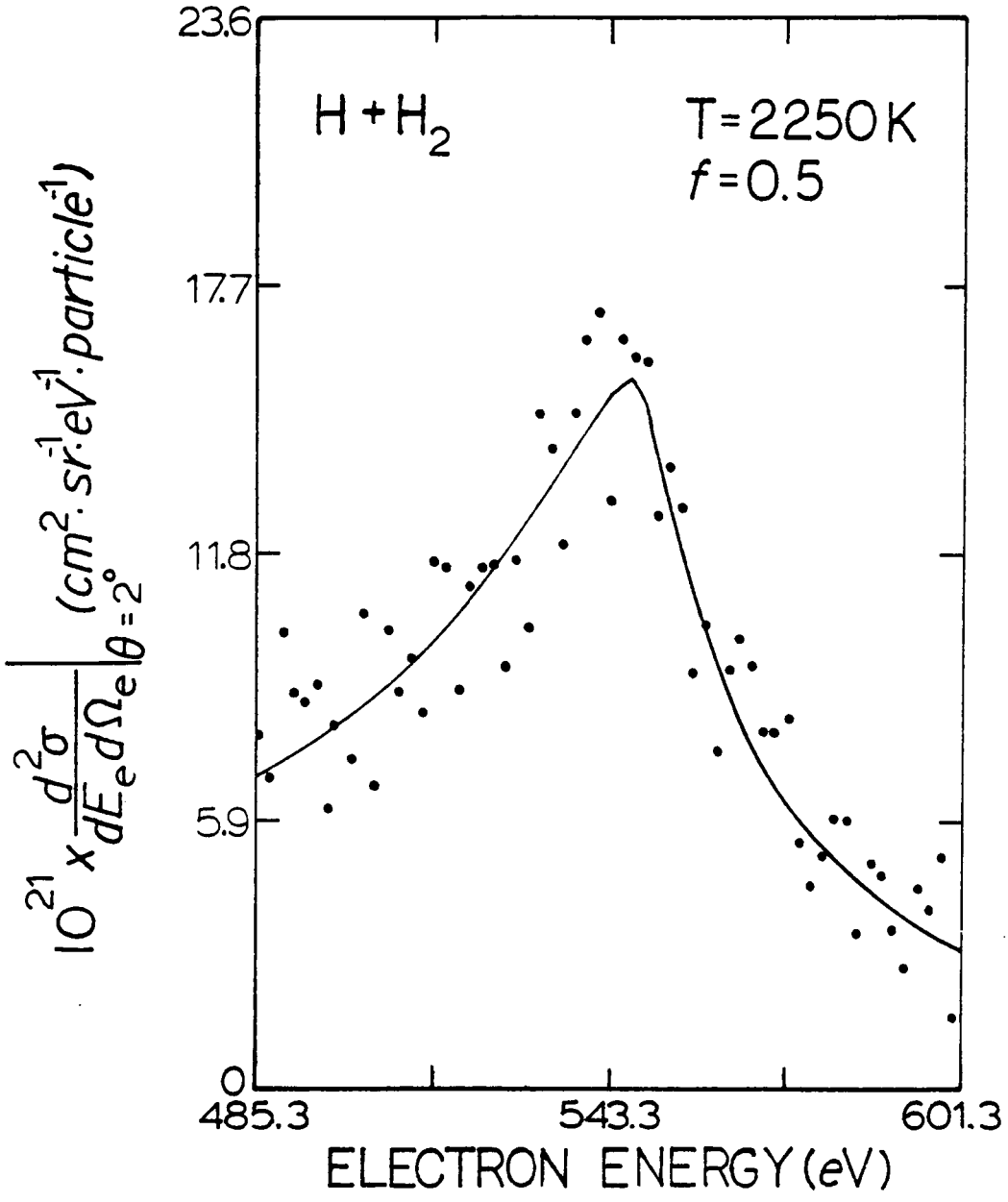

Figure 33. ECC Spectrum for 12 MeV C^{6+} Incident on the Hot H, H_2 mixture.

The data points result from the subtraction of the average background per channel from each channel. The solid line is least squares fit to the data using equation (104).

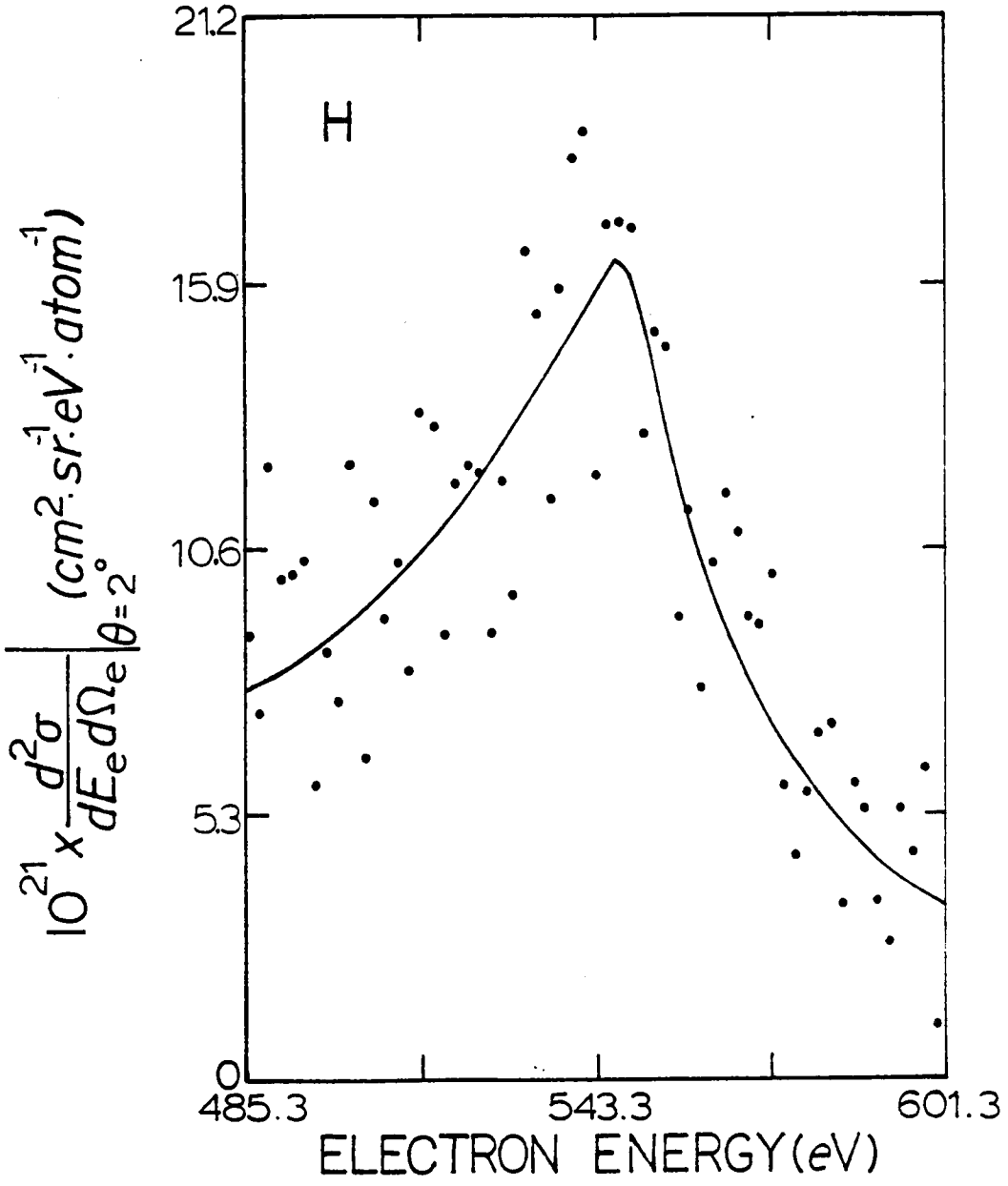

Figure 34. ECC Spectrum on Atomic Hydrogen.

Data is difference between data in Figure 29 and the normalized fit in Figure 32. Solid line is the difference between the fit in Figure 33 and the normalized fit in Figure 32.

where n is the number density (particles/cm^3) inside the oven, ℓ is the effective target lenght of the oven and $\Delta\Omega(\Theta_o)$ is the solid angle of acceptance of the electron spectrometer. The term n was shown to be accurately obtainable either by application of the gas flow relation given by equation (59) on page 59 along with p=nkT, or from direct experimental measurements as shown by the data in Table V on page 138 along with Figure 30 on page 139. By using the thermal transpiration curve of Figure 31 on page 141 and the discussion on pages 138-140, it was also shown that the value of n obtained in this way was valid when the oven was hot.

The length of the interaction region ℓ, was determined according to equation (98) on page 137. The results in Table V on page 138 show that equation (98) accurately represents the length of the interaction region. The final factor $\Delta\Omega(\Theta_o)$, determined from equation (99) on page 142, is strictly valid only for very thin targets, i.e., for very small ℓ.

As discussed on pages 136-138, the determination of the number density n, inside the oven was performed by using an ion beam passing through the oven. The procedure discussed on pages 136-138 could be used to determine the average value of n throughout the region of length ℓ, where ℓ was given by equation (98) on page 138. The determinations of both n and ℓ did not require the use of the electron spectrometer. As a result, the acceptance angle did not enter into any of the experimentally determined values. This is shown explicitly in equation (95) on page 136.

However, when determining ECC cross sections, the acceptance angle of the spectrometer was necessarily included, as shown in equations (84)

through (94) on pages 128-130. The focal point of the spectrometer was located approximately at the exit aperture of the oven as shown in Figure 17 on page 85. Because of the length of the oven there was no easily calculable value which could be used for $\Delta\Omega(\theta_o)$. The angle defining aperture shown in Figure 10 on page 70 actually defines the angular acceptance of the spectrometer only for those electrons produced in the focal plane of the analyzer. The ECC electrons produced at points inside the oven which are not in the analyzer focal plane will not be counted with the same efficiency as those produced in the focal plane. In principle, this effect can be accounted for by calculating the effective experimental value for the product $n\ell\Delta\Omega(\theta_o)$. This calculation can be written as[66]

$$\left[\underline{n}\ell\Delta\underline{\Omega}\right]_{\text{effective}} = \int_{\substack{\text{volume}\\ \text{of interaction}\\ \text{region}}} n(X,\Omega)\,dx d\Omega, \qquad (105)$$

where x represents the position inside the interaction region. This integral is sensitively dependent upon relative beam size, defining apertures, plume effects of gas outstreaming from the oven apertures, as well as other experimental factors. Analytical evaluation of the integral is very difficult under most circumstances. In most cases, the desired result can be obtained much easier by direct experimental determination.

By comparing ECC cross sections obtained with the present experimental configuration for a specific target gas to that of an absolute cross section measurement determined by an independent study for the

same target gas, the calibration of the present system can be obtained. This calibration would then be valid for a wide range of target gases and incident ion energies. This is, in effect, an experimental determination of the integral in equation (105).

Argon gas was used as the target for the purposes of the calibration since it was readily available. The data of C. R. Vane[2] was the only absolute cross section data easily available. For argon gas targets, however, the lowest energy for which absolute cross sections had been measured by Vane was 1.88 MeV/u for C^{6+} ions. The ORNL EN Tandem could not reach energies this high due to mechanical problems. It was decided to calibrate the present data collection system by extrapolating Vane's data to lower energies. Figure 35 shows that the logarithm of the cross section varies linearly with the incident ion velocity. A straight line extrapolation can be easily performed. Also, Vane's data showed that target shell effects should be small, at least over the region through which the extrapolation was to be performed. Since Vane's results also agreed with those of Rødbro and Anderson[16] it was therefore believed that the extrapolation of Vane's results was sufficiently valid.

By extrapolating the data points in Figure 35 a cross section of $(4.75\pm1.66)\times10^{-17}$ cm^2/sr was obtained for 1 MeV/u C^{6+} incident on argon. The value obtained with the present apparatus was $(4\pm1.7)\times10^{-18}$ cm^2/sr. Both cross sections were integrated over the same range of energies. These results show that the effective experimental value for the product $n\ell\Delta\Omega$ should be written as

$$\left[\overline{n\ell\Delta\Omega}\right]_{\text{effective}} = \frac{1}{11.875} \times \left[\overline{n\ell\Delta\Omega(\theta_o)}\right]_{\text{calculated}} . \qquad (106)$$

In order that absolute cross sections can be obtained from the data acquired with the present system, the product $n\ell\Delta\Omega(\theta_o)$ in the denominator of equation (94) on page 130 should be replaced by the righthand side of equation (106). The term $\boxed{n\ell\Delta\Omega}_{calculated}$ appearing in equation (106) is calculated using equation (72) on page 108 for n, equation (98) on page 137 for ℓ, and equation (99) on page 142 for $\Delta\Omega(\theta_o)$.

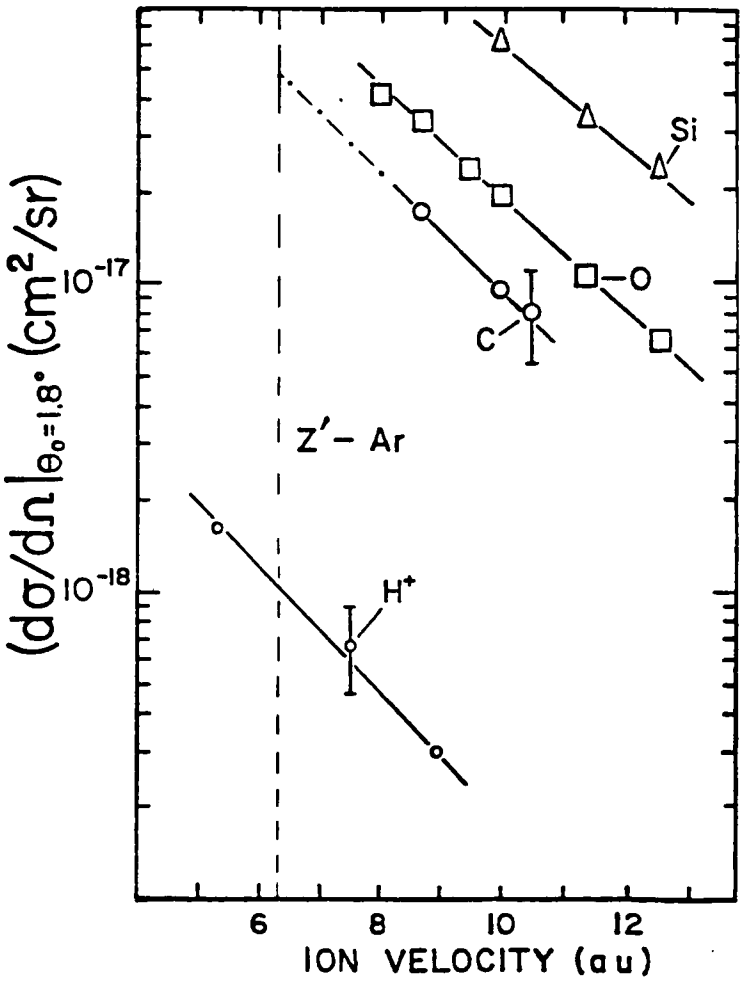

Figure 35. ECC Singly Differential Cross Section for H^+, C^{6+}, O^{8+}, and Si^{14+} on Argon.

(•–•) Extrapolation of data of Vane.[2]
(---) Marks the velocity of the C^{6+} ion used in the present study.
(Reproduced from reference 2.)

Calculation of Cross Sections

All cross sections were determined by use of equation (94) on page 130, where the energy limits of the integral E_1 and E_2, were the energies corresponding to the electron velocity v_e, such that $v_e = v_p(1+\alpha)$, where $\alpha = 0.04$.[2,14] This corresponded to an energy width of about 8% on either side of the cusp peak. Cross sections were calculated from both the data and fitted curves and the associated errors were estimated with equation (101). The cross section for atomic hydrogen was derived in two ways; first, the fitted curve for the H_2 in Figure 33 was normalized to correct number density n_2^*, of H_2 inside the hot oven and then subtracted from the curve fitted to the hot mixture data of Figure 34. The cross section was then calculated by integrating this resulting curve over the energy range E_1 to E_2. The second method considered the yield of ECC electrons due to the mixture of H and H_2 in the hot oven. This yield is

$$Y_{ECC}(H,H_2) \propto n^*\sigma(H+H_2) \approx n_1^*\sigma_{ECC}(H) + n_2^*\sigma_{ECC}(H_2), \qquad (105)$$

where $\sigma_{ECC}(H+H_2)$, $\sigma_{ECC}(H)$, and $\sigma_{ECC}(H_2)$ represent the ECC cross sections for $H+H_2$, H, and H_2, respectively. Solving this for $\sigma_{ECC}(H)$ gives,

$$\sigma_{ECC}(H) = \frac{n^*\sigma_{ECC}(H+H_2) - n_2^*\sigma_{ECC}(H_2)}{n_1^*} . \qquad (106)$$

From Figure 24, on page 112, at $T^* = 2250$ for $f = 0.50$, it is found that $n^* = 0.448\ n_2$, $n_1^* = 0.299\ n_2$, and $n_2^* = 0.149\ n_2$, where n_2 is the number density in the cold oven for the same gas flow rate into the oven. Equation (106) then becomes

$$\sigma_{ECC}(H) = 1.5\sigma_{ECC}(H+H_2) - 0.5\sigma_{ECC}(H_2). \qquad (107)$$

Equation (107) is not strictly accurate since each $n\sigma$ term in equation (106) should contain an additional target length factor, i.e.,

$$Y_{ECC}(H+H_2) \propto n^*\ell^*\sigma_{ECC}(H+H_2) = n_1^*\ell_1^*\sigma_{ECC}(H) + n_2^*\ell_2^*\sigma_{ECC}(H_2) \qquad (108)$$

where ℓ^*, ℓ_1^*, ℓ_2^* represent the effective target length of the $H+H_2$ mixture, H, and H_2, respectively. However, the error introduced by assuming equal target lengths is negligible.

Results of ECC Measurements

The results of the cross section determinations are shown in Table VII. It is immediately apparent from Table VII that the cross section for ECC from H_2 is not twice the cross section for ECC from H. This ratio is

$$\frac{\sigma_{ECC}(H_2)}{\sigma_{ECC}(H)} \approx 1.25.$$

When the errors are considered, however, the ratio may vary between $\sim$0.3 and $\sim$4. It has been found previously for low energy bound state capture that this ratio is less than 2.[53] However, the counting statistics of the present data preclude any conclusion concerning this feature.

The errors quoted in Table VII result from the combination of the independent errors given by equation 101 on page 143. The largest contributing error was the error due to counting statistics σ_Σ. This error was 17%, 31%, and 36%, for cold H_2, $H+H_2$ mixture, and H, respectively. The extrapolation used for cross section calibration discussed on page 146 was assumed to have the same 35% error quoted by Vane[2] for the experimental data.

TABLE VII

EXPERIMENTAL ECC CROSS SECTIONS FOR 12 MeV C^{6+} INCIDENT ON ATOMIC AND MOLECULAR HYDROGEN

	Data $\left(\frac{cm^2}{sr\text{-}particle}\right)^{\dagger}$	Fit $\left(\frac{cm^2}{sr\text{-}particle}\right)^{\dagger}$
H_2	$(5.58\pm3.4)\times10^{-19}$	5.52×10^{-19}
$H+H_2$	$(4.84\pm3.3)\times10^{-19}$	4.93×10^{-19}
H	$^{*}(4.48\pm2.3)\times10^{-19}$	$^{*}4.63\times10^{-19}$ $^{**}4.39\times10^{-19}$

All cross sections with exception of those for H were calculated with equation (94).

*Determined using equation (107) along with data values of $\sigma_{ECC}(H_2)$ and $\sigma_{ECC}(H+H_2)$.

**From difference of fitted curves to $(H+H_2)$ mixture and H_2 along with equation (94).

†One particle is defined as one molecule for H_2 and one atom for H.

As mentioned previously, low counting statistics prevented any complete study of spectral shapes. It is obvious, however, that the spectra shown in Figures 32-34 on pages 147-149, have the characteristic asymmetric cusp shape of ECC distributions. A comparison of the full-width-at-half-maximum (FWHM) for each of the spectra is given in Table VIII. The FWHM are calculated in two ways: 1) Using the FWHM obtained directly from the fits to the data. 2) By inserting the values obtained from the least squares fitting procedure for the parameters v_p and Θ_o

TABLE VIII

FULL-WIDTH-AT-HALF-MAXIMA MEASURED FOR ECC CUSPS

Target	Fit Parameters Θ_o	Fit Parameters v_p (au)	FWHM (au) (Fit)	FWHM (au)* (Dettmann)
H_2	1.968^o	6.317	0.219	0.325
$H+H_2$	2.119^o	6.323	0.373	0.350
H	2.139^o	6.320	0.414	0.328

*Using the present experimental values of $\Theta_o = 2^o$ and v_p (12 MeV C^{6+}) = 6.326 au, Dettmann's formula yields $3/2\ v_p\Theta_o$ = 0.331 au.

into Dettmann's formula, FWHM = $3/2\ v_p\Theta_o$ (see page 28). The FWHM given in Table VIII are not considered to be accurate since the data is much too scattered. The fit parameters Θ_o and v_p, are of particular interest, however. The least squares fitting procedure varied these two parameters (along with several other parameters) while searching parameter-space for the optimum values. Although Θ_o and v_p were initially set equal to the experimental values, the fitting procedure did not significantly change these values. This indicated that no major systemmatic errors were being introduced by the data collection apparatus.

Conclusions

The electron impact heated hydrogen dissociation oven was found to be a convenient method by which an atomic hydrogen static gas target could be produced for ECC measurements. The background due to blackbody

radiation from the hot oven was essentially eliminated by providing adequate physical barriers along with some electrical biasing. It was found that the electron spectrometer could remain close to the hot oven indefinitely without incurring any damage. The dissociation fraction inside the oven was determined using the double capture method with a 1.38 MeV C^{3+} incident ion. The determination of the dissociation fraction was found to be very difficult since the double capture cross section even at this fairly low (for the ORNL EN Tandem Accelerator) energy is small. Significant improvement would be realized if a low energy proton source (50-100 keV) could be used to determine this dissociation fraction. The cross sections for the double capture process are much larger at these low energies.[27]

Measurements of the ECC spectra on H_2 and subsequently H were found to be very time consuming because of the small cross sections involved; however, this study clearly shows that it is possible to obtain ECC spectra from an atomic hydrogen target. In order to accurately characterize the ECC spectrum from atomic hydrogen, a complete study is necessary. Each spectrum obtained must have significantly better counting statistics than the spectrum shown in Figure 34 on page 149. For this reason, a comprehensive study will require very long data acquisition times since the acquisition rate is very low.

LIST OF REFERENCES

LIST OF REFERENCES

1. Kenneth D. Sevier, Low Energy Electron Spectrometry. John Wiley and Sons, Inc. (1972).

2. C. R. Vane, Electron Capture to Continuum States of Bare Ions. Thesis, The University of Tennessee (1979).

3. M. E. Rudd and J. Macek, Case Studies in Atomic Physics 3, 125 (1972).

4. L. H. Thomas, Proc. R. Soc. 114, 569 (1927).

5. H. C. Brinkman and H. A. Kramers, Proc. Acad. Sci. Amsterdam 33, 973 (1930).

6. J. R. Oppenheimer, Phys. Rev. 31, 349 (1928).

7. Robin Shakeshaft and Larry Spruch, Rev. Mod. Phys. 51, 369 (April 1979).

8. R. M, Drisko, Ph.D. Thesis, Carnegie Institute of Technology, 1955.

9. W. J. B. Oldham, Phys. Rev. 161, 1 (1967).

10. M. E. Rudd, C. A. Sautter, and C. L. Bailey, Phys. Rev. 151, 20 (1960).

11. G. B. Crooks and M. E. Rudd, Phys. Rev. Lett. 25, 1599 (December 1970).

12. Joseph Macek, Phys. Rev. A 1, 235 (February 1970).

13. A. Salin, J. Phys. B 2, 631 (1969); 5, 979 (1972); 2, 1255 (1969).

14. M. Breinig, S. B. Elston, S. Huldt, L. Liljeby, C. R. Vane, S. D. Berry, G. A. Glass, M. Schauer, and I. A. Sellin, Phys. Rev. A 25, 3015 (June 1982).

15. C. R. Vane, I. A. Sellin, M. Suter, G. D. Alton, S. B. Elston, P. M. Griffin, and R. S. Thoe, Phys. Rev. Lett. 40, 1020 (April 1978).

16. M. Rødbro and F. D. Anderson, J. Phys. B 12, 2883 (1979).

17. C. R. Vane, I. A. Sellin, S. B. Elston, M. Suter, R. S. Thoe, G. D. Alton, S. D. Berry, and G. A. Glass, Phys. Rev. Lett. 43, 1388 (November 1979).

18. K. Dettmann, K. G. Harrison, and M. W. Lucas, J. Phys. B 7, 269 (1974).

19. F. T. Chan and J. Eichler, Phys. Rev. A 20, 367 (July 1979).

20. Robin Shakeshaft and Larry Spruch, Phys. Rev. Lett. 41, 1037 (1978).

21. D. H. Jakubassa-Amundsen, J. Phys. B: At. Mol. Phys. 16, 1767 (1983).

22. D. H. Jakubassa-Amundsen and P. A. Amundsen, Z. Physik A 297, 203 (1980).

23. C. R. Garibotti and J. E. Miraglia, Phys. Rev. A 21, 572 (February 1980).

24. C. R. Garibotti and J. E. Miraglia, J. Phys. B: At. Mol. Phys. 14, 863 (1981).

25. D. H. Jakubassa-Amundsen and P. A. Amundsen, J. Phys. B: At. Mol. Phys. 14, 1705 (1981).

26. Joseph Macek, J. E. Potter, M. M. Duncan, M. G. Menendez, M. W. Lucas, and W. Steckelmacher, Phys. Rev. Lett. 46, 1571 (June 1981).

27. J. E. Bayfield, Rev. Sci. Instr. 40, 869 (July 1969).

28. G. W. McClure, Phys. Rev. 148, 47 (August 5, 1966).

29. G. J. Lockwood, H. F. Helbig, and E. Everhart, J. Chem. Phys. 41, 3820 (December 15, 1964).

30. R. A. Phaneuf, F. W. Meyer, and R. H. McKnight, Phys. Rev. A 17, 534 (February 1978).

31. A. B. Wittkower, G. Ryding, and H. B. Gilbody, Proc. Phys. Soc. 89, 541 (1966).

32. C. Can, Tom J. Gray, J. M. Hall, L. Tunnell, and S. L. Varghese, Bull. Am. Phys. Soc. 27, 800 (September 1982).

33. J. M. George, Ph.D. Thesis, University of Missouri at Rolla, 1978.

34. M. R. C. McDowell and J. P. Coleman, Introduction to the Theory of Ion-Atom Collisions. North Holland Publishing Co., 1970.

35. R. Aaron, R. D. Amrado, and B. W. Lee, Phys. Rev. 121, 319 (1961).

36. K. Dettmann and G. Liebfried, Z. Physik. 210, 43 (1968).

37. Sydney Geltman, Topics in Atomic Collision Theory. Academic Press, Inc. 1969.

38. L. D. Landau and E. M. Lifshitz, Quantum Mechanics, Addison-Wesley Publishing Co., Inc. 1958.

39. Milton Abbramowitz and Irene A. Stegun, Handbook of Mathematical Functions. Dover Publications, New York, 1972, see formulae 13.12 and 13.3.2, 504-506.

40. H. S. W. Massey and C. B. O. Mohr, Proc. Roy. Soc. (London) 140 613 (1933).

41. D. R. Bates and G. Griffing, Proc. Soc. A 66, 961 (1953).

42. L. D. Faddeev, Soviet Physics JETP 12, 1014 (May 1961).

43. Marianne Breinig, Stuart Elston, Ivan Sellin, Leif Liljeby, Robert Thoe, Charles R. Vane, Harvey Gould, Richard Marrus, and Roman Laubert, Phys. Rev. Lett. 45, 1689 (1980).

44. S. D. Berry, I. A. Sellin, K.-O. Groeneveld, D. Hofmann, L. H. Andersen, M. Breinig, S. B. Elston, M. M. Schauer, N. Stolterfoht, H. Schmidt-bocking, G. Nolte, and G. Schiwietz, IEEE Transactions on Nuclear Science, NS-30 (April 1983).

45. J. S. Briggs, J. Phys. B: At. Mol. Phys. 10, 3075 (1977)

46. J. E. Miraglia and M. H. Ponce, J. Phys B: At. Mol. Phys. 13, 1195 (1980).

47. A. Guthrie and R. K. Wakerling, Vacuum Equipment and Techniques. 1st edition. McGraw-Hill Book Co., Inc. (1949);

48. Edward M. Purcell, Phys. Rev. 54, 818 (November 1938)

49. F. R. Paolini and G. C. Theodoridis, Rev. Sci. Instr. 38, 579 (May 1967).

50. muRata Corporation Technical Data Sheet, Report #RB11D2005.

51. G. J. Lockwood and E. Everhart, Phys. Rev. 125, 567 (January 1962)

52. J. R. Pierce, Theory and Design of Electron Beams. D. Van Nostrand Company, Inc. (1949).

53. James A. Fay, Molecular Thermodynamics. Addison-Wesley (1965), Chapter 14.

54. J. R. Macdonald and F. W. Martin, Phys. Rev. A 4, 1965 (November 1971).

55. J. R. Anderson, I. M. Ritchie, and M. W. Roberts, Nature 227, 705 (August 1970).

56. Phillip R. Bevington, Data Reproduction and Error Analysis for the Physical Sciences. McGraw-Hill, Inc. 1969.

57. W. Meckbach, I. B. Nemirovsky, and C. R. Garibotti, Phys. Rev. A 24, 1793 (October 1981).

58. S. D. Berry, I. A. Sellin, K.-O. Groeneveld, D. Hofmann, L. H. Andersen, M. Breinig, S. B. Elston, M. M. Schauer, N. Stolterfoht, H. Schmidt-Bocking, G. Nolte, and G. Schiwietz, IEEE Transactions on Nuclear Science, NS-30 (April 1983).

59. S. D. Berry, Private Communication.

60. M. Suter, C. R. Vane, I. A. Sellin, S. B. Elston, G. D. Alton, R. S. Thoe, and R. Laubert, Phys. Rev. Lett. 41, 399 (1978).

61. M. W. Lucas, W. Steckelmacher, J. Macek, and J. E. Potter, J. Phys. B: At. Mol. Phys. 13, 4833 (1980).

62. Irving Langmuir and Katherine Blodgett, Phys. Rev. 24, 49 (1924).

63. Irving Langmuir and G. M. J. MacKay, J. Am. Chem. Soc. 36, 1708 (1914); 37, 417 (1915); 38, 1145 (1916).

64. I. Manning, Phys. Rev. 139, B495 (1965).

65. T. V. Goffe, M. B. Shah, and H. B. Gilbody, J. Phys. B: At. Mol. Phys. 12, 3763 (1979).

66. Methods of Experimental Physics: Atomic Interactions, Part A, edited by L. Marton and Claire Marton. Academic Press, Inc. 1968.

APPENDICES

APPENDIX A

EQUILIBRIUM DISSOCIATION FRACTION

Almost 70 years ago it was discovered[63] that refractory metals maintained at high temperatures act as catalyzing agents in dissociating H_2 molecules. The process by which this dissociation occurs is both pressure and temperature dependent, however, the dissociation process must compete with the inverse process of recombination. For a given temperature, thermal and chemical equilibrium exists for all pressures but the fraction of molecules which are dissociated decreases with increasing pressure.

Detailed quantum mechanical calculations of the reactions between gaseous molecules and a solid surface are very complex and require parameterization of general properties of the solid and gas. Much of the physics is often lost in the mathematical computations. Even when an analytical solution is obtainable, the model has necessarily been simplified to the point where direct comparison to (or prediction of) physical reality is of little practical value. One method of reducing the problem to manageable size is to isolate, both experimentally and theoretically, the parameters which are considered important and generalize these to other physical systems. The basis for this method lies in determining the electronic structure of the solid and gas and by using this information to describe the nature of the interactions between the two. An alternative to this complex technique is the application of chemical kinetics and subsequent determination of reaction rates and other pertinent information. This latter method yields useful information with relatively few complicated mathematical manipulations.

Knowledge of several parameters is required for the application of the formulae but it can, in general, be obtained experimentally. When discussing molecular dissociation and recombination on a metal surface, for example, the reaction rates are determined by only a few basic variables: depth of potential wells on a solid surface capable of binding atoms to the surface, the average number of "binding sites" per unit area on the surface, dissociation energy of the diatomic gaseous molecule in question, and the probability that an atom will be bound to the surface in one of the binding sites. These parameters can either be determined directly from experiment or estimated fairly accurately using other information. When discussing the design of a hydrogen dissociation oven, it is not the reaction rates which are most important but the existence and nature of chemical equilibrium for the gas-surface interaction.

The dissociation fraction inside the hot oven is given by

$$f = \frac{n_1^*}{n_1^* + 2n_2^*} \tag{A.1}$$

where n_1^* = number of H atoms per unit volume, n_2^* = number of H_2 molecules per unit volume and (*) denotes high temperature. The denominator in this expression is a constant since the number of H atoms, whether bound or free, is conserved. The dissociation fraction is a measure of what fraction of H atoms are free. The following discussion is derived for the most part from Reference 53. The statement of dynamical equilibrium is written in the following form:

$$H_2 \rightleftarrows 2H. \tag{A.2}$$

The equilibrium constant K_p, is defined as

$$K_p \equiv \frac{P_1^2}{P_2}, \tag{A.3}$$

where P_1 and P_2 are the partial pressures of H and H_2, respectively. This equilibrium constant is a function of temperature only, as long as both H and H_2 can be considered to be ideal gases. The validity of this ideal gas state can be shown by first writing K_p in terms of the total partition functions of the gases H and H_2 as

$$K_p = \frac{P_1^2}{P_2} = \frac{(Q_1 kT/V)^2}{(Q_2 kT/V)}, \tag{A.4}$$

where $Q_j \equiv$ total partition function for the j^{th} gas. But for ideal gases, the total partition function Q_j, can be factored into two terms

$$Q_j = Q_j^{(t)} Q_j^{(i)}, \tag{A.5}$$

where

$$Q_j^{(t)} \equiv \text{translational partition function}, \tag{A.6}$$

and

$$Q_j^{(i)} \equiv \text{internal partition function}. \tag{A.7}$$

Now an ideal gas is defined as being a gas which is unaffected by external forces, i.e., all collisions between ideal gas particles are perfectly elastic. Because the gas molecule or atom is unaffected by

external forces, the total quantized energy for that atom can be written as a sum of separately quantized translational and internal energies.

$$\varepsilon_j = \varepsilon_j^{(t)} + \varepsilon_j^{(i)}. \tag{A.8}$$

Equation (A.8) allows the total partition function to factored as shown in equation (A.5). The internal partition function $Q_j^{(i)}$, can be further simplified. The internal energy $\varepsilon_j^{(i)}$ can be written as a sum of all internal energy components

$$\varepsilon_j^{(i)} = \varepsilon_j^{(r)} + \varepsilon_j^{(v)} + \varepsilon_j^{(e)}, \tag{A.9}$$

where $\varepsilon_j^{(r)} \equiv$ rotational energy, $\varepsilon_j^{(v)} \equiv$ vibrational energy, and $\varepsilon_j^{(e)} \equiv$ electronic energy. Even though the individual internal modes of motion are not strictly independent of one another, equation (A.9) can still be used if great accuracy is not required. The internal partition function $Q_j^{(i)}$, can be factored into three parts by using equation (A.9) and the fact that, in general, the partition function Q, is given by

$$Q = \sum_j C_j e^{-\varepsilon_j/kT}, \tag{A.10}$$

where C_j is a constant. Using (A.10) with (A.9) gives

$$Q_j^{(i)} = Q_j^{(r)} Q_j^{(v)} Q_j^{(e)}. \tag{A.11}$$

Combining the result of equation (A.11) with equation (A.5) then gives the final expression for the total partition function

$$Q_j = Q_j^{(t)} Q_j^{(r)} Q_j^{(v)} Q_j^{(e)}. \tag{A.12}$$

The partition functions corresponding to those in (A.12) can be shown to be the following for monatomic gases and diatomic gaseous molecules,[53]

$$Q_j^{(t)} = \left(\frac{2\pi m_j kT}{h^2}\right)^{3/2} V.$$

$$Q_j^{(r)} = \tfrac{1}{2}\, T/\Theta_r \text{ for } T \gg \Theta_r, \tag{A.13}$$

$$Q_j^{(v)} = (1-e^{-\Theta_v/T})^{-1},$$

where Θ_r and Θ_v are characteristic rotational and vibrational temperatures, respectively. Note that the only expression for $Q_j^{(r)}$ requires a restriction on the value of T. This restriction is easily met at the temperature inside the hydrogen oven. The value of $Q_j^{(e)}$ can be obtained in the following way: $Q_j^{(e)}$ for both H and H_2 can be written in the same form

$$Q_j^{(e)} = \sum_j g_i e^{-\varepsilon_i/kT} = g_o + g_i e^{-\varepsilon_1/kT} + g_2 e^{-\varepsilon_2/kT} + \ldots, \tag{A.14}$$

where $g_i \equiv$ degeneracy of the i^{th} quantum electronic state, $\varepsilon_i \equiv$ energy of the i^{th} quantum electronic state, and $\varepsilon \equiv 0$.

For the case of H, it is obvious that $g_o = 2$. For H_2 the situation is not quite so obvious. When considering two separate atoms, one with ground state degeneracy g_1, and the other with ground state degeneracy g_2, there are $g_1 g_2$ ways in which these atoms can interact when brought together. Not all of the interaction potential curves will have a

minimum. If more than one curve with a minimum exists, the curve with the lowest minimum will correspond to the ground state of the molecule if the atoms are each in the ground state also. For two interacting H atoms, there are four potential curves. Only one of these has a minimum, however. The remaining three are identical and form a repulsive triplet state. The singlet state is therefore the only possible bound state which can give electronic states for the H_2 molecule. So for the H_2 molecule, $g_o = 1$. As long as the temperature is low enough so that the first excited electronic state does not appreciably contribute to the partition function, then only the ground state need be included. This restriction is given by,

$$|\varepsilon_o - \varepsilon_{i>o}| \gg kT. \tag{A.15}$$

This restriction is easily met since $|\varepsilon_o - \varepsilon_1|_H \simeq 0.2$ eV, $|\varepsilon_o - \varepsilon_1|_{H_2} \simeq 11.4$ eV, and $kT \leq 0.2$ eV. Then the values of the electronic partition functions are given by

$$Q_j^{(e)} = \begin{cases} 2 \text{ for H} \\ 1 \text{ for } H_2 \end{cases} . \tag{A.16}$$

Rewriting equation (A.4)

$$K_p = \frac{\left[Q_H^{(t)} Q_H^{(r)} Q_H^{(v)} Q_H^{(e)} kT/V\right]^2}{Q_{H_2}^{(t)} Q_{H_2}^{(r)} Q_{H_2}^{(v)} Q_{H_2}^{(e)} kT/V} .$$

Inserting the expressions in equation (A.13) and (A.16) gives

$$K_p = \frac{\left[\left(2\pi m_H kT\right)^{3/2}(1)(1)(2)kT\right]^2 e^{-\varepsilon_d/kT}}{h^3\left(2\pi m_{H_2} kT\right)^{3/2}(\tfrac{1}{2}T/\Theta_r)\left(1-e^{-\Theta_v/T}\right)^{-1}kT}, \qquad (A.17)$$

where $Q_j^{(r)} = Q_j^{(v)} = 1$.

The term $e^{-\varepsilon_d/kT}$ appears as the result of the necessity to use a common reference level from which to measure the energies of internal motion of the molecules (or atoms). It is convenient to assume that all atoms have zero energy when in their lowest translational and electronic state. In that case, all molecules will have an energy of formation which is the energy required to form the molecule in its ground state from the required atoms in their ground states. The quantized internal of the j^{th} molecules is then

$$\varepsilon_j^{(i)} = \varepsilon_j^{(i)^*} + \varepsilon_j. \qquad (A.18)$$

The internal partition function then becomes

$$Q_j^{(i)^*} = Q_j e^{-\varepsilon_j^{(i)^*}/kT}. \qquad (A.19)$$

Equation (A.19) is used in equation (A.4) and the result is equation (A.17). The energy ε_d, represents the dissociation energy of the H_2 molecule. Replacing the mass m, by the molecular weight M, divided by Avogadro's number N_A, equation (A.17) yields

$$K_p = \frac{P_H^2}{P_{H_2}} = \left[\left(\frac{2\pi}{N_A}\right)^{3/2}(kT)^{5/2}h^{-3}\right]\left(\frac{M_H^2}{M_{H_2}}\right)\left[\frac{8\Theta_r}{T}\left(1-e^{-\Theta_v/T}\right)\right]e^{-\varepsilon_d/kT}. \qquad (A.20)$$

Inserting the values for the constants, using $\Theta_v = 6325K$, $\Theta_r = 87.5K$, $\varepsilon_d = 4.48$ eV and 1 N/M^2 = 7.5 mTorr,[53] equation (A.20) becomes

$$K_p(T) = 4.814 \times 10^6 \left[T^{3/2}(1-e^{-6325/T})\right] e^{-5.2 \times 10^4/T} \quad \text{mTorr} \tag{A.21}$$

Note that K_p is a function only of T for ideal gas conditions.

By using equation (A.1) along with equation (A.3), it may be easily shown that

$$f = \sqrt{\frac{K_p(T)}{K_p(T)+4P}}\,, \tag{A.22}$$

where $P \equiv P_1 + P_2$.

APPENDIX B

DOUBLE CAPTURE METHOD FOR MEASURING DISSOCIATION FRACTION

When an incident ion beam passes through the oven, additional charge states of the ion beam can be produced by electron capture and loss processes. For single collision conditions, an incident ion beam can capture two electrons only from the molecular hydrogen present in the oven. If $\sigma_{i,j}$ denotes the cross section for changing the incident ion charge state from i to j by an interaction with an H_2 target of thickness $\pi(H_2)$, then the yield of ions capturing two electrons from the H_2 per unit charge collected in the Faraday cup is given by

$$Y_{q,q-2} = \sigma_{q,q-2}(H_2)\pi(H_2) + \sigma_{q,q-1}(H_2)\sigma_{q-1,q-2}(H_2)\pi^2(H_2). \qquad (B.1)$$

Note that $\pi(H_2) \equiv n(H_2)\ell(H_2)$, where $n(H_2)$ is the number density of H_2 in the oven and $\ell(H_2)$ is the length of the H_2 target region. The last term on the right is a contribution possible only for double collisions and will henceforth be disregarded. Considering the same process, but with the oven hot

$$Y^*_{q,q-2}(H,H_2) = \sigma_{q,q-2}(H_2)\pi^*(H_2) + \text{2nd order terms}. \qquad (B.2)$$

Dividing (B.2) by (B.1) and defining $Y^* \equiv Y_{q,q-2}(H_2)$ and $Y \equiv Y_{q,q-2}(H_2)$

$$\frac{Y^*}{Y} = \frac{\pi^*(H_2)}{\pi(H_2)} \quad . \qquad (B.3)$$

Now consider the flow of gas into the oven. The flow of hydrogen atoms

at temperature T, into the oven must be equal to the flow of hydrogen atoms at temperature T^*, out of the oven. These atoms are bound into a molecule when entering the oven and only some of these are still bound when exiting the oven. So equating the flow rates

$$2n_w v_2 = 2n_2^* v_2^* + n_1^* v_1^*, \tag{B.4}$$

where $n_i \equiv$ number of particles/volume for the i^{th} particle, $v_i \equiv$ velocity of the i^{th} particle, and i = 1,2 denotes H and H_2, respectively. But $v_i \alpha \sqrt{\frac{T}{m_i}}$ and $\pi_i = n_i \ell_i$ where $\ell \equiv$ target length, so (B.4) becomes

$$\pi_2^* = \sqrt{\frac{T^*}{T}}\left[\pi_2 + \frac{1}{\sqrt{2}}\pi_1^*\right] . \tag{B.5}$$

Using (B.5) in (B.3) gives,

$$\frac{Y^*}{Y} = \sqrt{\frac{T}{T^*}}\left[\frac{\pi_2^*}{\pi^* + \frac{1}{\sqrt{2}}\pi_1^*}\right] . \tag{B.6}$$

Now the dissociation fraction f, is defined as

$$f = \frac{n_1^*}{n_1^*+2n_2^*} = \frac{\pi_1^*}{\pi_1^*+2\pi_2^*} \text{ for } \ell_1 \approx \ell_2 . \tag{B.7}$$

So solving (B.7) for π_1^*, and using in (B.6)

$$\frac{Y^*}{Y} = \frac{1-f}{1+f(\sqrt{2}-1)}\sqrt{\frac{T}{T^*}} . \tag{B.8}$$

The temperature dependence in (B.8) can be removed by considering the process in equations (B.1) and (B.2) for a nondissociating gas in the oven, say argon. Defining $A^* \equiv Y^*_{q,q-2}(Ar)$ and $A \equiv Y_{q,q-2}(Ar)$, the equations (B.1) and (B.2) become

$$A = \sigma_{q,q-2}(Ar)\pi(Ar) , \tag{B.9}$$

$$A^* = \sigma_{q,q-2}(Ar)\pi^*(Ar) . \tag{B.10}$$

Dividing (B.10) by (B.9) gives

$$\frac{A^*}{A} = \frac{\pi^*(Ar)}{\pi(Ar)} . \tag{B.11}$$

But equation (B.4) can also be rewritten for argon

$$n_{Ar}v_{Ar} = n^*_{Ar}v^*_{Ar},$$

or,

$$\frac{\pi^*(Ar)}{\pi(Ar)} = \sqrt{\frac{T}{T^*}} . \tag{B.12}$$

The solving (B.8) for f and using (B.11) and (B.12) gives two equivalent equations

$$f = \frac{\sqrt{\frac{T}{T^*}} - \frac{Y^*}{Y}}{\sqrt{\frac{T}{T^*}} + \frac{Y^*}{Y}(\sqrt{2}-1)} , \tag{B.13}$$

and,

$$f = \frac{\frac{A^*}{A} - \frac{Y^*}{Y}}{\frac{A^*}{A} + \frac{Y^*}{Y}(\sqrt{2}-1)} \quad . \tag{B.14}$$

APPENDIX C

SINGLE LOSS-SINGLE CAPTURE METHOD FOR DETERMINING DISSOCIATION FRACTIONS

Consider an ion beam passing through the hot hydrogen oven. If the incident ion is not a completely stripped ion, then either capture or loss of electrons can occur when H_2 is introduced into the oven. If an ion beam of intensity I_o, particles per cm^2 per sec and ion charge q, is incident (under single collision conditions) on the mixture of H and H_2 gas in the hot oven, the number of ions per second losing one electron is given by,

$$Y_{q,q+1} = I_o \left[\sigma_{q,q+1}(H)n(H)\ell(H)+\sigma_{q,q+1}(H_2)n(H_2)\ell(H_2)\right] . \qquad (C.1)$$

Similarly, the number of ions per second capturing one electron is,

$$Y_{q,q-1} = I_o \left[\sigma_{q,q-1}(H)n(H)\ell(H)+\sigma_{q,q-1}(H_2)n(H_2)\ell(H_2)\right], \qquad (C.2)$$

where $\sigma_{q,q\pm1}$ represents the cross section for the loss (+) or capture (-) of a single electron by the incident ion and is assumed to be obtained independently. $\ell(j)$ and $n(j)$ represent, respectively, the target length and target number density for the j^{th} species of gas. It will be assumed that $\ell(H)\approx\ell(H_2)\equiv\ell$. The dissociation fraction is defined as

$$f = \frac{n(H)}{n(H)+2n(H_2)}. \qquad (C.3)$$

Solving (C.3) for $n(H_2)$ and inserting in (C.1) and (C.2) gives

$$Y_{q,q+1} = n(H)\ell\sigma_{q,q+1}(H)\left[1+\frac{1-f}{2f}R_L\right], \tag{C.4}$$

and

$$Y_{q,q-1} = n(H)\ell\sigma_{q,q-1}(H)\left[1+\frac{1-f}{2f}R_C\right], \tag{C.5}$$

where

$$R_L \equiv \frac{\sigma_{q,q+1}(H_2)}{\sigma_{q,q+1}(H)} \text{ and } R_C \equiv \frac{\sigma_{q,q-1}(H_2)}{\sigma_{q,q-1}(H)}. \tag{C.6}$$

Equations (C.4) and (C.5) are two linearly independent equations with two unknowns f and n(H), and the linear independence will hold only if $R_C \neq R_L$. Dividing (C.4) by (C.5), and simplifying

$$\frac{Y_{q,q+1}}{Y_{q,q-1}} = \frac{\sigma_{q,q+1}(H)}{\sigma_{q,q-1}(H)}\left[\frac{R_L+f(2-R_L)}{R_C+f(2-R_C)}\right]. \tag{C.7}$$

The left hand side of (C.7) can be measured directly while the cross section $\sigma_{q,q+1}(H)$ and $\sigma_{q,q-1}(H)$ and the ratios R_L and R_C can be obtained from other published data. If either R_C or R_L is equal to two, there will be a decrease in the sensitivity of the measurement of f using (C.7). This corresponds to the situation that when a H_2 molecule dissociates the number of particles in the oven increases by one but the cross section per particle decreases by a factor of two so that the resultant signal remains the same before and after the dissociation event. When this conditions occurs, the experimental measurement cannot be expected to be sufficiently sensitive.

Using tabulated values of the cross section for a 1.380 MeV C^{3+} incident ion[65] equation (C.7) is reduced to,

$$\frac{Y_{3,4}}{Y_{3,2}} = \frac{0.1134+0.0946f}{2.235-0.235f} , \qquad (C.8)$$

where $R_L = 1.09$, $R_C = 2.235$ and $\frac{\sigma_{3,4}(H)}{\sigma_{3,2}(H)} = 0.104$. Note that although R_L is certainly not close to a value of two, the same is not necessarily true of R_C. While choosing the energy and charge state of the incident ion so that $R_L \neq R_C$ was relatively easy, fulfilling the additional requirement that $R_L \neq R_C \neq 2$ was more difficult. The 1.38 MeV C^{3+} ion was the best possible choice for the tabulated values. It was questionable however, how precisely and accurately the dissociation fraction f, would be determined when considering the almost linear relation between f and $\frac{Y_{3,4}}{Y_{3,2}}$ as seen in Figure C.1. It was found that because of the relative insensitivity exhibited in the plot in the figure, as well as the beam regulating difficulties discussed in Chapter III, this method could not be used to give accurate determinations of f. This method could, however, probably be successfully used for incident energies lower than those attainable on the EN Tandem accelerator used in this study.

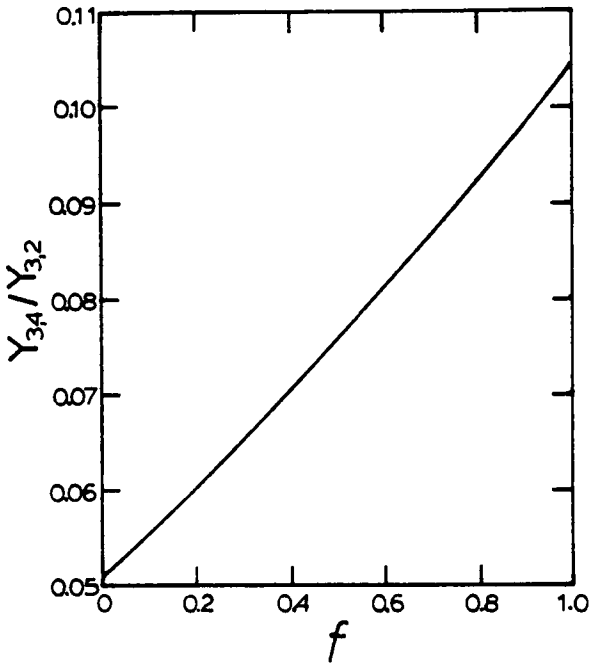

Figure C.1. Ratio of Single-Loss to Single-Capture Yields Versus Dissociation Fraction.

Plotted from equation (C.8).

APPENDIX D

THE ELECTRON GUN

The objectives in designing the electron gun used to heat the oven were threefold: 1) heating efficiency, 2) compactness, and 3) durability. The actual cathode chosen was a 0.76 cm diameter BaO dispenser cathode. This cathode could produce up to 9 amp/cm^2. The cathode heater required $\sim$2.5 amp at $\sim$10 VAC in order to operate most efficiently while the largest emission current required was $\sim$250 ma. The following discussion concerns the principles upon which the design of the lens system was based.

The flow of electrons between two concentric spheres can be described by Poisson's equation in spherical coordinates,[52]

$$\nabla^2 V = \frac{1}{\bar{r}^2}\frac{d}{d\bar{r}}\left(\bar{r}^2\frac{dV}{d\bar{r}}\right) = -\frac{\rho}{\varepsilon} \quad , \tag{D.1}$$

where ρ is the charge density, ε is the permittivity of the space between the cathode and anode spheres, $\bar{r}$ is the distance from the center of the spheres, and V is the potential. V is considered to be spherically symmetric for the purposes of this discussion. Assuming space charge limited flow between the spheres then (D.1) becomes

$$\frac{1}{\bar{r}^2}\frac{d}{d\bar{r}}\left(\bar{r}^2\frac{dV}{d\bar{r}}\right) = \frac{I}{4\pi\bar{r}^2\sqrt{2\eta}\,V^{1/2}} \quad , \tag{D.2}$$

where $\rho = \frac{I}{4\pi\bar{r}^2\dot{\bar{r}}}$, $\eta \equiv \frac{e}{m}$, and $\dot{\bar{r}} = \sqrt{2\eta}\,V^{1/2}$. The solution is parameterized in terms of $(-\alpha^2)$,[62]

$$I = 29.33\times10^{-6}\ \frac{V^{3/2}}{(-\alpha^2)}\ \text{amp}, \tag{D.3}$$

where $\alpha=\alpha\ (\bar{r}_c/\bar{r}_a)$, $\bar{r}_c \equiv$ cathode radius, and $\bar{r}_a \equiv$ anode radius. I, in equation (D.3), represents the current for a 4π solid angle of emission. For a cone of half angle Θ, the current I_o, is given by

$$I_o = \frac{I}{4\pi}\int_o^{\Theta} d\Omega = \left(\frac{1-\cos\Theta}{2}\right)I, \tag{D.4}$$

or, using $(-\alpha^2)=0.75$, for $\bar{r}_c/\bar{r}_a = 2$ then,[62]

$$I_o = 14.67\times10^{-6}\ V^{3/2}\ \text{amp}, \tag{D.5}$$

where $V \equiv V_{anode}-V_{cathode}$. Assuming that the anode has a small hole through which the electrons are focused, once the beam of electrons has passed through the hole in the anode it will enter a field-free region where space charge effects of the beam itself will cause the beam to diverge. The anode hole will act as a diverging lens of focal length[52]

$$f_a = \left.\frac{-4V}{\frac{dV}{d\bar{r}}}\right|_{\bar{r}\ =\ \text{anode radius}\ (\bar{r}_a)} \equiv \frac{-4V}{V'}\ . \tag{D.6}$$

If the anode hole did not act as a lens, the focal distance of the beam upon entering the hole would be

$$\frac{1}{f} = \frac{1}{\bar{r}_a}\ . \tag{D.7}$$

Combining this with the focal distance of the aperture, the total focal distance is given by,

$$\frac{1}{F} = \frac{1}{f} + \frac{1}{f_a}, \tag{D.8}$$

or using equations (D.6) and (D.7),

$$\frac{1}{F} = \frac{1}{\bar{r}_a} - \frac{V'}{4V}. \tag{D.9}$$

Using (D.3) in (D.9) gives

$$\frac{\bar{r}_a}{F} = \left[1 - \frac{\frac{\bar{r}_c}{\bar{r}_a} \frac{d(-\alpha^2)}{d(\bar{r}_c/\bar{r}_2)}}{6(-\alpha^2)} \right]. \tag{D.10}$$

Figure D.1 shows a plot of $\bar{r}_a/\bar{r}$ versus $\bar{r}_c/\bar{r}_a$ which gives the change in focal distance due to the focusing effect of the anode aperture; i.e., $\bar{r}_a$ is the point on the axis to which the electrons are aimed before passing through the anode aperture and F is the point on the axis to which the electrons are aimed after passing through the anode aperture. Now, it can be shown for axially symmetric beams with constant potential and zero magnetic field that,[52]

$$\frac{d^2r}{dz^2} = \frac{I}{4\sqrt{2}\pi\epsilon\eta^{\frac{1}{2}}V^{3/2}r}, \tag{D.11}$$

where r ≡ beam radius, and z ≡ distance along central axis of beam from the anode hole. This equation can be simplified by defining,

$$\begin{aligned} r_o &\equiv \text{beam radius at anode hole}, \\ R &\equiv r/r_o, \\ Z &\equiv \left[\frac{I}{2\sqrt{2}\pi\epsilon\eta^{\frac{1}{2}}V^{3/2}}\right]^{\frac{1}{2}} \frac{z}{r_o} = 174 \frac{I^{\frac{1}{2}}}{V^{3/4}} \frac{z}{r_o}. \end{aligned} \tag{D.12}$$

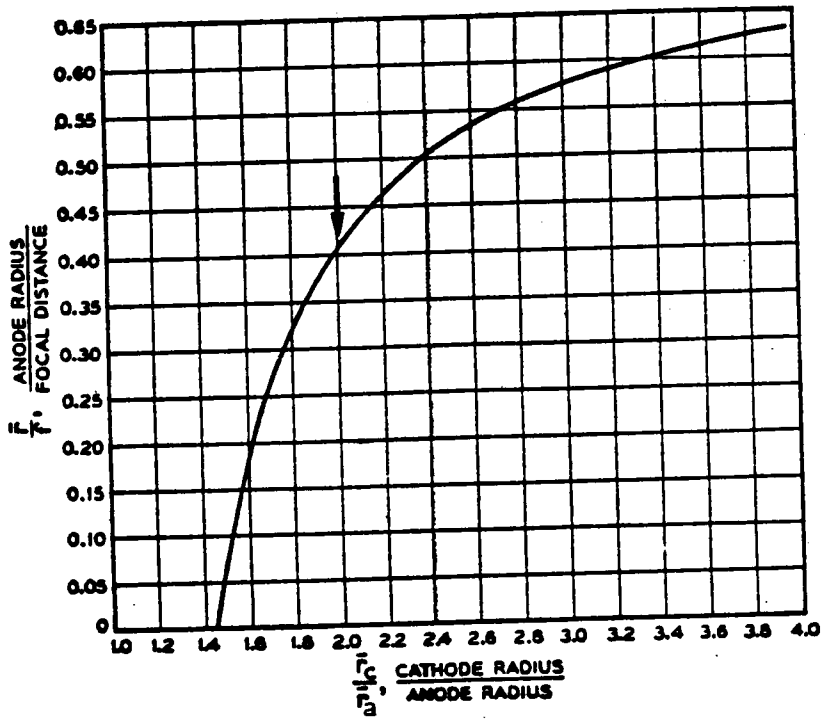

Figure D.1. Effect of Anode Aperture on Electron Beam Focal Point.

Plotted from Equation (D.10). Arrow shows the value of $\bar{r}_c/\bar{r}_a$ used in the oven heating electron gun. (Reproduced from reference 52.)

Then,

$$R'' = \frac{1}{2R'} \tag{D.13}$$

where $R' \equiv \frac{\partial R}{\partial Z}$. Inserting (D.5) and (D.12) gives

$$Z = 174\left[14.67\text{x}10^{-6}\,\frac{1-\cos\theta}{(-\alpha^2)}\,V^{3/2}\right]^{\frac{1}{2}}\frac{1}{V^{3/4}}\,\frac{z}{r_o}\,, \tag{D.14}$$

or,

$$Z = \frac{2}{3}\left[\frac{1-\cos\theta}{(-\alpha^2)}\right]^{\frac{1}{2}}\frac{z}{r_o}\,. \tag{D.15}$$

Note that for small anode hole diameters, $\theta \approx r_o/r_a$, and $1-\cos\theta \approx \frac{1}{2}(r_o/r_a)^2$. This gives

$$Z_{\theta_{small}} = 0.471\,\frac{1}{\sqrt{(-\alpha^2)}}\,\frac{z}{r_a}\,. \tag{D.16}$$

When the beam emerges from the anode hole it is focused so that[52]

$$\frac{dr}{dz} = \frac{-r_o}{F}\,. \tag{D.17}$$

Using (D.12)

$$dz = \frac{V^{3/4}r_o}{174I^{\frac{1}{2}}}\,dZ,$$

and

$$dr = r_o\,dR.$$

So,

$$\left.\frac{dr}{dz}\right|_{r=r_o} = \frac{dR}{dZ}\frac{r_o}{V^{3/4}}\frac{174}{r_o} I^{1/2} = \frac{dR}{dZ}\frac{174}{r_o} I^{1/2} = \frac{-r_o}{F} . \tag{D.18}$$

Using (D.5) in (D.18) gives,

$$\frac{dR}{dZ}\frac{174}{V^{3/4}}\left[14.6\times10^{6}\,\frac{1-\cos\Theta}{(-\alpha^2)}\,V^{3/2}\right]^{1/2} = \frac{-r_o}{F} , \tag{D.19}$$

or, after using (D.12),

$$R_o' = -\frac{3(-\alpha^2)^{1/2}}{2(1-\cos\Theta)^{1/2}}\frac{r_a}{F} , \tag{D.20}$$

where $R_o' \equiv \left.\frac{dR}{dZ}\right|_{Z=z=o}$. For small Θ this reduces to

$$R_o' = \frac{3}{\sqrt{2}}\left[(-\alpha^2)\right]^{1/2}\frac{\bar{r}_a}{F} . \tag{D.21}$$

Equation (D.13) can be integrated to give,

$$(R')^2 = \ell n\ R + \quad (R_o')^2 \tag{D.22}$$

The minimum value of R is R_m, that value at which $R'\big|_{R_m} = 0$. So,

$$R_m = e^{-(R_o')^2} . \tag{D.23}$$

Using $R' = \frac{dR}{dZ}$, equation (D.22) may be integrated to give

$$Z = \int_{1}^{R} \frac{dR}{\left[\ell nR+(R_o')^2\right]^{\frac{1}{2}}} .$$

Changing variable to $u = R'$ and using (D.22) to give the limits

$$Z = 2e^{-(R_o')^2} \int_{R}^{\pm\left[\ell nR+(R_o')^2\right]^{\frac{1}{2}}} e^{u^2} du. \qquad (D.24)$$

The following schematic diagram shows the relationship between R and Z and the regions where $R'>0$ and $R'<0$.

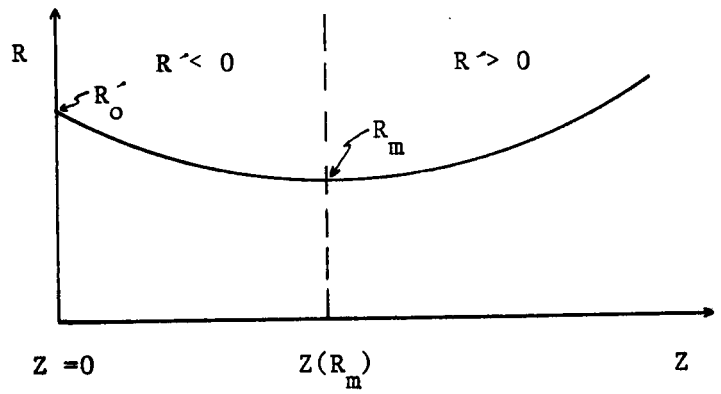

From (D.22)

$$R' = \pm \left[\ell nR+(R_o')^2\right]^{\frac{1}{2}}. \qquad (D.25)$$

For the initial trajectory, upon exiting the anode aperture, $R' \leq 0$ and $R(Z)<R_o$ for $Z \leq Z(R_m)$, after which $R'>0$ and $R(Z)<R_o$ for $Z>Z(R_m)$, so the limits in the integral in (D.24) are given by

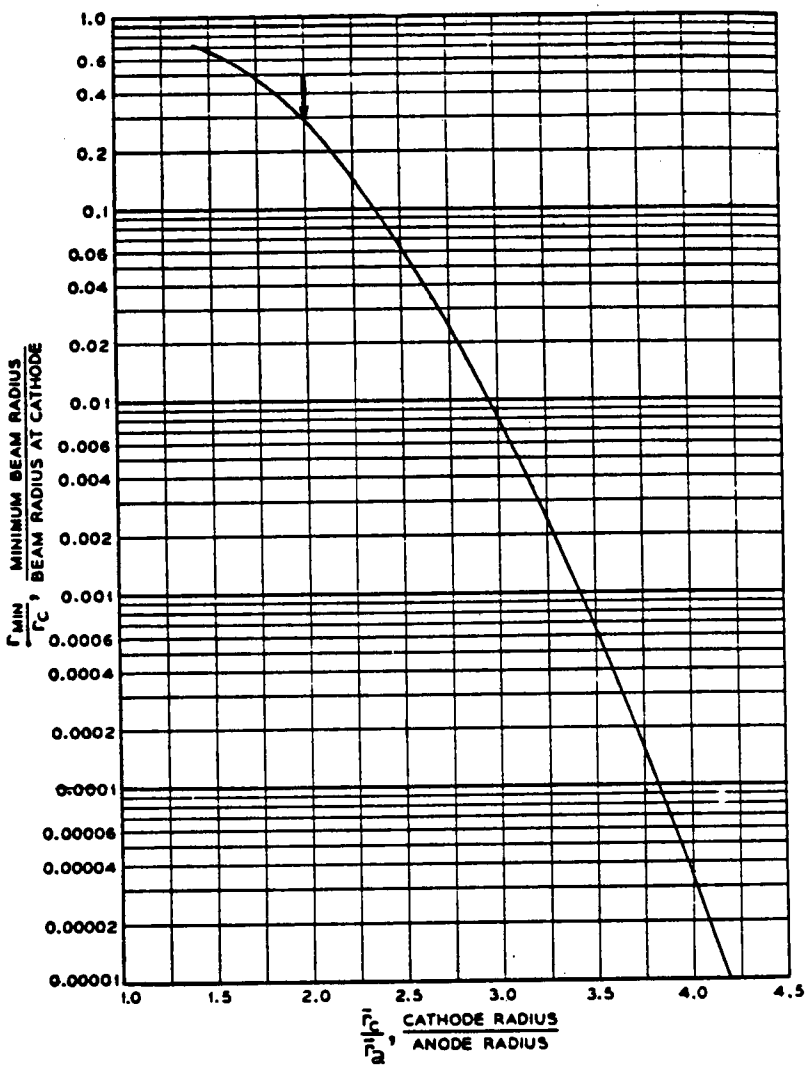

Figure D.2. Minimum Electron Beam Radius Compared to Radius at Cathode.

Arror shows the value of $\bar{r}_c/\bar{r}_a$ used in the oven heating electron gun. (Reproduced from reference 52.)

$$R_o' \leq R' \leq -\left[\ell nR+(R_o')^2\right]^{\frac{1}{2}} \quad \text{for } R \leq R_m, \tag{D.26}$$

and

$$0' \leq R' \leq +\left[\ell nR+(R_o')^2\right]^{\frac{1}{2}} \quad \text{for } R > R_m. \tag{D.27}$$

In many instances, it is easier and more convenient to parameterize distances in terms of well-known quantities. By measuring z (the distance along the beam axis from the anode hole) in terms of the cathode radius $\bar{r}_c$, and r (the beam radius) in terms of the beam radius at the cathode r_c, the equations can be reduced to a form which is more convenient for designing electron guns.

Using the relation

$$\frac{r_c}{\bar{r}_c} = \frac{r_o}{\bar{r}_a}$$

in equation (D.12) and (D.16) gives

$$\frac{z}{\bar{r}_c} = \frac{3}{\sqrt{2}} \frac{\left[(-\alpha 2)\right]^{\frac{1}{2}}}{(\bar{r}_c/\bar{r}_a)} Z, \tag{D.28}$$

and

$$\frac{r}{r_c} = \frac{R}{r_c/\bar{r}_a} . \tag{D.29}$$

Using (D.10), (D.21), (D.28), and (D.29), the minimum beam radius can be compared with the beam radius at the cathode and this is shown in Figure D.2. From (D.24), (D.16), (D.21), and (D.28) the distance from the anode hole

to the point of minimum beam radius can be obtained in terms of $(\bar{r}_c/\bar{r}_a)$ see Figure D.3. Although the complete path could be plotted there probably would not be any incentive for doing so since the paths at best would only provide a good starting point for trial and error testing of a particular electron gun design. This is especially true for the oven heating gun used in this study in view of the fact that the anode aperture radius is much larger than allowed by the approximation of equation (D.16). Figure D.4 shows the approximate path of the electron beam for the dimensions used in the electron gun heating the oven. The position of the tungsten plug shown in the figure was optimized for plug lifetime and heating efficiency.

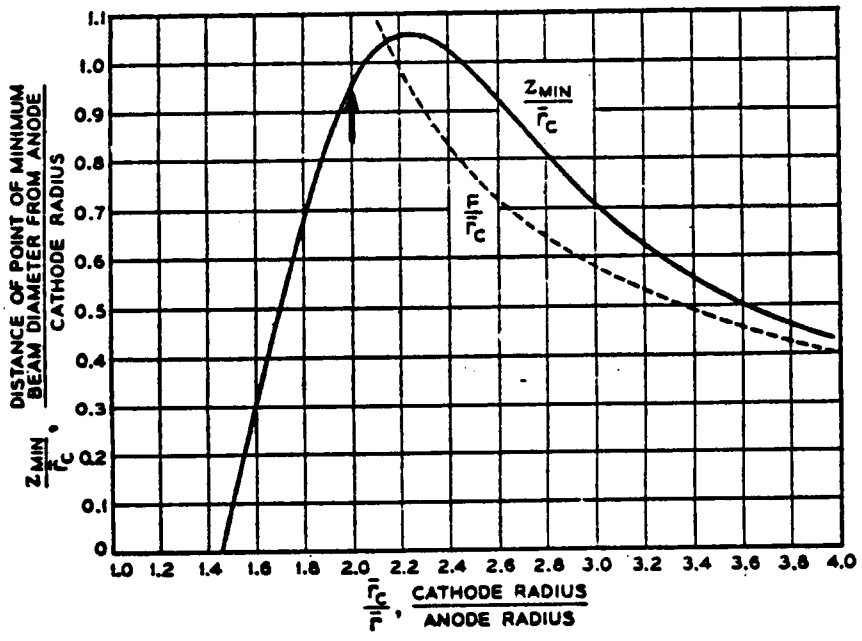

Figure D.3. Position of Minimum Beam Radius Relative to Anode.

Arrow shows the value $\bar{r}_c/\bar{r}_a$ used for the oven heating electron gun. (Reproduced from reference 52.)

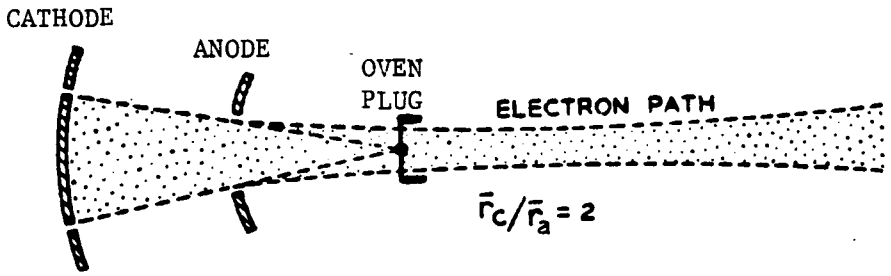

Figure D.4. Electron Path Through Cathode-Anode Lens System.

Converging dotted lines show path without focusing by anode hole. The oven plug is positioned at this convergence point. (Reproduced from reference 52.)

APPENDIX E

STATISTICAL ERRORS ASSOCIATED WITH DISSOCIATION FRACTION MEASUREMENTS

The experimental dissociation fraction can be written as in equation (B.13) in Appendix B.

$$f = \frac{\sqrt{\frac{T}{T^*}} - \frac{Y^*}{Y}}{\sqrt{\frac{T}{T^*}} + \frac{Y^*}{Y}(\sqrt{2}-1)} \tag{E.1}$$

where $Y^* \equiv Y^*_{q,q-2}(H_2)$ and $Y \equiv Y_{q,q-2}(H_2)$. Since the quantities Y^* and Y represent number of ions counted over some time, the statistical error associated with each is $\sqrt{Y^*}$ and $\sqrt{Y}$, respectively. The statistical error in Y^*/Y is

$$\varepsilon_y \equiv \frac{Y^*}{Y}\sqrt{\left(\frac{\sqrt{Y^*}}{Y^*}\right)^2 + \left(\frac{\sqrt{Y}}{Y}\right)^2} = \frac{Y^*}{Y}\sqrt{\frac{1}{Y^*} + \frac{1}{Y}} \tag{E.2}$$

It will be assumed that the error in $\sqrt{T/T^*}$ is negligible. Rewriting (E.1), including the uncertainties

$$f = \frac{\sqrt{\frac{T}{T^*}} - \left[\frac{Y^*}{Y} \pm \frac{Y^*}{Y}\sqrt{\frac{1}{Y^*} + \frac{1}{Y}}\right]}{\sqrt{\frac{T}{T^*}} + \left[\frac{Y^*}{Y} \pm \frac{Y^*}{Y}\sqrt{\frac{1}{Y^*} + \frac{1}{Y}}\,(\sqrt{2}-1)\right]} \quad . \tag{E.3}$$

If N/D is a fraction in which both N and D have some statistical uncertainty ε_N and ε_D, respectively, then the total uncertainty in the ratio, N/D is given by $\pm N/D\ (\varepsilon_N/N^2 + (\varepsilon_D/D)^2$. Writing the uncertainty

in f from (E.3) in this way and rearranging terms gives

$$f = f_{exp}\left\{1 \pm \left[\frac{\varepsilon_Y^2}{\left(\sqrt{\frac{T}{T^*}} - \frac{Y^*}{Y}\right)^2} + \frac{\varepsilon_Y^2\,(\sqrt{2}-1)^2}{\left[\sqrt{\frac{T}{T^*}} - \frac{Y^*}{Y}(\sqrt{2}-1)\right]^2}\right]^{\frac{1}{2}}\right\}, \qquad (E.5)$$

where f_{exp} is given by (E.1). If the dissociation fraction is written as (B.14) instead, the estimated errors give

$$f = f_{exp_A}\left\{1 \pm \left[\frac{\varepsilon_A^2 + \varepsilon_Y^2}{\left(\frac{A^*}{A} - \frac{Y^*}{Y}\right)^2} + \frac{\varepsilon_A + \varepsilon_Y\,(\sqrt{2}-1)^2}{\left[\frac{A^*}{A} - \frac{Y^*}{Y}(\sqrt{2}-1)^2\right]}\right]^{\frac{1}{2}}\right\}, \qquad (E.4)$$

where $A^*/A \equiv Y^*_{q,q-2}(Ar)/Y_{q,q-2}(Ar)$, $\varepsilon_A \equiv A^*/A\,\sqrt{1/A^* + 1/A}$ and

$$f_{exp_A} \equiv \frac{\frac{A^*}{A} - \frac{Y^*}{Y}}{\frac{A^*}{A} + \frac{Y^*}{Y}(\sqrt{2}-1)}\,.$$

VITA

Gary Alan Glass was born in New Iberia, Louisiana on December 10, 1948. He moved to Lafayette, Louisiana and attended elementary school there. He was graduated from Lafayette High School in June 1966 and entered the University of Southwestern Louisiana the following September.

After a four-year tour of duty with the United States Navy beginning in January 1971, he again entered the University of Southwestern Louisiana, and in June 1976 he received a Bachelor of Science degree in Physics. After receiving his Master's degree in Physics from the University of Southwestern Louisiana, he entered the Graduate School of The University of Tennessee, Knoxville, in September 1978.

The author is a member of Phi Kappa Phi and Sigma Pi Sigma. Mr. Glass is currently employed with the United States Naval Surface Weapons Center in Silver Spring, Maryland.

He is married to the former Judy Cook of New Orleans, Louisiana and has two children.